BETA DECAY STUDIES OF ^{69}Ni AND ^{58}V: DEVELOPMENT OF SUBSHELL GAPS WITHIN THE N = 28 - 50 SHELL

By

Joann I. Prisciandaro

A DISSERTATION

Submitted to
Michigan State University
in partial fulfillment of the requirements
for the Degree of

DOCTOR OF PHILOSOPHY

Department of Chemistry

2001

ABSTRACT

BETA DECAY STUDIES OF ^{69}Ni AND ^{58}V: DEVELOPMENT OF SUBSHELL GAPS WITHIN THE N = 28 - 50 SHELL

By

Joann I. Prisciandaro

Macroscopically, nuclei with magic proton or neutron numbers (N, Z = 2, 8, 20, 28, 50, 82 and 126) may be described with spherical charge distributions and modest collective features at low excitation energy. Between the magic shell closures, collective interactions amid nucleons becomes evident, inducing quadrupole deformation. This deformation becomes apparent in the form of vibrational and rotational excitations within the low-energy level spectrum and are expected to be maximum at midshell. However, the development of collectivity away from major closed shells may be inhibited by the presence of subshell closures, or minor shell gaps.

In the framework of this thesis, the development of subshell gaps at $N = 32$ and $N = 40$ for neutron-rich nuclides within the $N = 28 - 50$ shell were investigated.

A conventional beta detection system was used to examine the beta decay properties of neutron-rich nuclei near $N = 40$. An $N = 40$ subshell was first suggested for $^{68}_{28}Ni_{40}$ by Broda *et al.* [1] due to the rise of the first excited 2^+ state relative to its N - 2 neighbor, ^{66}Ni. The presence of an $N = 40$ subshell would inhibit the development of collectivity in this midshell region. During this study, a 3.4(7) s isomeric state in ^{69}Ni was directly produced via the fragmentation of a 70 MeV/nucleon ^{76}Ge beam in a ^{9}Be target at the National Superconducting Cyclotron Laboratory (NSCL) at Michigan State University. The beta decay of the $1/2^-$ isomer was observed to mainly populate the excited $3/2^-$ state at 1296 keV in ^{69}Cu. By comparing the total number of ^{69}Ni nuclei implanted with the intensities of the beta-delayed γ rays following the decay of the $1/2^-$ isomeric state and the ground state of ^{69}Ni, a 36% upper limit has been extracted for the beta branch from the isomeric state in ^{69}Ni to the ground

state of ^{69}Cu. Based on this branching ratio, a small 2p-2h mixture into the ground state of ^{69}Cu may be deduced. This small admixture suggests that the ground state of ^{69}Cu is predominately single-particle in nature and may be described as a proton coupled to a ^{68}Ni core. The dominance of the ^{68}Ni core provides a strong case for the $N = 40$ subshell.

A new beta detection system was employed to study the decay properties of neutron-rich nuclides near $N = 32$. An $N = 32$ subshell gap was first suggested following the measurement of the high-energy 2_1^+ state of $^{52}Ca_{32}$ [2]. Similar to the case of ^{52}Ca, the first excited 2^+ state of ^{56}Cr lies higher in energy relative to its $N - 2$ neighbor, ^{54}Cr. To determine whether the first excited 2^+ state continued to rise or is peaked at $N = 32$, it was necessary to measure $E(2_1^+)$ beyond $N = 32$.

^{58}V was produced following the fragmentation of ^{70}Zn at 70 MeV/nucleon in a ^{9}Be target at the NSCL. The ground state beta decay of ^{58}V was observed to mainly proceed into the 880 keV state of ^{58}Cr. In comparison to the first excited 2^+ state of $^{56}_{24}Cr_{32}$, a peak in this energy for even-even neutron-rich chromium isotopes is now evident at ^{56}Cr. The current measurement provides the first conclusive evidence for a significant subshell gap at $N = 32$. The presence of the $N = 32$ subshell gap has been attributed to a strong $\pi 1f_{7/2}$-$\nu 1f_{5/2}$ proton-neutron monopole interaction.

Per i miei genitori, tanti baci e abbracci.

ACKNOWLEDGMENTS

First and foremost, I would like to thank my advisor, Paul Mantica. Thank you, Paul, for your guidance, wisdom and support. Without you, none of this would have been possible.

The research described within this dissertation was performed at the National Superconducting Cyclotron Laboratory at Michigan State University and involved the collaborative efforts of many at the NSCL and abroad. I would like to thank the operations staff at the NSCL for allowing my experiments to run so smoothly and the National Science Foundation for their generous financial support. In addition, I owe a debt of gratitude to my collaborators: Don Anthony, Matt Cooper, Alejendro Garcia, Daniel Groh, Mika Huhta, Alexander Komives, Wasantha Kumarasiri, Patrick Lofy, Anca Oros-Peusquens, Reg Ronningen, Samuel Tabor, William Walters and Mathis Wiedeking. Their assistance during my thesis experiments was invaluable.

I would like to thank B. A. Brown for performing the shell model calculations discussed within this dissertation for the $N = 29$ isotones in the region $20 \leq Z \leq 28$.

I would also like to express my gratitude to Thomas Baumann for addressing my LaTeX and GEANT questions. You have proven to be a LaTeX and GEANT guru!

Special thanks to David Morrissey, Thomas Glasmacher and Michael Thoennessen for serving on my guidance committee.

Without my family, I would be nothing. They have been a constant source of love, support and encouragement. Mom and dad, although you weren't fond of the idea of my moving away from New York and living an hour from Detroit, you were still very supportive. You have always been there for me when I needed you the most, thank you! And trust me, I will always remember where I came from with pride! Annette and Frank thank you for being there to lift my spirits. You always believed in me even when I did not, thank you! To my sister Isabella, thank you for your many words of encouragement and for your moral support. Thank for you flying out on Thanksgiving

so I wouldn't be lonesome, even though you told me about your plans the day before your flight. You always were the spontaneous one! And Jack, I don't know where to begin. Growing up, I always felt like I was trying to live up to you. However, as an adult I finally realized that would be impossible. You are an intelligent, kind and wonderful person. You have been dubbed the "successful" one in our family, and I certainly agree. However, what I admire the most about you is not what you have become, but whom. Throughout it all, you always seem to remember what is truly important in life, your family and friends. Thank you for teaching me the finer points in life.

I don't think I would be able to muster up enough courage each morning to drag myself into work without my fellow graduate students and friends. Although the list is lengthy, I would like to name just a few friends to which I am forever indebted. Pat, we started our graduate career together and struggled through the same classes and exams. You were certainly a better sport than I. Thanks for putting up with my grumbles and gripes, and thank you for bringing a little humour to the lab (I still can't seem to manage to get that song from "The Sound of Music" out of my head). I don't think I will soon forget your many antics. You always knew how to make me laugh, even at myself. I still chuckle when I think about the time you flipped the canoe over during that trip to Alma with the other first year chemistry students. Now that I think about it, wasn't I the only one that ended up sopping wet?!!

Graduate school can be a very challenging and stressful period, especially when you are one of several female graduate students in a male dominated program. Katie, you certainly made my time here a lot easier. You gave me the strength to believe in myself and also taught me a few lessons about taking time to enjoy myself and relax. I don't think I will ever forget our camping trip out west. From the outhouses, to the smores, to the little incident in Colorado. Sorry about your CD's. Thank you for being a terrific friend.

Being the first graduate student in a group is like being the first born child, it isn't easy. You feel like mom and dad's guinea pig as they get their parental bearings.

Although most siblings are resentful of their younger siblings, that was certainly not the case with my academic brother, Daniel. I was grateful when you joined Paul's group. It was nice to have a comrade and friend that I could confide in. Thank you for all of your help during my thesis experiment and for your kindness afterwards. I still have the card that you and Michelle gave me after my experiment with the cartoon elephant chained to the S2 vault. It remained on the wall in front of my computer throughout the remaining years of my graduate career to remind me of the more challenging times I've experienced at the laboratory. In addition, it was a constant reminder that even when things were rough, I have friends around me that could lift my spirits. Thank you for lending me a helping hand when I needed it the most, especially when I needed someone to proof read my thesis.

To my dear friend Irene, although I did not continue on to medical school with you as I originally planned, you were always there for me. You had the confidence in me that I certainly lacked. Thank you for being such a wonderful friend.

Last but certainly not least, I would like to thank Mike. The last few years have been among the happiest because you have been a part of my life. Thank you for knowing just when I needed a hug and for making me laugh when I wanted to cry (although at this point your story about the leaves is just about ready to make me cry :-). Thank you for being you!

Contents

List of Tables

List of Figures

Chapter 1

Introduction

1.1 The Atomic Nucleus

The atomic nucleus lies at the heart of all matter that surrounds us. It is a system on the order of 10^{-15} m, consisting of a collection of protons and neutrons. Considering that protons are positively charged, it would seem impossible to confine these particles within such a small volume; the electromagnetic interaction among the similarly charged protons should cause them to repel. However, the predominant force within the atomic nucleus is the strong force. This attractive, short-ranged force counteracts the repulsive electromagnetic interactions, thereby enabling the nucleus to survive.

The subatomic particles comprising the nucleus, the protons and neutrons, make up the class of particles known as nucleons. With the exception of their charge, $q_p = +1$ and $q_n = 0$, protons and neutrons are essentially indistinguishable. Protons and neutrons have a spin of 1/2, are composed of three quarks (p = uud and n = udd, where u and d represent up and down quarks) and have a mass of 938.3 and 939.6 MeV/c^2, respectively. Considering the atomic nucleus as a charge independent system, protons and neutrons can be treated as degenerate nucleon states. They are distinguished from one another with the assignment of a fictitious spin vector known as isospin [3] and they are given different projections within isospin space, $\pm 1/2$. This enables nuclear scientists to consider protons and neutrons independently of one another.

1.2 Development of the Nuclear Shell Model

During the early studies of the atom, discontinuities were observed in the first ionization energy as a function of atomic number, where ionization energy is the amount of energy required to remove an orbital electron from an atom. The discovery of these discontinuities, see Fig. 1.1, at $Z = 2$, 10, 18, 36, 54 and 86 provided the first empirical evidence for the existence of an electronic shell structure for the atom. Using

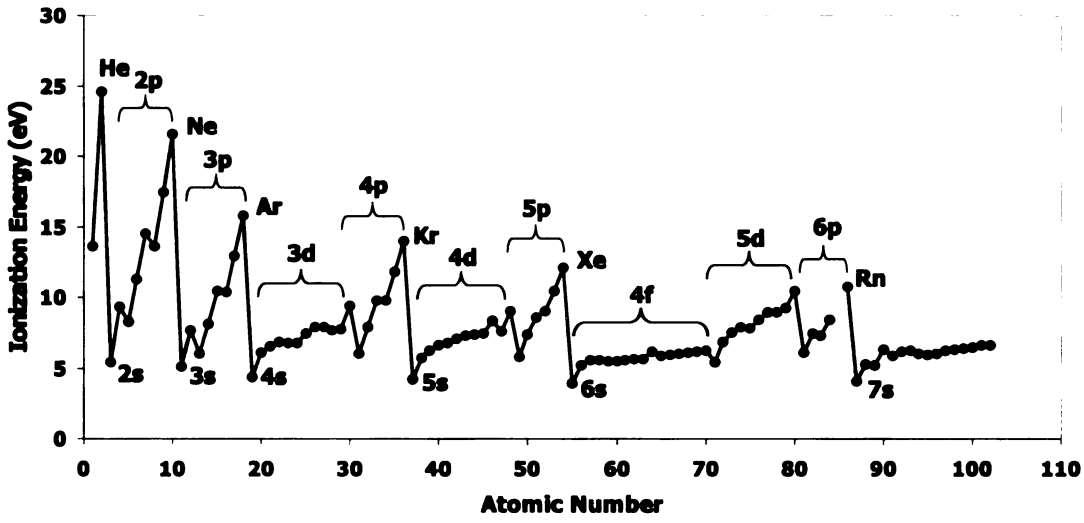

Figure 1.1: Systematics of the first ionization energy as a function of atomic number [4].

such models, atomic physicists were able to predict the properties of the atom in good agreement with experimental measurements. In the nuclear system, trends in nuclear masses and binding energies, B(Z,A), have suggested enhanced stability for nuclei associated with nucleon numbers 2, 8, 20, 28, 50, 82 and 126 (the magic nucleon numbers). For example, Fig. 1.2 depicts the difference in the experimental and theoretical two-nucleon separation energies versus nucleon number, where separation energy, S(p) or S(n), is the energy required to remove a nucleon, proton or neutron, from the nucleus. The peaks in ΔS(2p) and ΔS(2n), where S(2p) = B(Z,A) - B(Z-2,A-2) and S(2n) = B(Z,A) + B(Z,A-2), suggest enhanced binding at the magic nucleon numbers. As in the atomic case the existence of these magic numbers have led to the

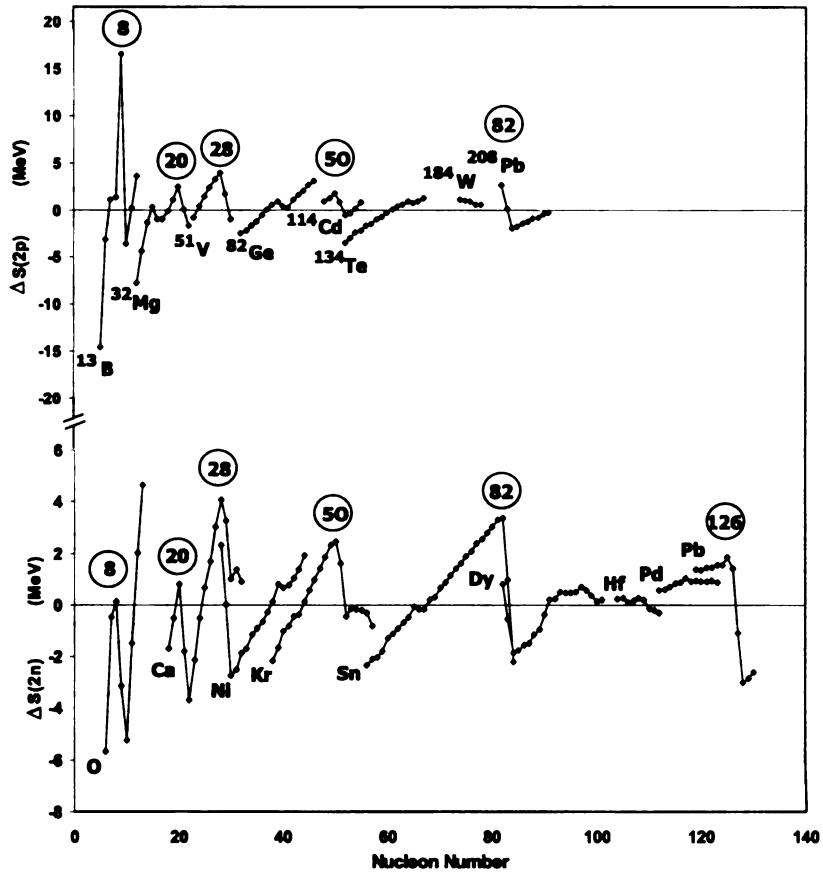

Figure 1.2: (Top) The difference between experimental and theoretical two-proton separation energies for a sequence of isotones. The lowest A members are noted. (Bottom) The difference between experimental and theoretical two-neutron separation energies for a sequence of isotopes. The theoretical two-nucleon separation energies were calculated based on the semi-empirical mass formula and the experimental values were obtained from Ref. [5]. This figure was adapted from Ref. [3].

development of the nuclear shell model, where the magic numbers correspond to the filling of major nuclear shells.

To model the phenomenological trends of the nucleus, theorists tried to develop a mathematical formulism to reproduce the known magic numbers. A large energy gap was expected between adjacent single-particle orbitals at major shell closures. Thus, such energy gaps should be apparent within the shell model at the magic numbers. However, in order to construct a shell model, an estimate of the nuclear potential was necessary. Unlike the atomic case, in which the potential is supplied by the Coulomb field of the nucleus [3], the nuclear potential is unknown. Some early candidates for

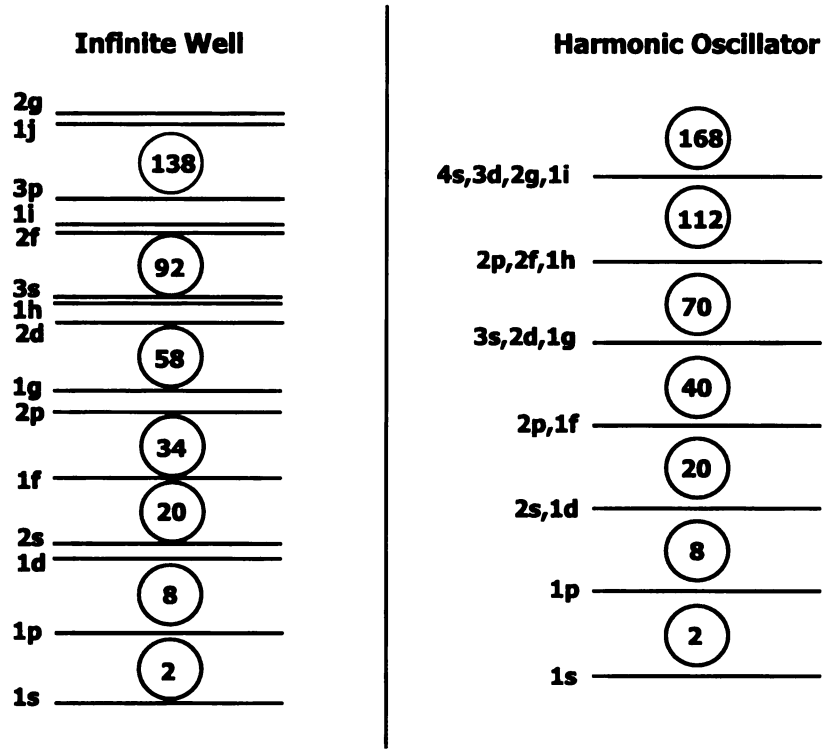

Figure 1.3: Calculated nuclear shell structure considering the infinite square well and harmonic oscillator potentials [3].

the nuclear potential were the infinite square well and the harmonic oscillator. The single-particle orbitals calculated with these potentials are shown in Fig. 1.3. Not only were these potentials unrealistic ($V \rightarrow \infty$ at the boundaries of the nucleus), they did not reproduce the correct magic numbers above 20.

As a next step, theorists considered the Woods-Saxon potential [6],

$$V(r) = \frac{-V_o}{1 + exp[(r - R_o)/a]} \tag{1.1}$$

where V_o represents the depth of the potential, r is the distance from the center of the nucleus, R_o is the mean radius (≈ 1.25 fm $A^{1/3}$), A is the atomic mass, and a is related to the "skin thickness," $4a \ln 3$, the distance over which the potential changes from 90 to 10% of V_o. Unlike the infinite square well and the harmonic oscillator, the Woods-Saxon potential smoothly falls off to zero at large values of r. Although the Woods-Saxon potential is a more realistic form of the nuclear potential, it could not reproduce all of the known magic numbers. The correct reproduction of the known

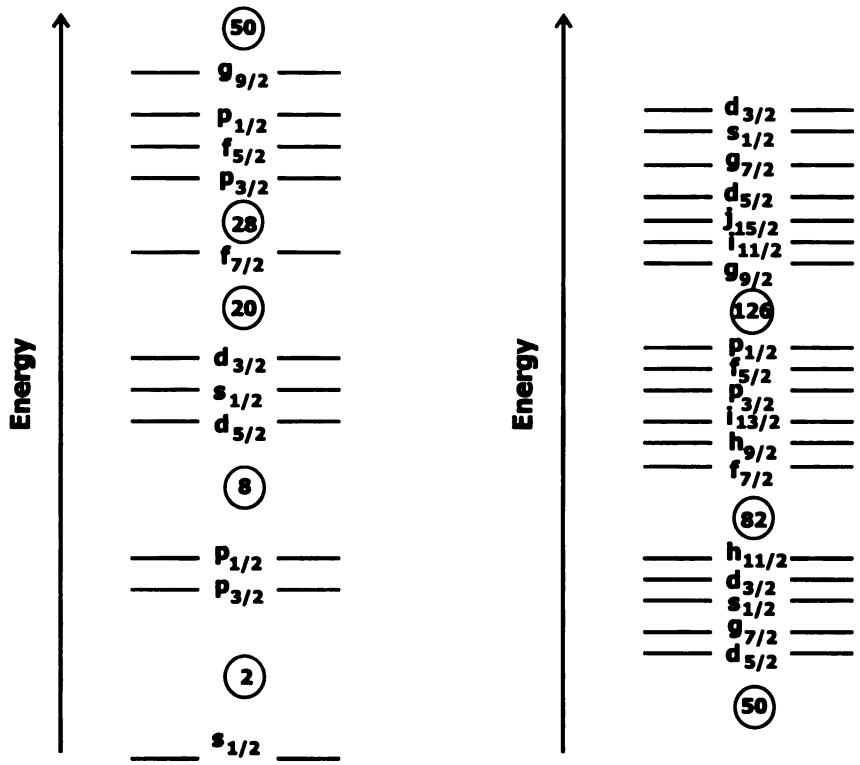

Figure 1.4: Modified nuclear shell structure with the inclusion of the spin-orbit interaction [7,8]. This figure is not drawn to scale.

magic numbers was not achieved until the spin-orbit interaction, $-V_{\ell s}\ \vec{\ell}\cdot\vec{s}$, where $V_{\ell s}$ is a strength constant, was included within the overall nuclear potential [7,8]. The $\vec{\ell}\cdot\vec{s}$ term of the spin-orbit interaction breaks the degeneracy for any pair of $\ell > 0$ states, drawing the $\ell + 1/2$ state lower in energy relative to the $\ell - 1/2$ state. This results in the reordering of the single-particle orbitals as shown in Fig. 1.4.

1.3 The Structure of Nuclear Systems

To the layperson, there is hardly a distinction between an atom and its nucleus. To a scientist, the atomic nucleus is often thought of as a spherical body consisting of protons and neutrons. Nuclei with magic proton or neutron numbers may be described with spherical charge distributions and modest collective features at low excitation energy. Following the spherical symmetry of the potential away from major shell closures, the nucleus has been found to deviate from sphericity, evolving into oblate

(discus-like) or prolate (football-like) bodies.

1.3.1 Nuclear Structure Near Shell Closures

Nuclei near major shell closures may be described microscopically by the shell model. The properties of these nuclei have been predicted in good agreement with experiment considering an extreme single-particle shell model. According to this model, the properties of the nucleus are dictated by the behavior of a single unpaired nucleon. To illustrate this point, consider as an example ^{41}Ca, which has 20 protons and 21 neutrons (see Fig. 1.5). In its ground state, the odd, 21^{st} neutron would reside in the $1f_{7/2}$ single-particle orbital. The predicted spin and parity for this state is $7/2^-$ ($J^\pi = J^{(-1)^\ell}$, where J and ℓ represent the total and orbital angular momentum of the odd neutron). Experimentally, the ground state spin and parity of ^{41}Ca have been determined to be $7/2^-$.

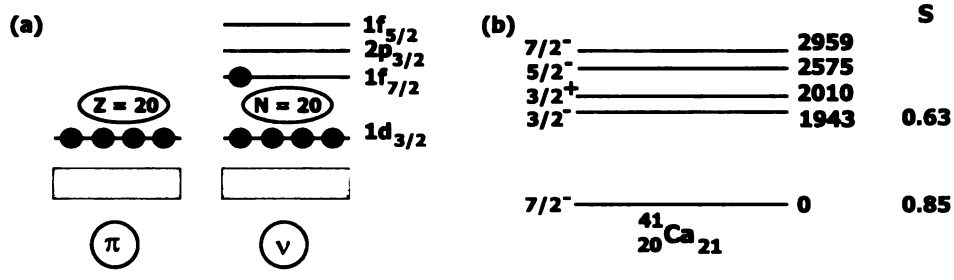

Figure 1.5: (a)The ground state single-particle proton and neutron configurations and (b)the low-energy level structure for ^{41}Ca [9]. The spectroscopic factor, S, is listed for the ground and first excited state of ^{41}Ca.

The parentage of a nuclear state is the fraction of that state that originates from a given nuclear configuration. To determine the parentage of the $7/2^-$ ground state of ^{41}Ca, it is necessary to examine the spectroscopic factor of this state. Spectroscopic factors provide a way to describe the fragmentation of single-particle configurations among the states of a given nucleus [10]. These values are typically extracted from data obtained in transfer reactions, either involving the pickup or stripping of a nucleon by the fragment of interest. Thus, the spectroscopic factor is the overlap between the final state configuration and the configuration obtained by coupling an odd nucleon

with a $(Z - 1)$ or $(N - 1)$ core. If there is no fragmentation of single-particle configurations, then $S = 1$. In reality, all states have some configuration mixing, thus $S < 1$.

For ^{41}Ca, several states have been assigned a spin and parity of $7/2^-$, however, a spectroscopic factor has only been extracted for its ground state [11], providing an upper limit of 0.85. This suggests that the ground state of ^{41}Ca has at most an 85% component from the $f_{7/2}$ single-particle orbital. In addition, the first excited state observed for ^{41}Ca at 1.9 MeV has a spin and parity of $3/2^-$. This experimentally extracted J^π is in agreement with the excitation of the odd neutron to the lowest unoccupied single-particle neutron orbital, $2p_{3/2}$. Although the spectroscopic factor for this state is lower, $S = 0.75$ [11], its configuration is predominately $p_{3/2}$ in nature. This example of ^{41}Ca represents a relatively simple configuration, however, most nuclei are more complex.

1.3.2 Quadrupole Deformation

Between the magic shell closures, more complex excitations develop. Microscopically, it is difficult to calculate the configurations of these new excited states. However, macroscopically these states can be described as the result of collective interactions amid nucleons, which induce quadrupole (prolate/oblate) deformation. The extent of quadrupole deformation is quantified by the quadrupole deformation parameter, β_2, and the sign of β_2 provides information on the shape of the nucleus. Values of $\beta_2 > 0$ are indicative of a prolate shaped nucleus, while $\beta_2 < 0$ suggests the nucleus is shaped like an oblate ellipsoid. Spherical nuclei have $\beta_2 \approx 0$. Nuclear shapes may also be specified by γ deformation, which is a measure of axial asymmetry. However, most known nuclei are believed to be axially symmetric, at least in their ground state [12]. Thus, for this study, the focus will be on quadrupole deformation.

1.4 Probing Nuclear Structure

Quadrupole deformation is expected to be maximum at midshell. In order to study such phenomena, experimental probes of quadrupole deformation may be utilized. There are a number of experimental probes that can be employed to determine the extent of quadrupole collectivity for a given nuclear system. The probes that have been considered for this study include the energy of the first excited 2^+ state, $E(2_1^+)$, and the ratio of the energies of the first excited 4^+ and 2^+ states, $E(4_1^+)/E(2_1^+)$.

1.4.1 $E(2_1^+)$

One measure of quadrupole collectivity in even-even (even number of protons and neutrons) nuclear systems is the energy of the first excited 2^+ state, $E(2_1^+)$. This value has been shown to be sensitive to the overall coherence and collectivity in the wave function of the first excited 2^+ state [13]. Figure 1.6 depicts the systematics of $E(2_1^+)$ versus nucleon number for a series of isotopes and isotones, nuclides with the same number of protons and neutrons, respectively. Similar to Fig. 1.2, peaks in $E(2_1^+)$ are apparent at the known magic numbers 8, 20, 28, 50, 82 and 126. Nuclei associated with a magic number of protons or neutrons exhibit an extra degree of binding, suggesting that excited nuclear states would lie high in energy. From a microscopic perspective, the peaks observed in the first excited 2^+ states for even-even nuclides near shell closures are relatively easy to explain. A sufficient amount of energy must be supplied to the nuclear system to break a pair of nucleons and excite one member of the pair to a higher-lying single-particle orbital. Promoting a nucleon across a shell gap will require a significant amount of energy, resulting in high $E(2_1^+)$ values. Away from shell closures, anomalously "low" 2^+ states were observed at energies even below that needed to break a pair of nucleons. Microscopically, this lowering may be attributed to multi-state mixing which draws collective quadrupole states lower in energy [13]. Macroscopically, the first excited 2^+ state is lowered as the potential energy surface softens, allowing for deformation to set in.

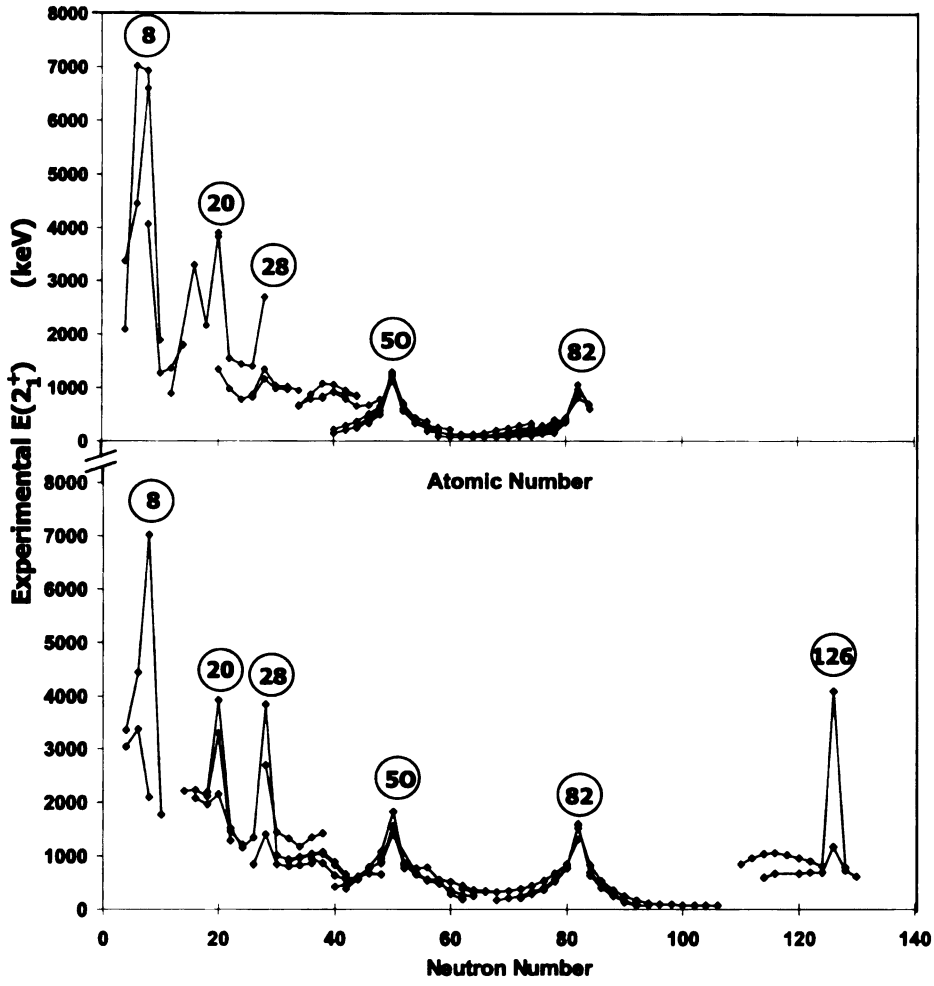

Figure 1.6: Experimental $E(2_1^+)$ systematics for (top) a series of isotones and (bottom) a series of isotopes. Peaks in $E(2_1^+)$ values are apparent at nucleon numbers 8, 20, 28, 50, 82 and 126. The data was taken from Ref. [9].

Based on the trends of the first excited 2^+ energies, Grodzins [14,15] derived the following empirical relation:

$$E(2_1^+) = \frac{1225 \text{ MeV}}{\beta_2^2 A^{7/3}} \tag{1.2}$$

Near major shell closures, nuclei are near-spherical, $\beta_2 \approx 0$, and $E(2_1^+)$ values are large relative to neighboring even-even isotopes as shown by Eq. 1.2. As nucleons are added or removed from a closed shell, $E(2_1^+)$ will decrease, a result of the dominance of collective interactions among nucleons. As stated earlier, collective excitations should

be maximum at midshell. However, the development of collectivity away from major closed shells may be inhibited by the presence of subshell closures, or minor shell gaps.

Although the energy gaps between single-particle orbitals for subshells are not as dramatic as major shell closures, $\Delta E \approx 2$ MeV as opposed to > 3 MeV [16], the properties exhibited by nuclei at or near subshell closures resemble those near major shell closures. For instance, similar to shell gaps, the structure of nuclei near minor shells are expected to be spherical, thus inhibiting the development of quadrupole deformation within a major shell. Therefore, in regions where one may expect large deformations, the contrary may be observed. The existence of subshells between major shell closures should result in similar $E(2_1^+)$ trends.

As an example, the $E(2_1^+)$ systematics for even-even $N = 50$ isotones are shown in Fig. 1.7a. The depicted $E(2_1^+)$ values were obtained from Ref. [9,17]. Although the major proton shell spans from $Z = 28 - 50$, there is a clear increase in $E(2_1^+)$ at ^{90}Zr, $Z = 40$. This peak in $E(2_1^+)$ suggests a substantial energy gap between the $\pi 2p_{1/2}$ and $\pi 1g_{9/2}$ single-particle orbitals, indicative of a $Z = 40$ subshell. An inspection of the $E(2_1^+)$ values for neutron-rich, even-even zirconium isotopes reveals a similar peak at $N = 56$ (see Fig. 1.7b). Sadler *et al.* [18] have suggested that the significant energy gap between the $\nu 2d_{5/2}$ and the $\nu 1g_{7/2}$ orbitals may be attributed to the $N = 56$ subshell. Thus, by examining the systematics of the $E(2_1^+)$ values, one may explore new features in nuclear shell structure, i.e. the development of quadrupole collectivity away from shell closures, the presence of subshell closures and changes in major shell closures away from beta stability.

1.4.2 Ratio of $E(4_1^+)$ to $E(2_1^+)$

Another method of exploring quadrupole collectivity in nuclear systems is by examining the ratio of the first excited 4^+ to 2^+ states. This ratio indicates the type of deformation a nuclear system undergoes, whether it may be vibrational or rotational.

Time averaged, a vibrationally deformed nucleus would appear spherical, as the

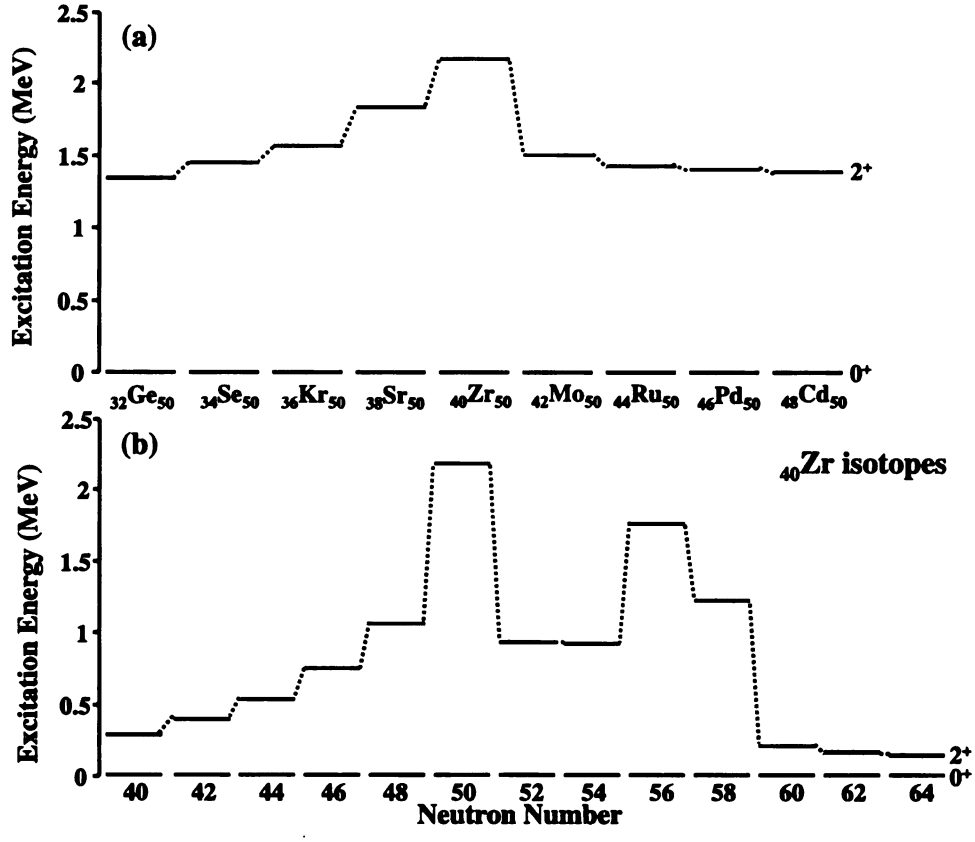

Figure 1.7: $E(2_1^+)$ systematics for (a) even-even $N = 50$ isotones and (b) neutron-rich zirconium isotopes. The $E(2_1^+)$ values for Ge to Pd were obtained from Ref. [9,17] and Cd from Ref. [18].

system undergoes dynamic shape deformations. Such a system may be identified by examining the systematics of $E(4_1^+)/E(2_1^+)$. In a vibrationally deformed system, the energy of the phonon state is:

$$E_{vib} = (v + 1/2)\hbar\omega \tag{1.3}$$

where $v = 0, 1, 2,..., \omega = (k/\mu)^{1/2}$, k is the force constant and μ is the reduced mass. Thus, each of the states would be separated by an energy of $\hbar\omega$. In an even-even nuclear system, the first excited 2^+ state should be the lowest excited state, followed by a degenerate triplet of states, 0_2^+, 2_2^+ and 4_1^+ state. For an axially symmetric, vibrationally active system the $E(4_1^+)$ to $E(2_1^+)$ ratio should be ≈ 2.

As one continues to move away from major shell closures, the nucleus becomes increasingly deformed. As more valence nucleons become available, collective interac-

tions enhance. The nucleus undergoes a transition from dynamic to static deformation with the onset of rotational motion. In a rotationally deformed system, the energy of a given state is:

$$E_{rot} = \frac{\hbar^2 J(J+1)}{2I} \propto J(J+1) \tag{1.4}$$

where I is the moment of inertia, $\sum_i \mu_i r_i^2$, μ_i is the reduced mass of particle i, r_i is the perpendicular distance of particle i to the axis of rotation and J is the spin of the state. Based on this equation, a rotationally deformed axially symmetric system has a ratio of the first excited 4^+ state to the first excited 2^+ state ≈ 3.3.

1.5 Motivation

The aim of the present work was to explore the development of quadrupole collectivity for neutron-rich species within the $N = 28 - 50$ major shell. This shells extends over 22 neutrons, thus one would expect very deformed nuclear systems at midshell. However, the $N = 28 - 50$ shell has been shown to exhibit interesting features. For example, a clear increase in $E(2_1^+)$ at $N = 40$, $Z = 28$ (see Fig. 1.8, data from Ref. [1, 9, 19, 20]) has been observed by Broda *et al.* [1]. They suggested this peak was the result of an $N = 40$ subshell closure for nickel, which would inhibit the development of collectivity in this midshell region. Although a peak in $E(2_1^+)$ is not apparent at $N = 40$ for Fe, Zn or Ge, this may be due to the predominately proton nature of their configurations.

If $N = 40$ is indeed a viable subshell closure, then the $N = 28 - 50$ shell is effectively split into two subshells, $N = 28 - 40$ and $N = 40 - 50$, which inhibits the full development of collectivity in this major shell. To determine the robustness of the $N = 40$ subshell, neutron-rich species near $N = 40$ were explored in this work. One such nuclide was $^{69}_{29}Cu_{40}$, which was produced by the beta decay of $^{69}_{28}Ni_{41}$. If $N = 40$ is a good subshell closure, then the properties of ^{69}Cu could be described by the extreme single-particle shell model as a proton coupled to a ^{68}Ni core. Details of this study will be discussed in section 5.1.1.2.

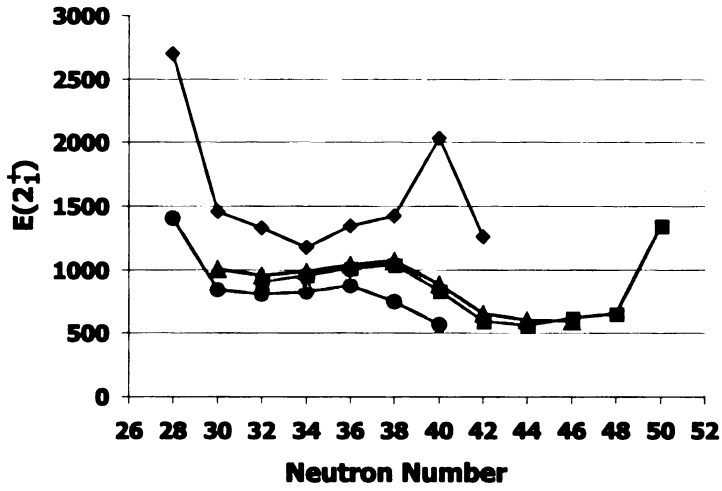

Figure 1.8: The first excited 2^+ energies for Fe (orange circles), Ni (green diamonds), Zn (blue triangles) and Ge (purple squares) as a function of neutron number. Data were taken from Ref. [1,9,19,20]. Please note that images in this dissertation are presented in color.

To investigate whether the $N = 40$ subshell strengthens for increasingly neutron-rich nuclides, an extension of the $N = 40$ study to lighter mass systems was of interest. Therefore, neutron-rich species within the $N = 28 - 40$ midshell were examined. Similar to major shells, collectivity should be at a maximum in the middle of a subshell. Thus, one would expect deformed nuclear systems in the middle of the $N = 28 - 40$ subshell. However, following the β-decay study of ^{58}V, new empirical evidence for an $N = 32$ subshell was observed. Such discoveries warrant the need for further experimental studies into nuclear structure. Much of what is known about the properties of radioactive species approaching or near the neutron drip-line has been attained through the extrapolation of experimentally derived measurements of stable nuclei. By experimentally probing regions away from stability, theorists are presented with new data to check and refine their current models to better predict the properties of nuclei away from the valley of stability.

For this study, it was of interest to populate the first excited 2^+ and 4^+ states in neutron-rich nuclides in the $N = 28 - 40$ subshell. As discussed above, the first excited 2^+ and 4^+ states are key to unveiling the structure of the atomic nucleus. The

method that was utilized to populate these states was β decay.

Chapter 2

Technique

An important technique for studying the properties of neutron-rich nuclei is beta-delayed gamma ray spectroscopy. Using this method, a nuclide of interest is produced following the beta decay of its ${}^{A}_{Z-1}X_{N+1}$ parent. During the course of beta decay, the parent nuclide may populate an excited nuclear state in the daughter. When this state de-excites, a gamma ray is emitted, providing a measure of the exact energy difference between nuclear states. By correlating the observed gamma ray transitions, one may construct an energy level scheme for the daughter nucleus.

2.0.1 Beta Decay

Beta decay is a radioactive decay process that involves the transformation of a neutron (proton) within the nucleus into a proton (neutron). In addition, two particles are emitted, a beta particle, which is a fast electron that originates in the nucleus, and a neutrino, an electrically neutral subatomic particle. Although the atomic number and neutron number will change by $Z + (-) 1$ and $N - (+) 1$ during this process, the mass number, A, will remain constant.

There are three types of beta decay processes:

1. Electron capture : ${}^{A}_{Z}X_{N} + e^{-} \rightarrow {}^{A}_{Z-1}Y_{N+1} + \nu + Q_{EC}$

2. β^{+} decay : ${}^{A}_{Z}X_{N} \rightarrow {}^{A}_{Z-1}Y_{N+1} + \beta^{+} + \nu + Q_{\beta+}$

3. β^{-} decay : ${}^{A}_{Z}X_{N} \rightarrow {}^{A}_{Z+1}Y_{N-1} + \beta^{-} + \bar{\nu} + Q_{\beta-}$

where e^{-} is an electron, $\beta^{\pm}$ are beta particles, ν is a neutrino, $\bar{\nu}$ is an anti-neutrino

and Q_β is the difference between the initial and final nuclear mass energies [3]. Both β^+ decay and electron capture occur in nuclides that are neutron-deficient, however, they may not both be energetically possible. In order for beta decay to occur, the decay energy, Q_β, must be greater than zero.

In electron capture, the nucleus captures an atomic electron, producing a bound neutron. The only particle emitted from the nucleus following this process is a neutrino. As the mass of a neutrino is extremely small, $\geq$ 0.1 eV [21,22], it is nearly impossible to observe this particle. In reality, electron capture is tracked not through primary particle emission, but rather secondary. When the atomic electron is captured, it leaves a vacancy in the electron shell (typically the K shell). This is an unstable electronic configuration, and the electrons quickly reconfigure. A higher-lying electron de-excites to fill the vacancy and in the process gives rise to either detectable x-rays or Auger electrons.

When the Q_β value is greater than $2m_ec^2$, twice the rest mass of an electron, β^+ decay becomes energetically possible. During this process, a bound proton is converted to a bound neutron. In addition, a neutrino and a β^+ particle are emitted. In β^+ decay, the beta particle is a positively charged electron, a positron. Since neutrinos are nearly undetectable, β^+ decay is monitored through the emission of positrons. Positrons are very reactive species. Unbound, they quickly combine with an electron and annihilate, emitting two 0.511 MeV photons in opposite directions. In addition, β^+ particles may be directly observed. Beta particles will interact directly with atomic electrons within the detection material.

When the neutron-to-proton ratio in a nucleus is significantly larger than the ratio of the stable isobar, β^- decay is possible. During this process, a bound neutron is converted to a bound proton. In addition, a β^- particle (an electron) and an anti-neutrino are emitted. To monitor such a decay, the β^- particle must be observed. As in the case of β^+ decay, these particles are detected as they interact directly with the orbital electrons within the detection medium. For the present study, β^- decay will be the decay mode of interest.

By monitoring beta activity, the half-life of the initial decaying nuclide (the mother) may be deduced. The half-life is the time over which the initial number of atoms is reduced on average by one half [23]. Consider the first-order rate law,

$$\frac{d[N]}{dt} = -\,[N]\,\lambda \Longrightarrow \frac{N}{N_o} = \epsilon^{-\lambda t} \tag{2.1}$$

where N and N_o represent the final and initial number of atoms of a given radioactive species and λ is the rate constant. At $N/N_o = 1/2$,

$$t \;=\; t_{1/2} \;=\; \frac{\ln 2}{\lambda}. \tag{2.2}$$

β-decay half-lives typically range from a few milliseconds to seconds or longer. This time is dependent on the differences in the spin, parity and energy of the original and final state to which the mother decays. During the process of beta decay, two particles, an electron and a neutrino, are emitted from the nucleus. Each particle has a spin of 1/2 and can carry orbital angular momentum. If their spins are anti-parallel ($\uparrow\downarrow$, S = 0), the nuclear system will undergo a Fermi decay [3]. In an allowed/favored Fermi decay, the electron and neutrino are emitted with zero units of orbital angular momentum. Thus, there will be no change in the nuclear spin, $\Delta J = |J_i - J_f| = 0$. In addition, when $\ell = 0$, the parities of the final and initial states will be the same, $\pi = (\text{-}1)^{\ell}$. If an electron and a neutrino have their spins aligned parallel ($\uparrow\uparrow$ or $\downarrow\downarrow$, S = 1), then the system may experience a Gamow-Teller decay [3]. For an allowed Gamow-Teller decay, the electron and neutrino must carry away one unit of angular momentum. Thus,

$$^{A}_{Z}X \rightarrow \; ^{A}_{Z+1}Y + (\beta^{-} + \bar{\nu}) \tag{2.3}$$

$$\vec{J}_i = \vec{J}_f + \vec{1} \tag{2.4}$$

and

$$|J_f - 1| \leq J_i \leq J_f + 1, \;\; \Delta J = 0, 1 \tag{2.5}$$

As for allowed Fermi decays, the initial and final states following an allowed Gamow-Teller decay will have the same parity ($\Delta\pi$ = no).

Allowed β-decay transitions are among the fastest. However, it is also possible to undergo beta transitions in which $\Delta J > 1$ and/or the initial and final states have opposite parities. These transitions are classified as "forbidden." Unlike the name suggests, forbidden transitions are feasible, however, they are slower than allowed transitions. Table 2.1 provides a list of known β-decay transitions and a corresponding $\log ft$ range. $\log ft$ values can be used to provide a comparative half-life for a given transition. The $\log f$ term corrects the half-life measurement for the atomic number of the daughter and the maximum energy of the beta transition [23], due to the atomic interactions of the emitted electron,

$$\log f_{\beta-} = 4.0 \ \log E_{max} + 0.78 + 0.02 \ Z - 0.005 \ (Z - 1) \ \log E_{max} \qquad (2.6)$$

where E_{max} is the difference in energy in MeV of the initial state in the mother and the final state in the daughter and Z is the atomic number of the beta daughter. $\log t$ is the logarithm of the partial half-life for the beta decay branch to a given state,

$$T_{1/2}^{partial} = \frac{T_{1/2}^{total}}{BR} \qquad (2.7)$$

where BR is the branching ratio. Although some beta transitions may be classified as pure Fermi or Gamow-Teller decays, beta decays may also be characterized as mixed Fermi and Gamow-Teller transitions.

2.0.2 Beta-Delayed Gamma Ray Transitions

Following β-decay, the daughter nuclide may be left in an excited state. This state will de-excite through the emission of one or more photons, either directly or through a cascade of gamma rays to the ground state. The emission of gamma radiation is the result of changes in the charge and current distribution of the nucleus [23]. These changes give rise to electric and magnetic moments, respectively. Thus, γ-ray transitions may be classified as electric or magnetic in nature. Similar to beta particles, γ-rays may carry orbital angular momentum as they are emitted from an excited nuclear state. In general, the favored transitions are associated with the transfer of

Table 2.1: Selection rules for beta decay transitions [23].

Type	ΔJ	$\Delta \pi$	$\log ft$
Superallowed	0,1	No	3
Allowed (normal)	0,1	No	4-7
Allowed (ℓ-forbidden)	1	No	6-12
First forbidden	0,1	Yes	6-15
First forbidden (unique)	2	Yes	9-13
Second forbidden	2	No	11-15
Second forbidden (unique)	3	No	13-18
Third forbidden	3	Yes	17-19
Third forbidden (unique)	4	Yes	
Fourth forbidden	4	No	~23
Fourth forbidden (unique)	5	No	

the lowest amount of angular momentum. Gamma rays ejected with $\ell = 1, 2, 3, 4, \lambda\,\hbar$ of angular momentum are referred to as dipole, quadrupole, octupole, hexadecapole and 2^{λ}-pole radiation.

Transitions may be electric, magnetic or a combination of electric and magnetic in character. Electric and magnetic transitions may be differentiated by the relative parities of the initial and final states. Following an electric transition, the initial and final nuclear states will experience a change in parity when the emitted gamma ray carries off an odd value of angular momentum. In a magnetic transition, the initial and final states will have opposite parities if the gamma ray is emitted with an even unit of angular momentum. Thus, the selection rules for a gamma ray transition are as follows:

$$|J_i - J_f| \leq \lambda \leq |J_i + J_f| \tag{2.8}$$

$$\Delta\,\pi(E) = (-1)^{\lambda} \tag{2.9}$$

$$\Delta\,\pi(M) = (-1)^{\lambda+1} \tag{2.10}$$

A reasonable single-particle estimate for electromagnetic transition rates may be

calculated as follows [24]:

$$T_W(E\lambda) = \alpha\hbar c\frac{8\pi(\lambda+1)}{\lambda[(2\lambda+1)!!]^2}\frac{1}{\hbar}(\frac{1}{\hbar c})^{2\lambda+1}E^{2\lambda+1}B_W(E\lambda) \tag{2.11}$$

$$T_W(M\lambda) = \alpha\hbar c(\frac{\hbar}{2M_pc})^2\frac{8\pi(\lambda+1)}{\lambda[(2\lambda+1)!!]^2}\frac{1}{\hbar}(\frac{1}{\hbar c})^{2\lambda+1}E^{2\lambda+1}B_W(M\lambda) \tag{2.12}$$

where α is the fine structure constant ($\approx 1/137$), c is the speed of light (2.998 x 10^{23} fm/s), M_p is the mass of a proton (938.3 MeV/c^2), $\hbar$ is Planck's constant divided by 2π (6.582 x 10^{-22} MeVs), λ is the multipole order and $B_W(E\lambda)$ and $B_W(M\lambda)$ are the Weisskopf single-particle estimates to the λ^{th} multipole reduced transition probability. The reduced transition probabilities are defined as:

$$B_W(E\lambda) = \frac{1}{4\pi}(\frac{3}{\lambda+3})^2(1.2)^{2\lambda}A^{\frac{2\lambda}{3}}e^2fm^{2\lambda} \tag{2.13}$$

$$B_W(M\lambda) = \frac{10}{\pi}(\frac{3}{\lambda+3})^2(1.2)^{2\lambda-2}A^{\frac{2\lambda-2}{3}}\mu_N^2fm^{2\lambda-2} \tag{2.14}$$

where μ_N is the nuclear magneton, $\frac{e\hbar}{2M_p}$. The transition rates are calculated in inverse seconds. Transition rates can also be expressed in Weisskopf units. One Weisskopf unit for a λ^{th} multipole is equivalent to $1B_W(E\lambda)$ or $1B_W(M\lambda)$ depending upon whether the transition is electric or magnetic. Deviations from the single-particle estimate of the transition rates are calculated as the ratio of the experimentally extracted reduced transition probability and the single-particle estimate, B_{exp}/B_W. In addition, one may predict the lifetime of an isomeric state, a long-lived excited nuclear state, by multiplying the inverse of the transition rates by ln 2. Table 2.2 lists the Weisskopf single-particle estimates for the reduced transition probabilities and Eλ and Mλ transition rates for several multipolarities, where E_γ is in units of MeV.

2.0.3 Summary

To investigate subshell gaps in the midshell region of $N = 28 - 50$, beta-delayed gamma ray spectroscopy was utilized. Using this technique, a nuclide of interest was produced by the β^- decay of its (Z - 1), (N + 1) parent. Since beta decay is a selective decay process following the rules indicated in Table 2.1, states in the daughter nuclide

Table 2.2: Weisskopf single-particle reduced transition probabilities and estimated transition rates [24].

λ	$B_W(E\lambda)$ $(\epsilon^2 fm^{2\lambda})$	$B_W(M\lambda)$ $(\mu_N^2 fm^{2\lambda-2})$
1	6.446 x 10^{-2} $A^{2/3}$	1.790
2	5.940 x 10^{-2} $A^{4/3}$	1.650 $A^{2/3}$
3	5.940 x 10^{-2} A^{2}	1.650 $A^{4/3}$
4	6.285 x 10^{-2} $A^{8/3}$	1.746 A^{2}
5	6.929 x 10^{-2} $A^{10/3}$	1.925 $A^{8/3}$
λ	$T_W(E\lambda)$ (s^{-1})	$T_W(M\lambda)$ (s^{-1})
1	1.025 x 10^{14} E_γ^3	3.157 x 10^{13} E_γ^3
2	7.279 x 10^{7} E_γ^5	2.242 x 10^{7} E_γ^5
3	3.391 x 10^{1} E_γ^7	1.044 x 10^{1} E_γ^7
4	1.066 x 10^{-5} E_γ^9	3.284 x 10^{-6} E_γ^9
5	2.396 x 10^{-12} E_γ^{11}	7.378 x 10^{-13} E_γ^{11}

are preferentially populated if their spin, J_f, is equal to the spin of beta decaying parent state, J_i or if $J_f = |J_i \pm 1|$. In addition, in allowed beta decay transitions the parities of the parent and daughter states are the same ($\Delta\pi$ = no).

Beta decay may populate an excited nuclear state in the daughter. As this state de-excites, a gamma ray is emitted. The goal of this study was to populate the first excited 2^+ and the first excited 4^+ states via beta decay of even-even neutron-rich nuclei in the $N = 28 - 40$ subshell. The energies of the 2_1^+ and 4_1^+ states would be useful in extracting structural information concerning the nuclides of interest.

Chapter 3

Experimental Setup

3.1 Production of Radioactive Beams

With the exception of several long-lived transuranic isotopes and a few other common radionuclides (i.e. ^{40}K and ^{14}C), radioactive nuclides are not readily available on earth. In nature, these nuclides are produced within a stellar media during the course of their evolution. One method of producing radioactive nuclides within a laboratory setting is using a technique known as projectile fragmentation. The National Superconducting Cyclotron Laboratory (NSCL) at Michigan State University is one of several facilities worldwide that utilizes this method for the production of radioactive beams. This technique, at the NSCL, entails the acceleration of a primary, stable beam within the K1200 cyclotron. Once the primary beam has been accelerated to a sufficient energy, it is impinged upon a thick, stable target (typically ^{9}Be). As a result of this collision, the target will abrade nucleons from the initial projectile producing both stable and radioactive secondary beams ranging from the A and Z of the primary beam to hydrogen. To study the decay properties of a given subset of secondary beams, these nuclides must be isolated from the other reaction products. This separation was achieved by transporting the secondary fragments through the A1200 fragment analyzer [25]. The A1200 was designed to be achromatic, with two intermediate images between two sets of dipoles, whose bending radii were in opposite directions. Momentum slits were inserted at the first dispersive image to filter nuclides based on their momentum to charge (p/q) ratio. In addition, an aluminum

wedge was placed at the second dispersive image of the device to purify the secondary beams. This was accomplished by differentially degrading the energy of the secondary fragments as they traverse the wedge. By inserting a position slit at the focal point of the fragment separator, further constraints were placed on the secondary fragments, limiting the number of transmitted fragments.

Once the secondary beams of interest were isolated from the other reaction products, they were transported through the Reaction Products Mass Separator (RPMS) and finally to the S2 experimental vault where the beta detection system was located. The RPMS may be used to provide mass/charge separation of secondary fragments, however, during the two studies that will be discussed, the RPMS was not utilized for this purpose. Although some separation was achieved by applying a voltage of $\pm$ 140 kV to the Wien filter, position slits were not inserted at the end of the RPMS. Therefore, for all practical purposes, the RPMS can be viewed as a beamline connecting the S1 and S2 vaults.

3.2 Beta Detection System

3.2.1 Pulsed Beam Method, Experiment 97004

In conventional beta detection systems, a radioactive beam is implanted within a collection target for an implantation time, $t_{implant}$. The beam is then inhibited for a period t_{decay} when the bulk activity of the beta decaying implants is monitored with a series of beta detectors surrounding the implantation foil. For this particular study, the collection foil was mounted on a rotating target wheel. The target wheel was 40 cm in diameter with nine Al collection foils, 165 mg/cm^2 in thickness and 5 cm in diameter, equally spaced along its circumference [26]. The wheel was aligned at an angle of 45^o with respect to the beam axis and located downstream from the end of the beam line, which was sealed with a kapton window. Two 3 mm plastic scintillators coupled to photomultiplier tubes were used to monitor the emission of β particles. In addition, two high-purity Ge (HPGe) detectors with 80 and 120%

photopeak efficiency relative to a 3" × 3" cylindrical NaI(Tl) crystal were utilized for the detection of γ-rays. One plastic scintillator-Ge pair was aligned parallel to the beam axis and approximately 40 mm from the center of the collection foil. The second plastic scintillator-Ge pair was located directly behind the collection foil, such that the Ge detector was 15 mm from the center of the foil. In this orientation, a total β efficiency of 40(2)% and a peak γ-ray efficiency of 4.5% at 1.274 MeV was attained (see discussion in Appendix A–B).

Further upstream from the beta detection system was a 300 μm Si PIN detector. Secondary fragments were identified by their energy loss within this Si detector and their time of flight (TOF) from a plastic detector inserted at the first dispersive image of the A1200. Particle identification was also determined at the focal plane of the A1200 where a second 300 μm Si PIN detector was located. In addition, a parallel plate avalanche counter (PPAC) was placed upstream from the beta detection system. The PPAC detector consists of two parallel plate electrodes separated by a small gap [27]. The electrodes are encased between two thin mylar windows in a container filled with iso-octane gas at a pressure of $\approx$ 5 torr. This gas-filled cell was used to determine the position of the secondary beams as they passed through the detector. Figure 3.1 is a schematic of the detector endstation used for this experiment.

A cocktail beam consisting of 5.2% ^{67}Co, 18.8% ^{69}Ni, 12.9% ^{71}Cu, 25.7% ^{72}Zn and 37.4% of ^{68}Ni + ^{70}Cu was produced following the fragmentation of a 70 MeV/nucleon $^{76}Ge^{19+}$ beam, provided by the K1200 cyclotron, in a 202 mg/cm^2 Be target. The primary beam current was $\approx$ 1.6 enA, resulting in the production of ^{69}Ni at a rate of 86.7 s^{-1}. The magnetic rigidity, Bρ, of the dipole magnets of the A1200 fragment analyzer were set to 2.505 Tm and 2.250 Tm, respectively. B represents the magnitude of the magnetic field and ρ is the radius of curvature of the fragments as they traverse the $\vec{B}$ field. The full momentum acceptance of the A1200 was set to 0.5% using momentum slits at the first dispersive image of the device. A 70 mg/cm^2 Al degrading wedge was inserted at the second dispersive image of the A1200 to separate the fragments of interest from other reaction products following fragmentation.

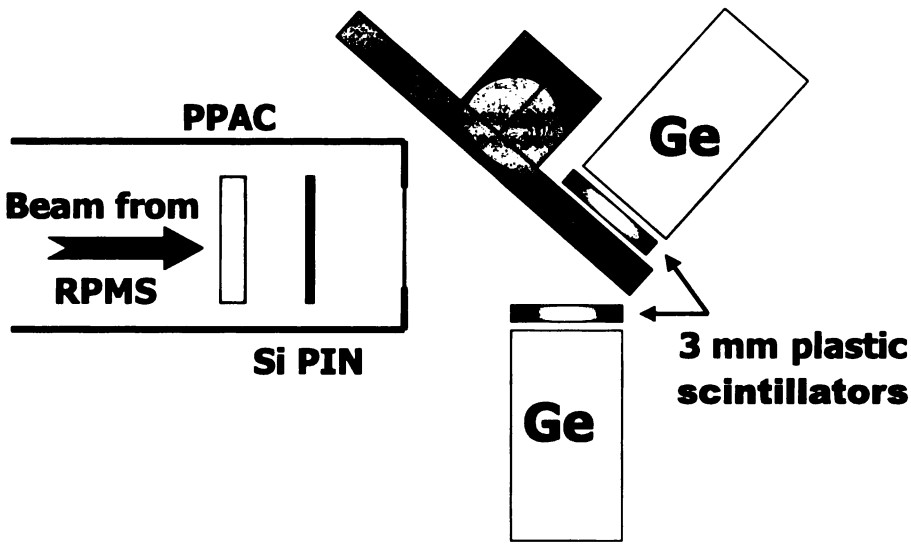

Figure 3.1: Schematic diagram of the beta detection system utilized in experiment 97004.

To study the beta decay properties of the nuclides of interest, the secondary beams were transported to the experimental endstation. After penetrating the PPAC detector and the Si PIN detector, the fragments were transported through a kapton barrier which separated the beam-line vacuum from the beta detection system that was at atmospheric pressure. The secondary fragments were implanted within one of the nine aluminum collection foils of the rotating target wheel for $t_{implant}$ = 24 s. The beam was then pulsed off for 36 s. Once this cycle was completed, the target wheel was rotated to a new collection foil using a stepper motor whose controller was interfaced with the data acquisition system. The rotation of the target wheel required 250 ms. A second pulsing sequence was used with $t_{implant}$ = 4 s and t_{decay} = 4 s to measure the half-lives of short-lived radioactive species. Data were collected only during the implantation and decay periods.

Using a second tune of the A1200, a different subset of nuclides were produced. The new Bρ setting for the second set of dipole magnets, 2.245 Tm, and a slightly larger full momentum acceptance, 1%, produced a cocktail beam of ^{68}Co, ^{69,70}Ni, ^{71,72}Cu and ^{73}Zn. For the second tune, several different $t_{implant}/t_{decay}$ sequences were used: 1.7 s/1 s, 1 s/1 s, 24 s/36 s, 0.3 s/0.3 s and 33 ms/100 ms.

3.2.1.1 Electronics

Figures 3.2 and 3.3 show the electronics diagram used for experiment 97004. The master gate was triggered by an event above threshold in either the germanium detectors, the plastic scintillators or the PIN detector. The master gate trigger from the PIN detector was downscaled by a factor of ten to prevent these triggers from dominating the master gate, as the beam implantation rate was rather high ($\approx$ 1000 particles/sec). $\beta - \gamma$ coincidence events were identified, in software, as events that triggered one of the plastic scintillators and the non-adjacent Ge detector.

3.2.2 Continuous Implantation Method, Experiment 98020

Although the conventional beta detection method has proven to be quite useful in extracting beta decay information for radioactive species, it has two shortcomings. In this technique, (1) the bulk activity of the implanted species is monitored rather than monitoring the activity on a nuclide-by-nuclide basis; and (2) the beam is pulsed. Cycling the beam on and off reduces the overall counting statistics. To avoid these two limitations, a new beta detection system was developed. This system employed a Micron Semiconductor Ltd. type BB1 double-sided silicon strip detector (DSSD). The DSSD is a single silicon wafer segmented in 40 1-mm wide strips in both x and y dimensions, yielding 1600 pixels. These 1600 pixels behaved as 1600 individual detectors. A bias of -140 V was applied to the front of the strip detector, resulting in the collection of holes on the front and electrons on the back of the detector. The purpose of using this new beta detection system was to take advantage of the high pixelation of the microstrip detector to continuously implant short-lived activities over as much of the active area of the detector as possible and correlate implant and subsequent beta decays on an event-by-event basis. A 985-μm thick DSSD was selected to ensure sufficient Si for the detection of high-energy beta particles expected from the decay of nuclei far removed from the line of β stability. The DSSD was positioned between two 5 cm $\times$ 5 cm Si PIN detectors, placed at a distance of 1.9 cm and

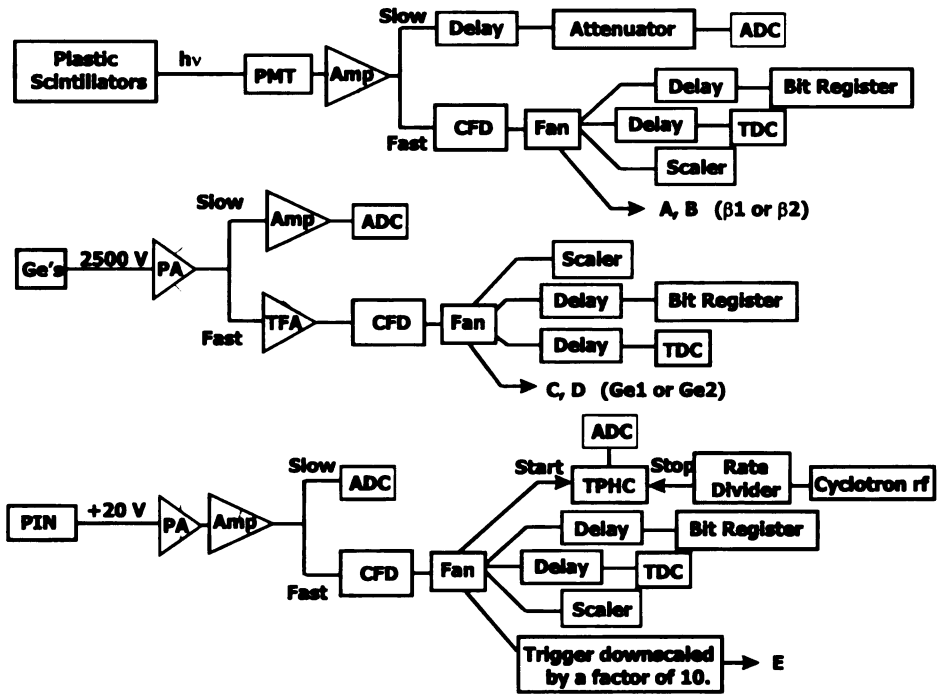

Figure 3.2: Plastic scintillator, Ge and PIN electronic diagrams for experiment 97004.

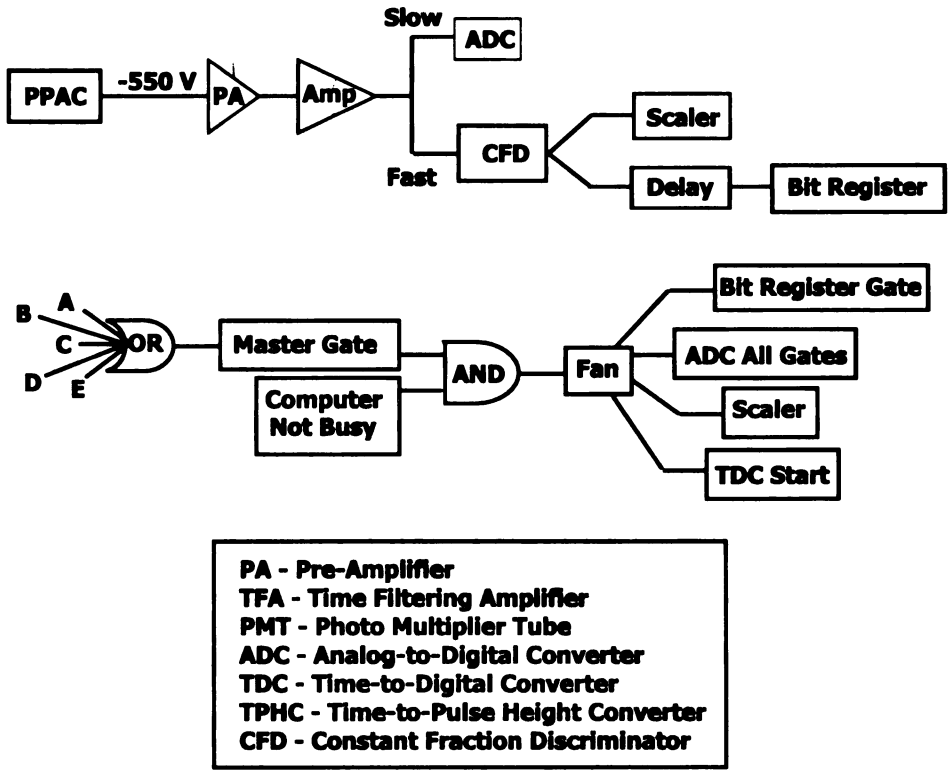

Figure 3.3: PPAC and master gate electronic diagrams for experiment 97004.

2.2 cm, respectively from the center of the DSSD. The upstream PIN detector had a thickness of 503 μm, while the downstream detector was 309 μm thick. The PIN detectors and the DSSD were mounted on an ISO-160 flange for easy coupling to the beam-line vacuum. Two 50-pin feed-throughs on this flange were used to bring the DSSD signals to a grounding board placed immediately outside the vacuum chamber. The grounding board provided a common ground for each output channel and six 34-way ribbon cables to transmit the DSSD output to the shaping amplifiers.

During this experiment, NSCL fabricated preamplifiers with gains of 60 mV/MeV and rise and fall times of 50 ns and 100 μs, respectively, were utilized. These pre-amps were chosen because of their high gain and short rise time, which was necessary to trigger the electronics, namely the constant fraction discriminators (CFD's), on the DSSD signals. In an earlier test run, preamplifiers obtained from Washington University were used. Although these pre-amps were equipped with both fast (τ_{rise} = 7 ns and τ_{fall} = 200 ns) and slow (τ_{rise} = 1 μs and τ_{fall} = 100 μs) outputs, only the slow output signals were processed. The noise level from the fast output was considerably larger than that from the slow output, 125 mV peak-to-peak as compared to 3 mV peak-to-peak. Although the slow pre-amp signals were originally teed to provide both energy and timing signals for each DSSD channel, the signals could not trigger the CFD's due to their relatively long rise time.

The pre-amps, the DSSD and the vacuum chamber were all on a common electrical ground. The NSCL pre-amp signals were teed to yield an energy and time signal for each DSSD channel. The energy signal was recorded by processing the pre-amp output through a variable gain Washington University CAMAC shaper and then digitalized using a Philips 7164H ADC in CAMAC. Each of the 80 channels of electronics from the DSSD (40 strips x and y) were gain matched using high-energy alpha peaks from a ^{232}U source. A timing signal was produced by first passing the pre-amp output through a fast amplifier. The amplified signal was sent through a Lecroy 3420 CFD with 100 ns delay chips. This signal was delayed 100 ns and teed to provide inputs for a Lecroy 4434 scaler, a Lecroy 4448 coincidence register and a Philips 7186H time-

to-digital converter (TDC). The master gate, defined as any trigger from the DSSD, served as a common start for the TDC.

Further upstream from the PIN-DSSD-PIN detector telescope was a 300 μm Si PIN detector. This Si detector provided energy loss and, in conjunction with the cyclotron radio frequency, time of flight (TOF) necessary for particle identification. In addition, two PPAC's were placed upstream from the silicon telescope. The PPAC detectors were used for beam diagnostics, providing information concerning the beam position.

Gamma ray emission was monitored by an array of Ge detectors. A 120% HPGe detector was positioned directly behind the ISO-flange. In addition, an 80% HPGe detector and three HPGe clover detectors (each Ge crystal within the clover had a relative efficiency of $\approx 25\%$) were oriented in the plane perpendicular to the beam axis. The 80% HPGe detector was placed 8.5 cm from the center of the DSSD at an angle of 104^{o} relative to the beam line. The three clover detectors were 8.1 cm from the center of the DSSD, offset by an angle of 4^{o} relative to perpendicular. A depiction of the experimental endstation is shown in Figure 3.4.

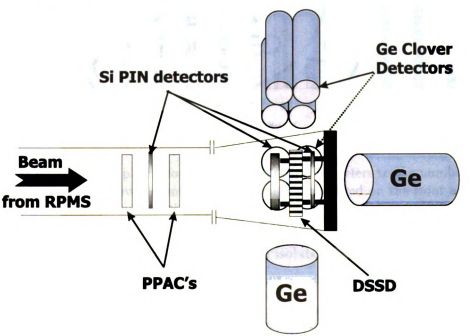

Figure 3.4: Schematic diagram of the detector positions for experiment 98020.

As a consequence of using single, high-gain electronics to process the DSSD energy signals, the high-energy implant events (E > 17 MeV) fell outside the maximum input voltage range of the ADC's and were recorded as overflow events. Moreover, the large pre-amp signal for a given strip induced signals in neighboring channels. This resulted in an implantation multiplicity greater than one in both the front and back channels. An average multiplicity of six in both x and y were recorded for a given implant event within the DSSD (see Fig. 3.5). To determine the pixel of each implant, the sum of consecutive strip numbers recording an overflow were tallied and divided by the multiplicity for both the front and back of the DSSD. The most central pixel in the overflow array, along with its i±1 neighbors, where i is the implant strip, were identified as the implant pixels.

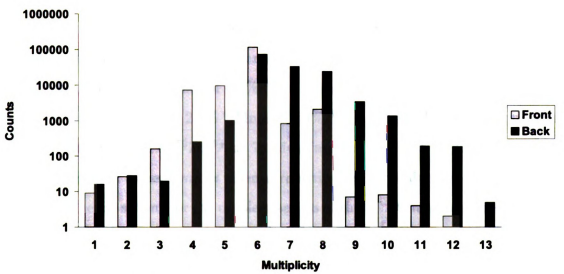

Figure 3.5: Implant multiplicity for the DSSD. Multiplicity refers to the number of strips that were triggered for a given event. On average, six strips fired on the front and back of the strip detector during implantation.

Unlike implant events, beta events could be isolated to the nearest pixel (see Fig. 3.6). This was due to the fact that the emitted beta particles were far less energetic than the implanted ions. In addition, rather than depositing their full energy within the DSSD, the beta particles were depositing a fraction of their total energy, ΔE, as they were emitted from a given pixel in the DSSD. These beta decays were then

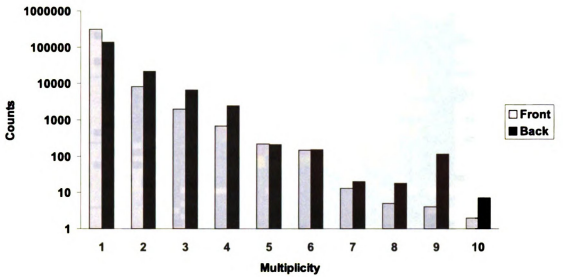

Figure 3.6: Decay multiplicity for the DSSD.

correlated with previously identified implants within a given pixel. Neighboring i±1 pixels that had been labelled as implants for the same event were then zeroed.

A cocktail beam consisting of 0.3% ^{54}Sc, 1.5% ^{55}Ti, 2.6% ^{56}Ti, 37.1% ^{57}V, 1.9% ^{58}V, 3.8% ^{58}Cr, 47.2% ^{59}Cr, 2.1% ^{60}Mn and 3.4% ^{61}Mn was produced by fragmenting a primary, stable beam of $^{70}Zn^{18+}$ at 70 MeV/nucleon in a 155 mg/cm^2 ^{9}Be target. The primary beam current was $\approx$ 40 enA, resulting in the production of ^{57}V at a rate of 240 s^{-1}. The Bρ setting for the dipole magnets of the A1200 fragment analyzer were 2.771 Tm and 2.645 Tm. The full momentum acceptance of the A1200 was set to 0.5% using momentum slits at the first dispersive image of the device. A 70 mg/cm^2 Al degrading wedge was inserted at the second dispersive image of the A1200 to separate the fragments of interest from other reaction products following fragmentation. The secondary beams were then transported through the RPMS to the S2 vault where the experimental endstation was located. On average, ions were implanted into the strip detector at a rate no greater than 100 s^{-1}. The secondary beam was defocused in both x and y to illuminate $\approx$ 2/3 of the active detector area. This beam profile, shown in Fig. 3.7, resulted in an average two-second time window between successive implants in the central most portion of the DSSD, ample time for measuring half-lives

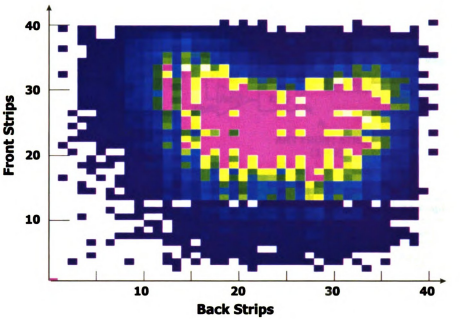

Figure 3.7: Beam profile on the strip detector.

of the nuclides of interest.

3.2.2.1 Electronics

A schematic of the electronics diagram is depicted in Fig. 3.8–3.10. The master gate was triggered by an event above threshold in the x and y strips of the DSSD. Implant events were identified in software as any event that triggered the strip detector and the first PIN detector without firing the third PIN detector. Decay events were identified in software as events that triggered the strip detector and either the second or third PIN detector without firing the first PIN detector.

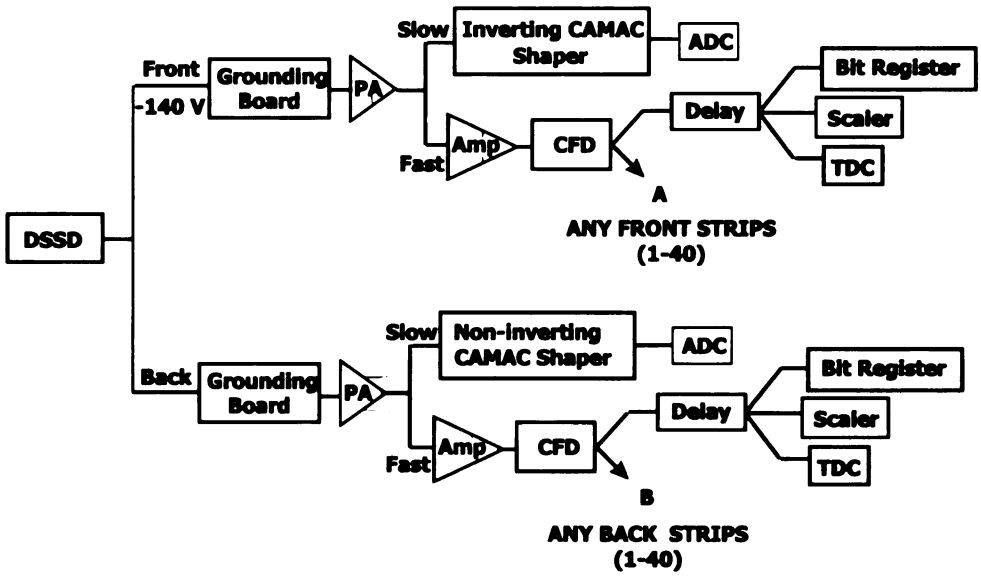

Figure 3.8: DSSD electronics diagram for experiment 98020.

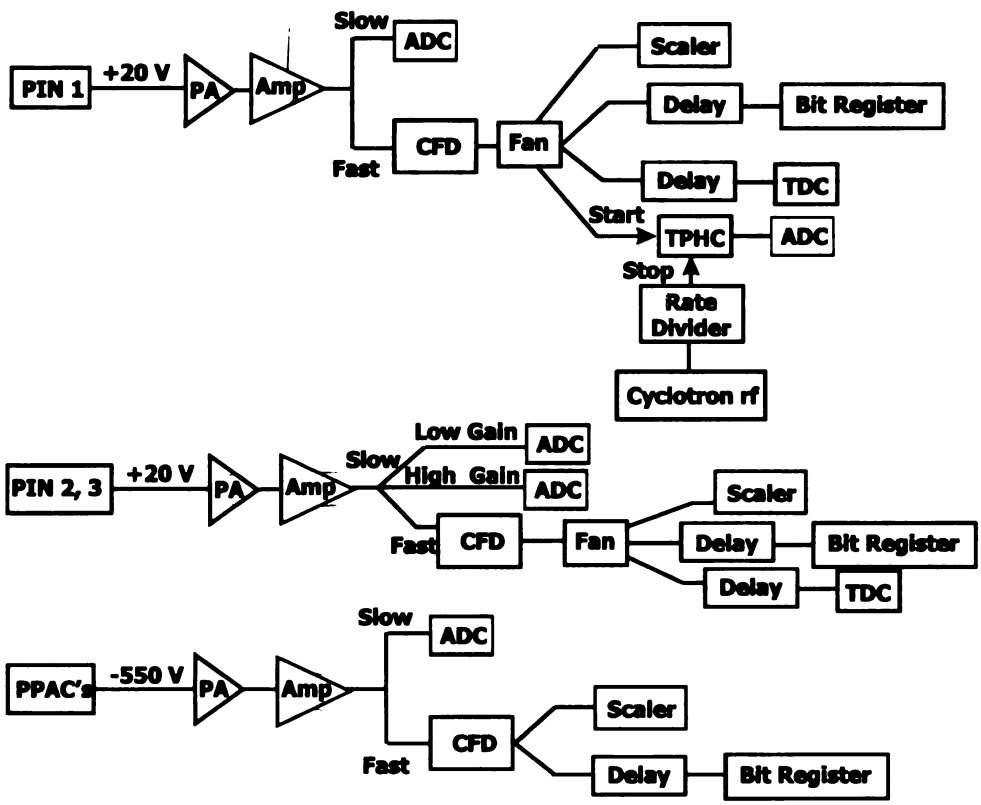

Figure 3.9: PIN and PPAC electronics diagram for experiment 98020.

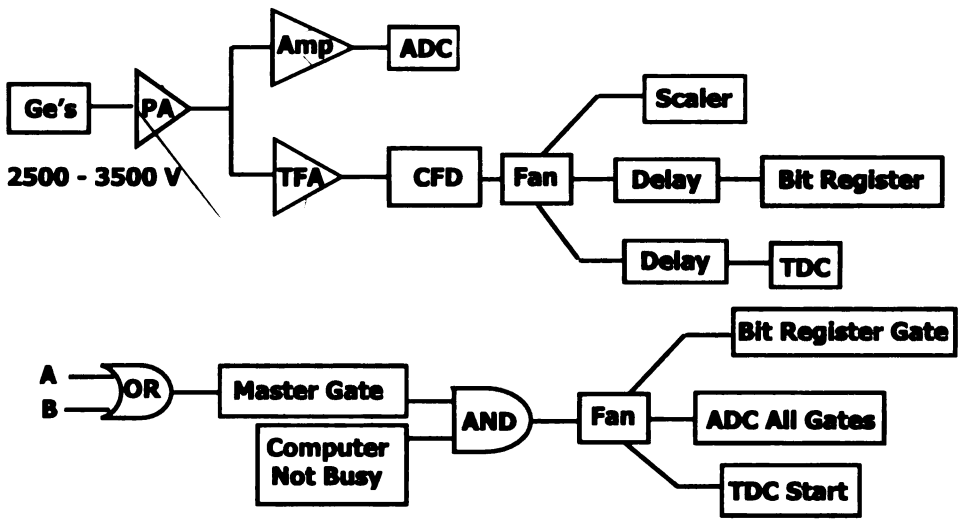

Figure 3.10: Ge and master gate electronics diagram for experiment 98020. A and B are the front and back triggers as shown in Fig. 3.8.

Chapter 4

Sample Data Analysis for Continuous Beam Implantation

The bulk activity measurement discussed in Sec. 3.2.1 made use of a Si PIN detector to identify fragment implants and plastic scintillators for beta detection. When a fragment of interest was implanted into one of the nine Al collection foils, the primary cyclotron beam was stopped for a fixed time to reduce the beam-induced background in the scintillators during the beta detection period. To study the decay properties of short-lived, low intensity radioactive beams more efficiently, a new beta counting system has been developed. As discussed in Sec. 3.2.2, this new system employs a double-sided silicon strip detector (DSSD) to correlate fragment implants with subsequent beta decays. The goal was to take advantage of the high pixelization of the strip detector to continuously implant short-lived activities over the entire active area of the detector. This results in a two-fold improvement over the conventional beta detection system. (1)Each of the pixels can be treated as individual detectors, therefore, an implant and its subsequent beta decay may be correlated within a given pixel on a nuclide-by-nuclide basis. (2)By maintaining an implantation rate of less than 100 s^{-1}, the beam may be continuously implanted into the strip detector resulting in a duty factor on the order of 100%.

4.0.3 Test study, beta decay of ^{57}V

To ensure that the DSSD beta detection system was working properly, the decay properties of a known nuclear system were compared with previously published results. The nuclide utilized for this test was ^{57}V, which represented 37.1% of the implanted cocktail beam. ^{57}V was identified based on its energy loss in the upstream Si PIN detector and time of flight from the cyclotron, see Fig. 4.1a. By placing a gate around the ^{57}V contour in the particle identification spectrum and requiring coincident events in the other detectors within the experimental setup, the decay properties of ^{57}V were extracted.

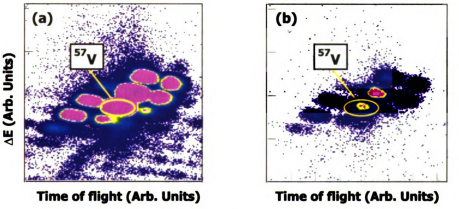

Figure 4.1: (a) Energy loss versus time of flight plot representing all nuclei implanted within the DSSD. (b) Implantation spectrum correlated with subsequent beta events.

As discussed in Sec. 3.2.2, implant events were identified in software as any event that triggered the DSSD and the first Si PIN detector, without firing the third PIN detector. The high-energy implant events were recorded as overflow events and resulted in an average implant strip multiplicity of approximately six, see Fig. 3.5. To determine the pixel of each implant, the sum of consecutive strip numbers were tallied and divided by the multiplicity for the front and back of the DSSD. The most central pixel, along with its i±1 neighbors were labelled as implant pixels. In addition, each of the implant pixels were tagged with an absolute time stamp, the corresponding energy loss of the implant in the first PIN detector and the time of flight of the implant from the cyclotron to the first PIN detector. If a second implant was identified in the

pixel within a 6 s time window before a decay, the pixel was zeroed to reduce the chance of random implant-decay correlations. A timestamp was acquired by running two 16-bit clocks in parallel. One clock was incremented 65536 channels every two seconds, clock 1, and the other was incremented one channel per second, clock 2. An algorithm was written to create a timestamp such that,

$$Timestamp = clock\ 1 + \frac{clock\ 2}{2} * 65536$$

Overall, the timestamp had a 30 μs resolution.

Ideally, a beta particle would be identified as an event that triggered the strip detector without triggering the upstream Si PIN detector. However, prior to the experimental run, the DSSD was energy calibrated with an open ^{232}U source. The source was exposed to the DSSD within close proximity while the chamber was under vacuum for an extended period of time. Alpha peaks ranging from 5 - 8 MeV were observed in the DSSD energy spectra. To determine the origin of these alpha peaks, two background measurements were performed within $\approx$ 18 hours of one another. During the first measurement an activity of 15.9 s^{-1} was calculated by taking the ratio of the number of counts observed in the alpha peaks (1.40 x 10^5) to the total run time. The measured activity during the second background run was 13.2 s^{-1}. Based on Eq. 2.1, a half-life of 2.79 d was calculated. Considering the decay chain of ^{232}U (see Fig. 4.2), this half-life is close to the known half-life of ^{224}Ra, suggesting that the DSSD was contaminated with traces of ^{224}Ra.

To isolate the DSSD triggers generated by beta particles from the α particles, beta decay events were identified in software as events that triggered both the front and the back of the strip detector and either the second or third Si PIN detector without firing the first PIN detector (see Fig. 3.4). This condition was imposed under the assumption that alpha particles would not have sufficient energy to exit the DSSD and trigger either PIN detector. By requiring additional conditions to satisfy a beta event, the overall beta efficiency of the DSSD was reduced. Table 4.1 lists the ϵ_β values determined by taking a ratio of the correlated fragment-β spectrum, Fig. 4.1b,

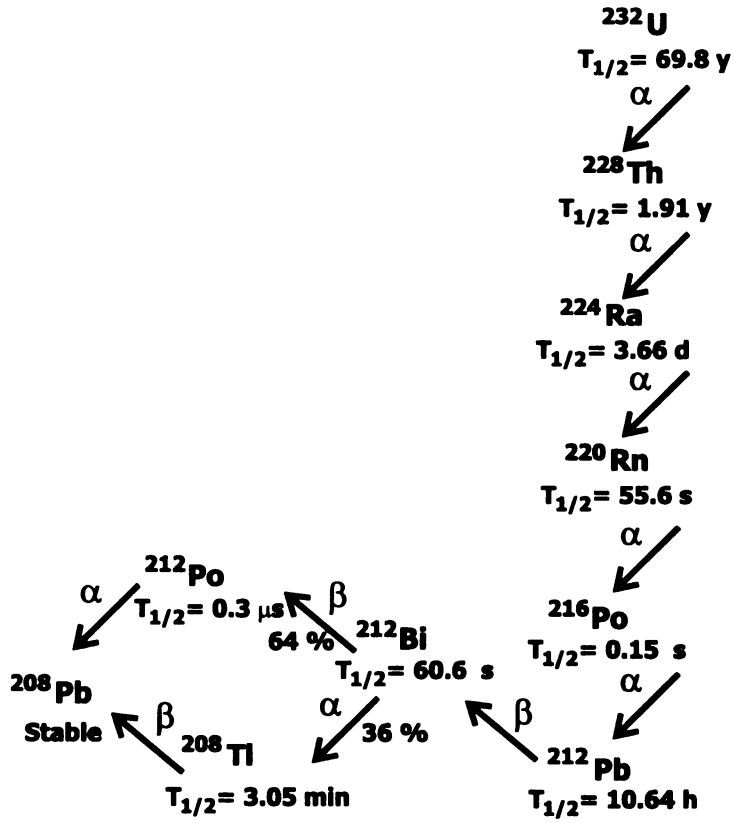

Figure 4.2: The decay scheme for ^{232}U.

to the implantation spectrum, Fig. 4.1a, on a nuclide-by-nuclide basis. The Q_β values and previously measured $T_{1/2}$ are also listed for the readers convenience, where data were taken from Ref. [9,28–30].

In an attempt to simulate the beta efficiency, a Monte Carlo based simulation program, GEANT, was utilized. To ensure that the simulation program was working properly, a ^{90}Sr source run was performed after the ^{224}Ra contamination had decayed. Thus, the master gate was triggered only by beta events above threshold within the DSSD. The efficiency calculations using this point source are detailed in Appendix A. Using a source-to-detector distance of 26.7 cm, a lower limit experimental beta efficiency of 0.291(9)% was determined. To determine the intrinsic efficiency of the detector, the calculated efficiency was divided by the geometrical efficiency of the detector, 0.175%. An intrinsic efficiency of 166.3% has been determined. The intrinsic

Table 4.1: Calculated beta efficiencies for the nuclides produced in Exp. 98020. In addition, the decay energies and previously measured $T_{1/2}$ are provided. Data were taken from Ref. [9, 28–30].

Nuclide	ϵ_β (%)	Q_β (MeV) [9]	$T_{1/2}$ (s)
^{54}Sc	1.78(8)	11.3	0.225(40) [29]
^{56}Ti	1.81(2)	7.11	0.150(30) [28], 0.190(40) [30]
^{55}Ti	1.81(5)	7.34	0.600(40) [28], 0.320(60) [30]
^{58}V	2.02(3)	11.6	0.205(20) [29], 0.200(20) [30]
^{57}V	1.85(1)	8.02	0.323(30) [29], 0.340(80) [30]
^{59}Cr	1.74(1)	7.77	0.740(240) [9]
^{58}Cr	1.94(3)	3.97	7.00(30) [9]
^{61}Mn	1.92(2)	7.18	0.710(10) [9]
^{60}Mn	1.86(3)	8.24	51.0(6.0) [9]
^{60}Mn^{m1}		8.51	1.77(2) [9]

efficiency is believed to be greater than 100% as a result of beta particles scattering off of the Al vacuum chamber and the Al degrader to which the source was mounted. The scattered particles were effectively collimated, increasing the total beta efficiency of the DSSD in the given geometry. The GEANT simulation confirmed this hypothesis. The details on this simulation are also discussed in Appendix A. From this simulation, a 135.9% intrinsic beta efficiency was determined, which is 82% of the determined experimental intrinsic efficiency.

To simulate the beta efficiency for Exp. 98020, the current FORTRAN code would need to be modified to account for the distribution of the beta source in the x-y plane within the DSSD. In addition, a distribution in implantation depth and straggling of the secondary beam should to be considered. An algorithm has been included in the GEANT code to vary the position of a beta particle in the z axis, however, at present, this routine has been commented out.

Unlike implant events, beta particles deposited a small amount of energy, $0 \leq \Delta E \leq 0.56$ MeV (considering a $Q_\beta = 10$ MeV), within the DSSD, thus a beta event could be isolated to the nearest strip. As depicted in Fig. 3.6, beta events were predominately multiplicity one events. For those events that resulted in a multiplicity greater than one, the decay was isolated to the pixel that registered the largest energy loss. Once a

decay pixel was identified, it was tagged with an absolute time stamp and correlated with a previously identified implant (i±1) within the same pixel.

Lifetime curves were generated by taking the difference between the absolute time of fragment implants and subsequent beta decays. Neighboring i±1 pixels with the same time difference were zeroed as they were set in the same implant array. The decay curve for ^{57}V, shown in Fig. 4.3a, was obtained by gating the total lifetime

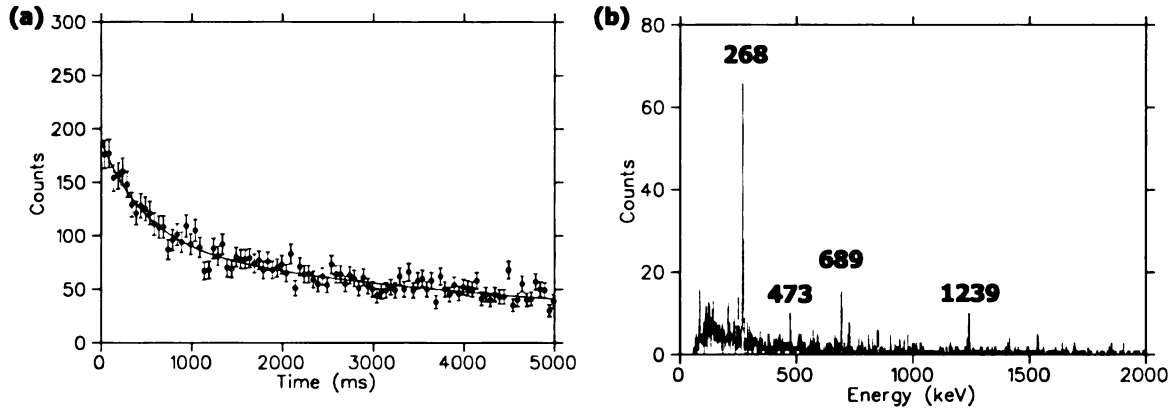

Figure 4.3: (a)The ^{57}V half-life curve following the correlation of ^{57}V implants and their subsequent beta decays. (b)Beta delayed gamma ray spectrum obtained by gating the total gamma ray spectrum on beta correlated ^{57}V implants.

spectrum on the ^{57}V contour in the correlated-ΔE versus TOF spectrum (see Fig. 4.1b). The data was fit using a two-component exponential, one component for ^{57}V and the other for the background, in PHYSICA, a mathematical analysis and data visualization software. Using the FIT command in PHYSICA, the fit parameters were varied to minimize the least-squares residual between the equation and the dependent variable [31]. From this least-squares fit, a half-life of $T^{\beta}_{1/2}$ = 358(62) ms was extracted. This half-life is consistent with the previous measurements of Sorlin *et al.* [29], $T_{1/2}$ = 323(30) ms, and Ameil *et al.* [30], $T_{1/2}$ = 340(80) ms.

A beta-delayed gamma ray spectrum was also extracted following the decay of ^{57}V. A total gamma ray spectrum was generated by adding the energy spectrum of one of the five Ge detectors (Ge 120%, Ge 80% and any of the three clover detectors) that observed a gamma trigger above threshold on an event-by-event basis. Figure 4.3b was produced by gating the total gamma ray spectrum on the same ^{57}V contour discussed

above. An intense gamma ray peak was observed at 268.1(1) keV. In addition, several small gamma ray peaks were observed at 473, 689 and 1239 keV. The smaller peaks are the result of a random background generated by the decay of the other radionuclides implanted within the DSSD. For instance, the 473 keV and 689 keV gamma rays are populated by the beta decay of ^{59}Mn and the 1239 keV gamma ray is fed by the beta decay of ^{59}Cr.

Background peaks, in addition to true β-delayed γ peaks, have been observed in the beta-delayed gamma ray spectra for the other eight implanted radionuclides. Typically, the most intense gamma ray peak(s) observed in the beta-delayed gamma ray spectrum corresponds to a true beta-delayed gamma ray transition in the nuclide of interest. Thus, the intensity of the 268 keV peak suggests that this peak is indeed the result of a β-delayed γ-ray transition in ^{57}Cr and is not a random background peak. Considering the area of this peak, the ϵ_β value listed in Table 4.1 and the ϵ_γ determined in Appendix B, a beta decay branching ratio from the ground state of ^{57}V to the 268 keV state in ^{57}Cr may be extracted. To ensure that this branching ratio is correct, a nuclide with a known branching ratio produced in this study was first analyzed.

An 18(3)% beta branch has been determined for the ground state feeding of ^{61}Mn to the 629 keV state in ^{61}Fe [32]. A β-delayed gamma ray spectrum for ^{61}Fe was produced in a similar manner as the spectrum for ^{57}Cr. 5$\pm$3 counts were observed in the 629 keV peak. Considering the beta efficiency for ^{61}Mn (see Table 4.1), the gamma efficiency (0.0605) and the total number of ^{61}Mn implants (4.93(1) x 10^5), a beta decay branch was determined as follows:

$$BR = \frac{\gamma_{counts}(629)}{\epsilon_\beta * \epsilon_\gamma \; {}^{61}Mn \; implants} = 0.874(524)\% \qquad (4.1)$$

This branching ratio is a factor of 21 smaller than the value reported by Runte *et al.* [32], suggesting that $\epsilon_\beta * \epsilon_\gamma$ is a factor of 21 too large.

During the experimental run, a number of single-sided events satisfying a beta condition were observed. These single-sided events were originally assumed to arise

Table 4.2: Comparison of the number of experimental and simulated single-sided beta events.

Event	*Experiment*	*Simulation*
Single-Sided Front	1.97 x 10^5	3.25 x 10^4
Single-Sided Back	3.80 x 10^5	7.32 x 10^4
Neither Front nor Back	1.65 x 10^3	3.37 x 10^3

from the presence of dead strips or strips with high threshold settings on one side of the DSSD. To test this theory, a FORTRAN code was written to count the number of single-sided events expected for each side of the strip detector when a given number of beta particles were emitted into the detector. The user was required to enter the central position and FWHM of the extended source each time the code was executed, and the position of the emitted beta particle was varied such that by programs end, the source had a Gaussian distribution in both the x and y plane. Events identified in strips that were not working properly or set with high energy thresholds in the experiment were not counted. Table 4.2 lists the number of single-sided events observed in the simulation and experimentally when a ^{90}Sr source run was performed. 7.69 x 10^5 beta particles were observed at an energy below $\approx$ 6 MeV in the DSSD during the source run, thus, 7.69 x 10^5 beta particles were considered in the simulation. Although the ratio of the single-sided front to single-sided back events are comparable (52% from experiment and 44% from simulation), there are clearly more single-sided events observed experimentally. The reason for this discrepancy is unknown, however, it may explain the enhancement of ϵ_β by at least a factor of 6.

A significant portion of the enhanced $\epsilon_\beta{}^*\epsilon_\gamma$ is believed to arise from improperly set gates on the ADC's processing the germanium signals. "True" beta events were identified in software as double-sided DSSD events. The number of observed beta-delayed gamma rays may have been reduced because the ADC gates may not have overlapped with the actual coincident γ-ray energy signals from the Ge amplifiers. When the gamma ray spectra were examined without requiring a software beta coincidence, there were far more gamma rays observed because the master gate was set

by any event above threshold in the strip detector. Since there was a large number of single-sided DSSD events, the gamma ray gate was almost always open, allowing one to see almost all the beta delayed gamma rays within the limits of the Ge detection efficiency. However, the later gamma ray spectra were uncorrelated.

In an attempt to extract a beta decay branch from the ground state of ^{57}V to the 268 keV state in ^{57}Cr, the ^{57}V branching ratio was normalized to the known branching ratio of ^{61}Mn,

$$BR(^{57}V) = BR(^{61}Mn)\,\frac{\gamma_{counts}(^{57}V)}{\gamma_{counts}(^{61}Mn)}\,\frac{\epsilon_\beta(^{61}Mn)}{\epsilon_\beta(^{57}V)}\,\frac{^{61}Mn\ imp.}{^{57}V\ imp.}\,\frac{\epsilon_\gamma(^{61}Mn)}{\epsilon_\gamma(^{57}V)} \qquad (4.2)$$

Using Eq. 4.2 the enhancement of $\epsilon_\beta{}^{*}\epsilon_\gamma$ may be factored out. Based on this equation, a beta branch of $36^{+22}_{-26}\%$ was determined following the beta decay of the ground state of ^{57}V to the 268 keV state in ^{57}Cr. A $\pm 22\%$ error was determined by propagating the statistical error due to the ^{57}V related terms ($\pm 1\%$) and the systematic error from the ^{61}Mn related terms ($\pm 21\%$). In addition, an upper limit -4% error was determined for a possible 1% gamma ray intensity feeding into the 268 keV state in ^{57}V from a higher-lying state. In the absence of an additional gamma ray in the beta-delayed gamma ray spectrum for ^{57}V, the intensity of such a gamma ray would be on the order of 1%. Considering this branching ratio, the extracted half-life and Eq. 2.6–2.7, a $\log ft$ range of $4.43 \leq \log ft \leq 5.35$ was determined, suggesting that the 268 keV state is populated by an allowed beta transition.

To enhance the observed γ-ray spectrum, a second beta-delayed gamma ray spectrum was obtained by accepting gamma rays observed within a 200 ms time window following the implantation of ^{57}V nuclide (see Fig. 4.4a). To correct for random background, the intensity of two non-^{57}Cr peaks in the ^{57}V-gamma spectrum, 726 keV and 1239 keV, were compared with the intensity of these peaks in the total gamma ray spectrum (shown in Fig. 4.4b). The 726 keV gamma ray is populated by the beta decay of ^{59}Mn and the 1239 keV gamma ray is populated by the decay of ^{59}Cr. The gamma ray peaks were fit to Gaussians using the Oak Ridge Display, Analysis and Manipulation Module, DAMM. A background correction factor of 0.859 was calcu-

lated by taking the average ratio of the area of the 726 keV and 1239 keV γ-ray peaks in the ^{57}V spectrum to the area of the same peaks in the total γ-ray spectrum. By multiplying the total gamma spectrum by this correction factor and subtracting the resulting spectrum from the ^{57}V-gamma spectrum, a background subtracted ^{57}Cr spectrum was obtained, see Fig. 4.4c. A single gamma-ray peak was observed at 268.1(1) keV.

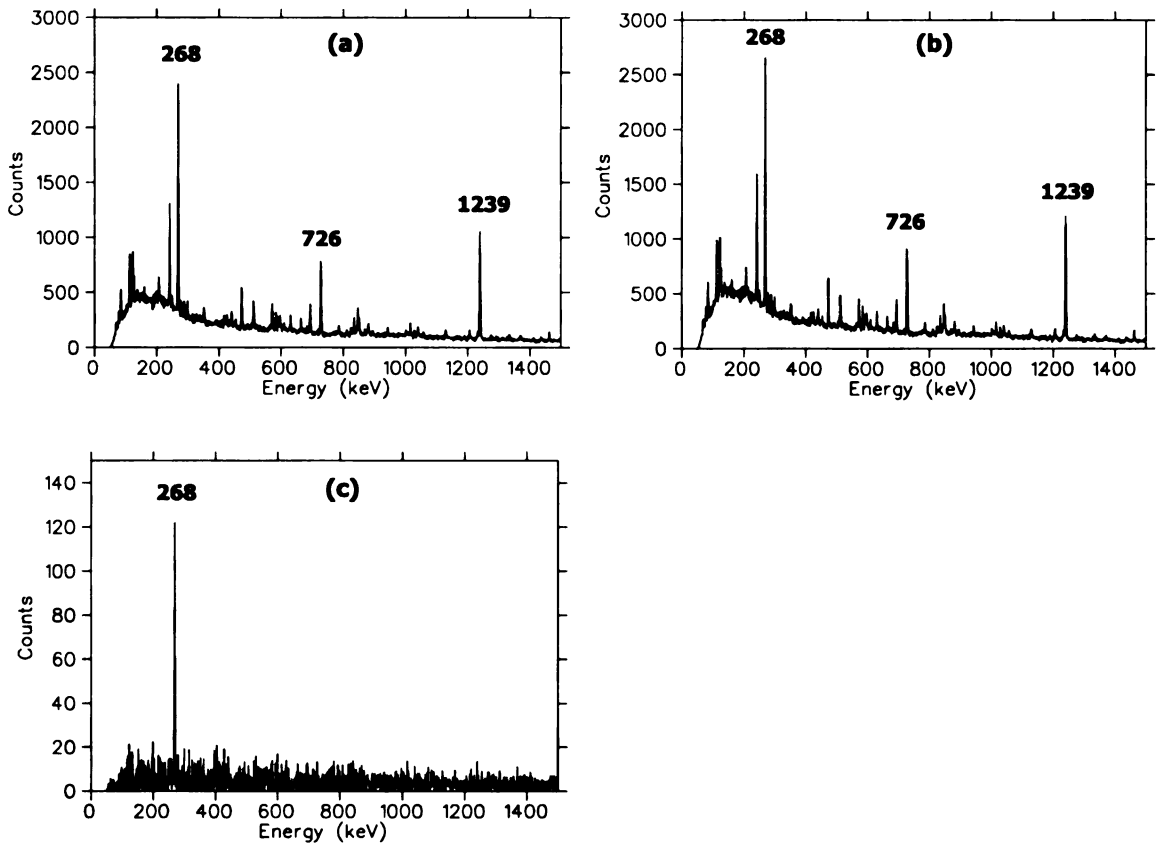

Figure 4.4: (a)The Beta-delayed gamma ray spectrum following the beta decay of ^{57}V, (b)the total gamma ray spectrum and (c)the background subtracted β-delayed gamma-ray spectrum following the decay of ^{57}V.

Figure 4.5 depicts the β-delayed gamma ray spectrum observed by Sorlin *et al.* [29] following the β-decay of ^{57}V. The spectrum was obtained using bismuth germanate (BGO) inorganic scintillator detectors, which have a higher counting efficiency but poor energy resolution as compared to HPGe detectors. The authors identified three γ-rays in Fig. 4.5 at 300(50), 700(50) and 900(50) keV. The authors also identified

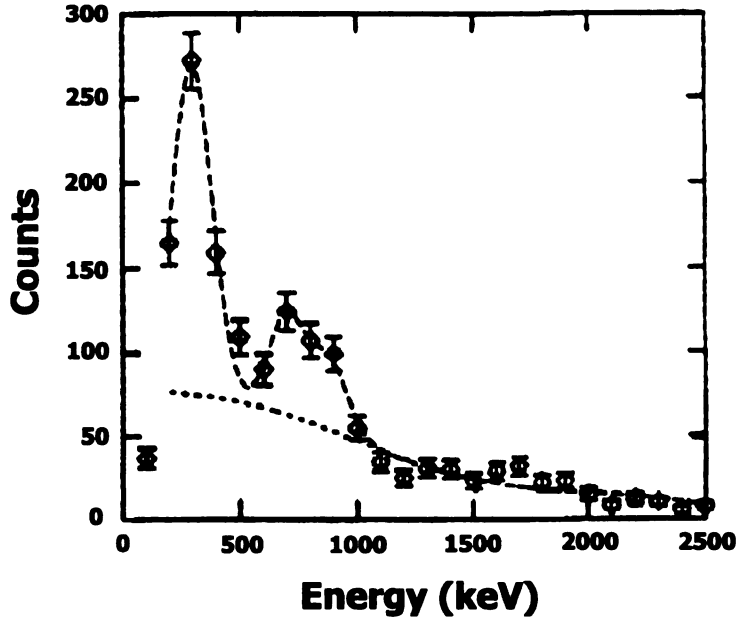

Figure 4.5: Beta-delayed gamma ray spectrum observed by Sorlin *et al.* [29] following the decay of ^{57}V.

a 267(4) keV gamma ray in their β-gated Ge spectrum, in the absence of the two higher-energy gamma rays, which is consistent with the current measurement. Sorlin *et al.* [29] extracted a 45(5)% beta branch to the 300(50) keV state following the beta decay of ^{57}V, suggesting that the beta branch to the 268 keV state is indeed the result of an allowed beta transition.

In an attempt to explore the low-energy level structure of ^{57}Cr, a 268-γ coincidence spectrum was generated. This spectrum was obtained by recording γ-ray transitions observed in one of the Ge detectors when another detected a 268 keV transition. Coincident gamma rays are observed if a transition overlaps within the resolving time of the spectrometer with the 268-keV gamma ray. The resulting 268-γ spectrum is shown in Fig. 4.6. No coincident gamma rays were observed.

4.0.4 J$^{\pi}$ discussion

^{57}V has 23 protons and 34 neutrons. In its ground state, the odd, 23rd proton resides in the 1f$_{7/2}$ single-particle orbital, suggesting a J^{π} value of $7/2^{-}$. The National Nuclear Data Center [33] has tentatively assigned the ground state spin and parity of ^{57}V

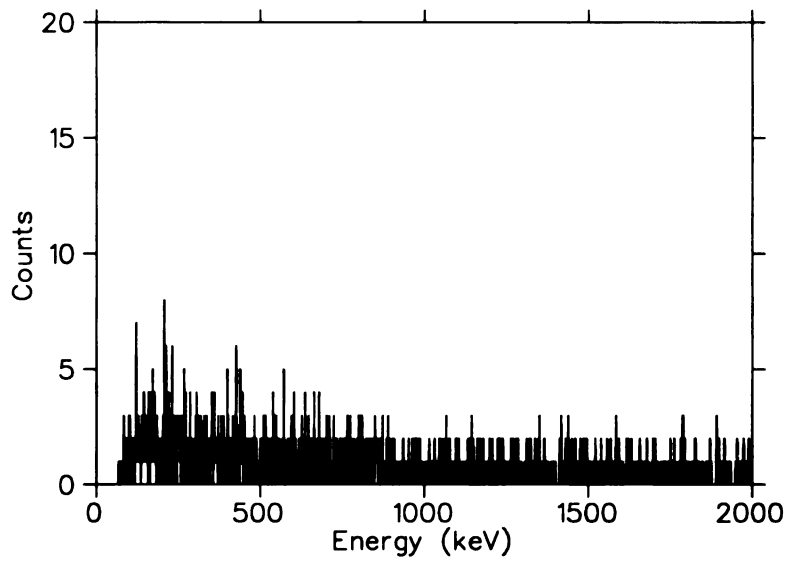

Figure 4.6: 268-γ coincidence spectrum.

as $7/2^-$ based on the systematics of the odd-A vanadium isotopes. The extracted $4.43 \leq \log ft \leq 5.35$ following the ground state beta decay of ^{57}V to the 268-keV state in ^{57}Cr suggests that this state is populated via an allowed beta transition. With this J^π assignment, allowed beta transitions would populate states in ^{57}Cr with a spin and parity of $5/2^-$, $7/2^-$ and $9/2^-$ (see Table 2.1). Thus, the spin and parity of the 268 keV state in ^{57}Cr should be $5/2^-$, $7/2^-$ or $9/2^-$.

The ground state of ^{57}Cr has been assigned a J^π ranging from $3/2^-$ to $7/2^-$ [33]. Davids *et al.* [34] have assigned this state a spin and parity of $3/2^-$, however, this J^π value was not directly measured following their ^{48}Ca(^{11}B,pn) study. The spin and parity were deduced by considering the decay scheme of ^{57}Mn. Allowed β-branches to the ground and 1835 keV states have been observed in ^{57}Mn. Both states have a J^π of $5/2^-$, thus, the possible J^π values for the ground state of ^{57}Cr are again $3/2^-$, $5/2^-$ and $7/2^-$. In addition, Davids *et al.* considered a state at 2188-keV that was assigned a spin of 1/2 by Aniol *et al.* [35]. Davids *et al.* identified a state at 2186-keV that was populated following an allowed beta branch from ^{57}Cr. For the ground state of ^{57}Cr to decay to the $5/2^-$ and $1/2^-$ states in ^{57}Mn via an allowed beta transition, the ground state of ^{57}Cr is expected to be $3/2^-$ [34]. However, this assignment relies heavily on the $1/2^{(-)}$ identity of the 2188 keV state in ^{57}Mn [35]. In the absence of

a J^{π} confirmation, the ground state spin and parity of ^{57}Cr can only be limited to $3/2^-$, $5/2^-$ or $7/2^-$. In the event that the ground state J^{π} of ^{57}Cr is either $5/2^-$ or $7/2^-$, one would expect a strong ground state to ground state beta branch from ^{57}V to ^{57}Cr.

4.0.5 Summary

The decay properties of ^{57}Cr have been examined following its production via the beta decay of ^{57}V. The goal of this study was to compare experimentally extracted properties with the previously published results to ensure that the new DSSD beta detection system was working properly. Utilizing this new beta detection system, a beta decay half-life of 358(62) ms was extracted, which compares well with Sorlin *et al.* [29] and Ameil *et al.* [30] measurements. In addition, a beta-delayed gamma ray was observed at 268.1(1) keV, which is consistent with the 267 keV peak observed in the β-gated Ge spectrum of Sorlin *et al.* [29]. A 36^{+22}_{-26}% branching ratio to the 268 keV state in ^{57}Cr was determined through a normalization to the ^{61}Mn-628 keV beta branch. A range of $\log ft$ values of $4.43 \leq \log ft \leq 5.35$ was determined, suggesting the beta decay of the ground state of ^{57}V to the 268 keV state in ^{57}Cr is the result of an allowed beta transition. Based on the systematics of odd-A vanadium isotopes, the ground state spin and parity of ^{57}V is expected to be $7/2^-$, suggesting the J^{π} of the observed 268 keV state in ^{57}Cr is $5/2^-$, $7/2^-$ or $9/2^-$. An allowed β-branch to the ground state of ^{57}Cr may also be possible if its spin and parity is $5/2^-$ or $7/2^-$.

Chapter 5

Experimental Results & Interpretation

5.1 Subshell Gaps and Neutron-Rich Nuclei

To predict the decay properties of nuclei away from stability, an understanding of nuclear structure is essential. To date, most of the information regarding the structure of extremely neutron-rich nuclides has been attained through the extrapolation of experimentally derived measurements of stable nuclei. However, if the magic numbers weaken or subshell closures (minor shell gaps) develop away from stability, this will have a profound impact on such predictions.

For this study, the existence of the $N = 40$ subshell was investigated by examining the properties of $^{69}_{28}Ni_{41}$ and its beta decay daughter, $^{69}_{29}Cu_{40}$. If $N = 40$ is a good subshell closure, then the low energy level structure of ^{69}Ni and ^{69}Cu may be described as a neutron and a proton, respectively, coupled to the excited states in the underlying even-even ^{68}Ni core. In addition, it was of interest to extend the study of $N = 40$ to lighter mass systems. If $N = 40$ is indeed a good subshell closure, then collectivity should be maximum at midshell. However, following the beta decay study of ^{58}V, new empirical evidence for an $N = 32$ subshell was observed. Comparing the first excited 2^+ state of $^{54}_{24}Cr_{30}$ and the new measurement for $^{58}_{24}Cr_{34}$, a clear rise in $E(2^+_1)$ was observed for $^{56}_{24}Cr_{32}$ relative to its N $\pm$ 2 neighbors. This peak in $E(2^+_1)$ for ^{56}Cr suggests the existence of a significant subshell gap at $N = 32$.

5.1.1 Neutron-Rich Nickel Near $N = 40$

One region that has attracted a good deal of attention are nuclei within the vicinity of $N = 40$. Broda *et al.* [1] suggested the existence of a subshell closure at $N = 40$, $Z = 28$ finding that the first excited 2^+ state in ^{68}Ni lies at an energy of 2.033 MeV. As compared to the $E(2_1^+)$ values of its even-even neighbors, see Fig. 5.1a, a peak in the first excited 2^+ state energy is observed for ^{68}Ni. This peak in $E(2_1^+)$ is believed to be an indication of a significant subshell closure at $N = 40$.

Further support for an $N = 40$ subshell can be found in the recently measured first excited 4^+ state of ^{68}Ni. Ishii *et al.* [37] observed the 4_1^+ state of ^{68}Ni at an energy of 3147 keV. The ratio of the first excited 4^+ state to the first excited 2^+ state is approximately 1.5, suggesting this nucleus is spherical in nature (see Sec. 1.4.2). Figure 5.1b depicts the $E(4_1^+)/E(2_1^+)$ ratios for nickel isotopes ranging from $N = 28 - 42$. As neutrons are added to the ^{56}Ni core, this ratio begins to increase, suggesting that collective interactions ensue. In the middle of the $N = 28 - 40$ subshell, the $E(4_1^+)/E(2_1^+)$ ratio is maximum at ≈ 2, indicating that midshell nuclei are vibrationally deformed. However, by ^{68}Ni, the $E(4_1^+)/E(2_1^+)$ ratio has decreased and is shell model in character.

Raman *et al.* [36] have recently reported the reduced transition probability, $B(E2)$, for ^{68}Ni as 260(60) e^2fm^4. This value was provided by D. Guillemaud-Mueller and O. Sorlin in a private communication. The reduced transition probability is another experimental probe that may be used to determine the extent of quadrupole collectivity associated with a given nuclei. The reduced transition probability is related to quadrupole deformation as follows,

$$\beta_2 = \frac{4\pi}{3ZeR_o^2}\sqrt{B(E2; 0_1^+ \rightarrow 2_1^+)} \tag{5.1}$$

where Ze is the charge of the nucleus of interest and $R_o \approx 1.25$ fm $A^{1/3}$. This equation suggests a small degree of quadrupole deformation ($\beta_2 \approx 0.1$) for ^{68}Ni. As compared with the $B(E2)$ values of other nickel isotopes in this region (see Fig. 5.1c) a reduction in quadrupole deformation is observed for ^{56}Ni and ^{68}Ni.

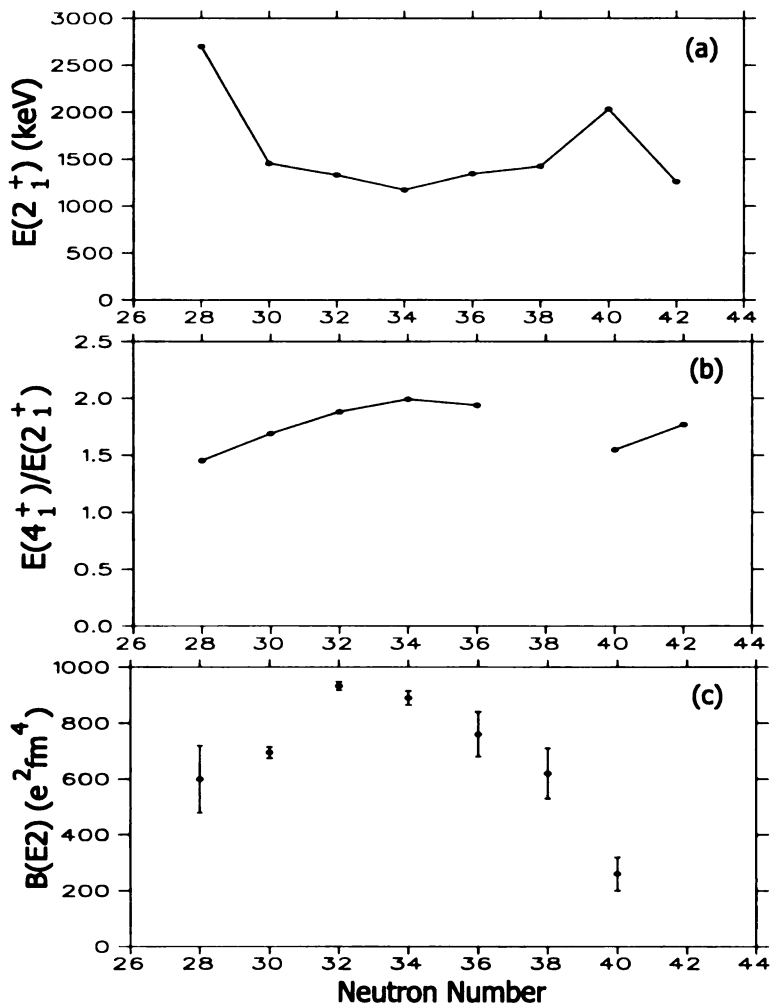

Figure 5.1: (a)The first excited 2^+ energies, (b)$E(4_1^+)/E(2_1^+)$ and (c)the reduced transition probabilities for nickel isotopes in the region $28 \leq N \leq 40$ [1,9,16,36,37].

Magicity was also suggested for ^{68}Ni by Bernas *et al.* [38] following their spin assignment of 0^+ to the first excited state of $^{68}_{28}Ni_{40}$. This J^π assignment was made following an angular distribution measurement around 0^o for the ^{70}Zn(^{14}C,^{16}O) reaction. The authors based their hypothesis on the inversion of the 2_1^+ and 0_2^+ states, which has also been observed in $^{16}_{8}O_8$, $^{40}_{20}Ca_{20}$, $^{72}_{32}Ge_{40}$, $^{90}_{40}Zr_{50}$, $^{90}_{40}Zr_{56}$ and $^{98}_{42}Mo_{56}$ [39]. The lowering of the 0_2^+ state below the 2_1^+ state in ^{68}Ni has been attributed to a two-particle excitation to the $\nu 1g_{9/2}$ orbital, resulting in a strong two-neutron coupling in this shell [38]. However, based on the 2_1^+ and 0_2^+ spin inversion argument, their suggestion of magicity for ^{68}Ni was premature at best.

The collective dynamics of ^{68}Ni have been investigated by calculating its potential energy as a function of quadrupole deformation based on Hartree-Fock-Bogoliubov theory [39]. Two minima have been predicted, an absolute minimum at $E = 0$ MeV with $\beta \approx 0$, and a local minimum at $E \approx 3$ MeV with $\beta \approx 0.4$. The absolute minimum suggests that the ground state of ^{68}Ni is spherical, whereas the local minimum is indicative of a deformed 0_2^+ state.

For this study, the existence of an $N = 40$ subshell was investigated by examining the properties of $^{69}_{28}Ni_{41}$ and its beta decay daughter, $^{69}_{29}Cu_{40}$. If $N = 40$ is indeed a good subshell closure then the excitations in the A - 1 and A + 1 nuclei should consist of single-hole or -particle states coupled to excited states in the underlying even-even ^{68}Ni core [40]. In light of this argument, the low-energy structure of ^{69}Cu will be discussed.

Recently, several new microsecond isomeric states have been identified in the neutron-rich nuclides near ^{68}Ni, including a 0.439(3) μs state at 2.70 MeV in ^{69}Ni [41]. The depopulation of this isomeric state in ^{69}Ni follows mainly a three γ-ray cascade to the ground state (see Fig. 5.2a). Two weak γ-ray cascades were also observed from this isomer, one terminating at a previously unidentified level at 321 keV in ^{69}Ni. The authors proposed the 321-keV state as a second isomer in ^{69}Ni with $J^\pi = 1/2^-$ (based on an assumed spin-parity of $J^\pi = 17/2^-$ for the 2.70 MeV isomeric state and a cascade of four stretched $E2$ transitions). They estimated a half-life, based on the

Weisskopf estimate, of $\approx$ 14 days for an $M4$ transition from the proposed 321-keV isomeric state to the $9/2^+$ ground state of ^{69}Ni. The more probable decay path for this isomeric state, as pointed out in Ref. [41], is β decay to the $J^\pi = 3/2^-$ ground state of ^{69}Cu. Assuming a log ft value similar to that observed for the decay of the $J^\pi = 1/2^-$ ground state of ^{67}Ni to the $J^\pi = 3/2^-$ ground state of ^{67}Cu (log ft = 4.7 [32]), a β decay half-life of $\approx$ 3 s was predicted [41].

Mueller *et al.* [42] studied the β decay of ^{69}Co and its subsequent daughters. The parent nuclei were produced by proton induced fission of ^{238}U, and the Ion Guide Laser Ion Source [43] at the Leuven Isotope Separator On-Line was used to selectively ionize and efficiently extract the Co isotopes from the production target. They observed a 594-keV β-delayed γ-ray transition, which they attributed to the decay of ^{69}Co, and a 1298-keV transition assigned as a β-delayed γ ray following the decay of a 3.5(5) s isomeric state in ^{69}Ni. This beta-delayed gamma ray was previously identified at 1296 keV [44]. The proposed sequence for the ^{69}Co β decay is shown in Fig. 5.2b, along with the states observed following the decay of the 0.439 μs isomer in ^{69}Ni.

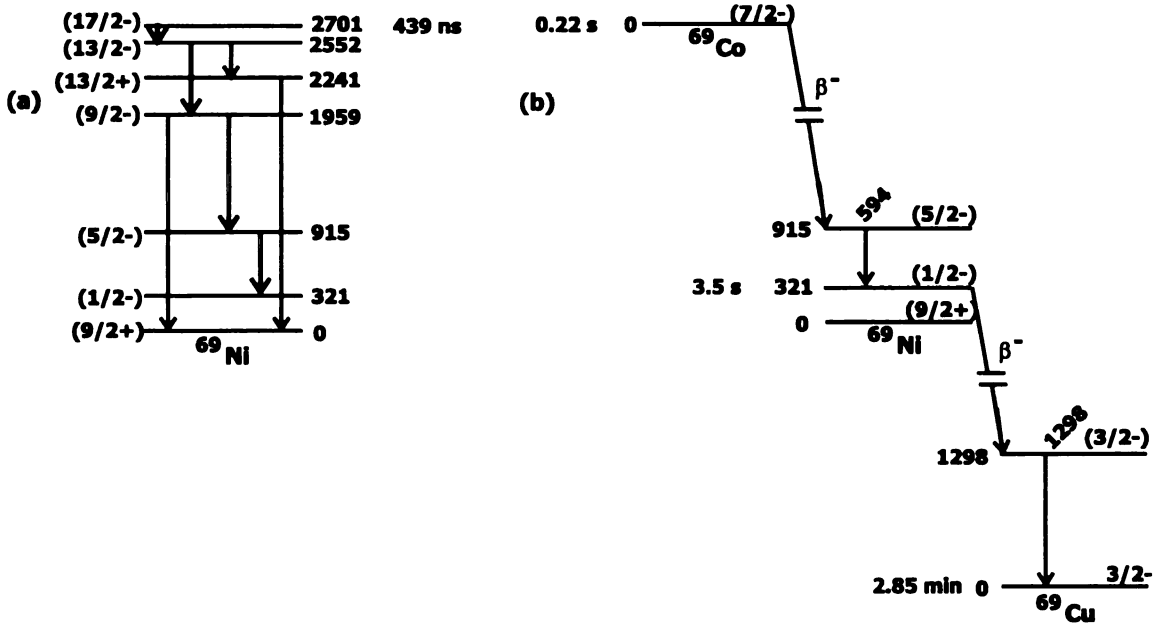

Figure 5.2: (a) The ^{69}Ni levels identified by Grzywacz *et al.* [41] and (b) the ^{69}Co - ^{69}Ni β decay sequence proposed by Mueller *et al.* [42]

The recent improvement in the intensities of metal primary beams at the National Superconducting Cyclotron Laboratory (NSCL) at Michigan State University has allowed access to new regions of the chart of the nuclides for nuclear structure measurements. For example, the production of the 3.4(7) s isomeric state in ^{69}Ni via projectile fragmentation was detailed in Section 3.2.1.

A portion of the β-delayed γ-spectrum collected when the A1200 was set for the peak production of ^{69}Ni from ^{76}Ge is shown in Fig. 5.3a. The rotating collection wheel setup described in Sec. 3.2.1 was used for this measurement. All major transitions in the β-delayed γ spectrum could be attributed to known γ rays from the decay of ^{69}Ni or from the decays of ^{67}Co, ^{68}Ni, ^{70,71}Cu, and ^{72}Zn (the major beam contaminants) except for a peak at 1297-keV. To investigate the origins of this beta-delayed gamma ray, the corresponding beta decay half-life was extracted. The half-life curve was generated by gating a 16-bit clock in software with coincident beta particles observed in either of the two plastic scintillators incorporated within the setup (see Sec. 3.2.1) and 1297-keV gamma rays observed in the Ge detectors. The half-life curve for the 1297-keV transition is shown as an inset in Fig. 5.3a. The decay portion of the half-life curve was fit using PHYSICA with an exponential plus a constant background, and revealed a half-life of $\approx$ 4 s, inconsistent with the known half-lives of the six constituents of the beam. For comparison, the half-life curve for the 1297-keV transition is shown in Fig. 5.4 along with the half-life curves for the major γ-ray transitions from four of the six radioactive nuclides comprising the secondary beams. In addition, the full-width at half-maximum (FWHM) of the 1297-keV peak in the β-gated γ-ray spectrum was found to be $\approx$ 50% larger when compared to the FWHM of other peaks in this energy region, suggesting this peak is a doublet.

To investigate the origin of the components of the 1297-keV doublet, the tune of the A1200 fragment analyzer was changed to implant a different subset of nuclei from the ^{76}Ge fragmentation reaction. This second tune was set for the peak production of ^{71}Cu. In addition to this isotope, the secondary beam contained the radioactive nuclides ^{68}Co, ^{69,70}Ni, ^{72}Cu, and ^{73}Zn. A portion of the β-delayed γ-spectrum for

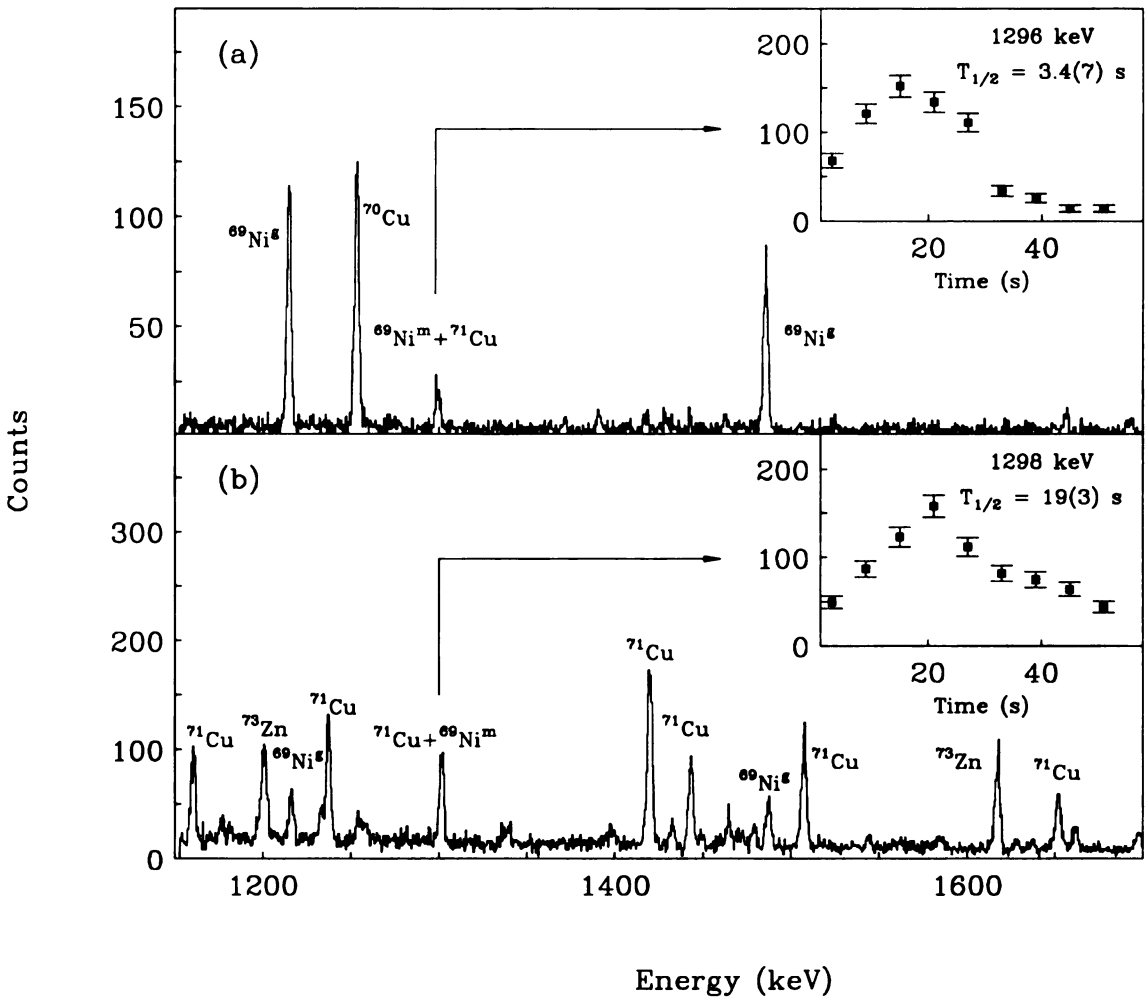

Figure 5.3: β-delayed γ-ray spectrum obtained when the A1200 separator was tuned for peak production of (a) ^{69}Ni and (b) ^{71}Cu. Known γ-ray transitions are labeled. The half-life curve shown as an inset in each spectrum corresponds to the 1297-keV doublet.

the A1200 tune set for peak production of ^{71}Cu is shown in Fig. 5.3b. A 1297-keV doublet peak was also present in this β-delayed γ-spectrum; however, the relative ratio of the two components of the doublet have changed significantly (see Fig. 5.6). The half-life curve obtained for the 1297-keV transition during the second tune of the A1200 is shown as an inset in Fig. 5.3b. A single component fit (exponential plus background) to this half-life curve revealed a half-life of $\approx$ 19 s, consistent with the adopted half-life of ^{71}Cu ($T_{1/2}$ = 19.5 s). In addition, the 1298.1(4) keV transition, not previously assigned to the β decay of ^{71}Cu, is observed to be coincident with the known 489-keV transition in ^{71}Zn (see Fig. 5.5). Based on the half-life measurement

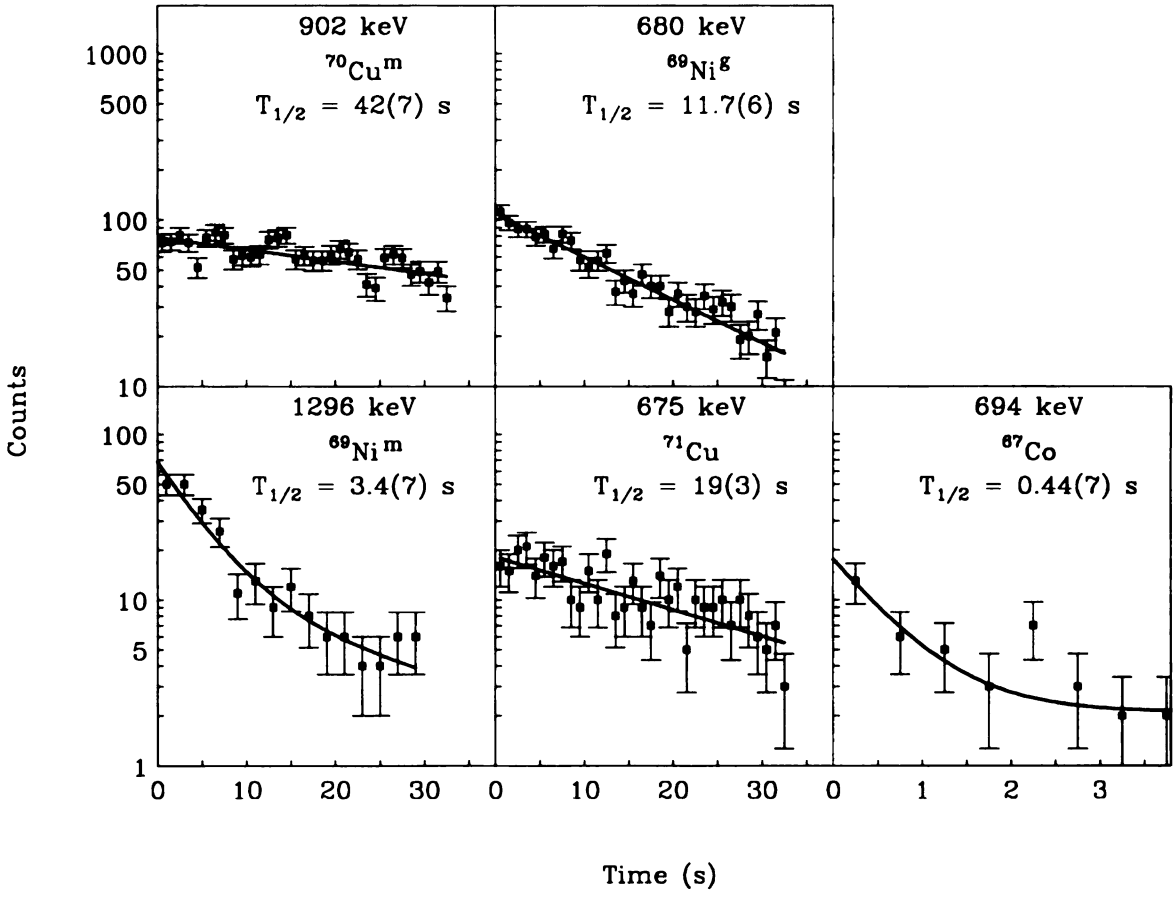

Figure 5.4: Decay time curves for selected γ-ray transitions identified during implantation of ^{67}Co, ^{68,69}Ni, ^{70,71}Cu, ^{72}Zn. The two nuclides denoted with a superscript of 'm' represent metastable/isomeric forms of the indicated nuclide [45].

and γ-γ coincidence data, the higher-energy member of the 1297-keV doublet was assigned to the decay of ^{71}Cu.

The decay portion of the half-life curve for the 1297-keV doublet obtained during the first tune of the A1200 (Fig. 5.4) was fit taking into account a contribution from the 1298-keV transition now assigned to the β decay of ^{71}Cu ($T_{1/2}$ = 19.5 s). A two-component fit,

$$\begin{aligned} y(T) &= A(^{69}Ni) * exp(-0.693 * T/T_{1/2}) \\ &\quad + A(^{71}Cu) * exp(-0.693 * T/19.5\ s) \end{aligned} \tag{5.2}$$

where $T_{1/2}$ is the half-life of the beta-decaying isomer and $A(^{69}Ni)$, $A(^{71}Cu)$ are the corresponding activities of ^{69}Ni and ^{71}Cu at the beginning of the beam off cycle,

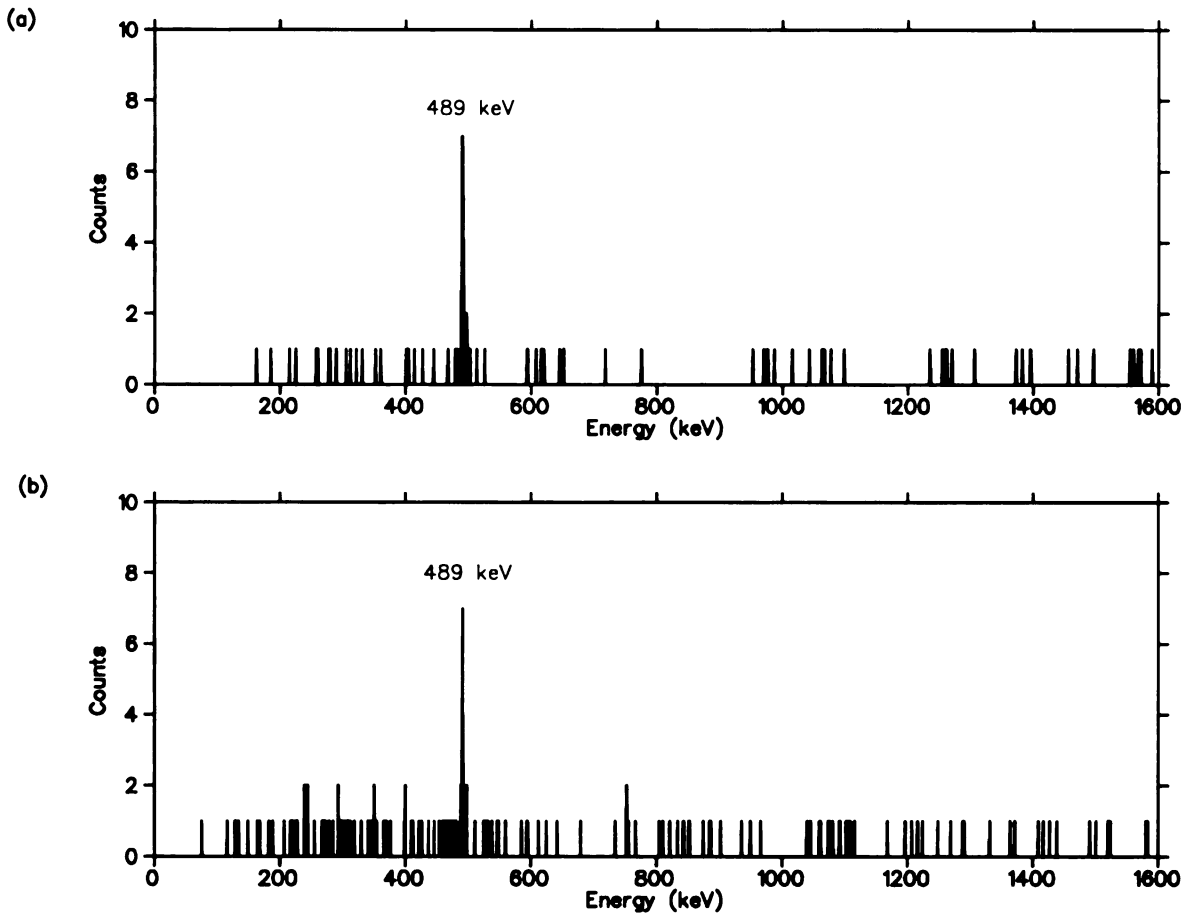

Figure 5.5: 1298-γ coincidence spectra for the (a) 80 and (b) 120% Ge detectors. The newly identified 1298-keV transition is observed in coincidence with the known 489-keV transition in ^{71}Zn.

resulted in a deduced half-life of 3.4(7) s for the low-energy member of the 1297-keV doublet. The short half-life of this 1296.1(2)-keV γ-ray cannot be attributed to the ground state decay of any species implanted when the A1200 was tuned for peak production of ^{69}Ni. Although the half-life for the 1296-keV transition is only slightly outside the 1σ value of the measured half-life for ^{70}Cu^{g}, the β decay of this nucleus is known [9] to feed only the ground and first excited (885 keV) states of ^{70}Zn. There was no evidence of a 1296-885 coincidence in the γ-γ data, and the relative peak intensities of these transitions would imply a direct β feeding of $> 10\%$ if the 1296-keV transition directly populated the ground state of ^{70}Zn.

Since the 1296-keV transition was observed in the β-delayed γ-ray spectra for both A1200 tunes, it may be attributed to a β-decaying isomer in either ^{69}Ni or ^{71}Cu,

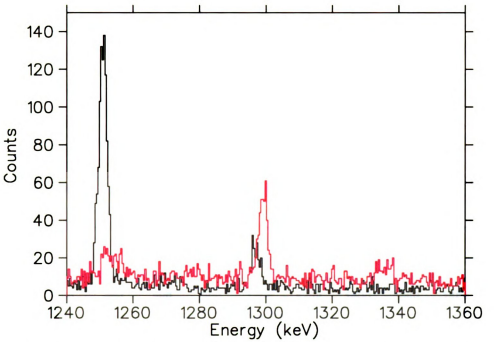

Figure 5.6: A portion of the β-delayed gamma ray spectrum when the A1200 was tuned for the peak production of ^{69}Ni (black line) and the peak production of ^{71}Cu (red line).

which were the only two nuclei present in both radioactive beam implantations. From the difference in the production intensities of ^{69}Ni and ^{71}Cu and the change in the 1296-1298 γ-ray intensities (see Fig. 5.6), the 1296-keV activity is correlated with the production of ^{69}Ni. This suggests that the 1296-keV β-delayed γ-ray transition originates from a 3.4(7) s isomer in ^{69}Ni. This transition is consistent with Mueller *et al.* [42], see Fig. 5.2b.

To determine if other gamma ray transitions having a similar half-life to the 1296 transition were present, the gamma ray intensities during the beam on and beam off cycles were examined. By taking the ratio of the beam on to beam off intensity, a comparison of the half-lives of the beta-delayed gamma ray transitions observed in the Ge detectors were made. Nuclides with short β-decay half-lives would result in a larger beam on/off ratio relative to longer-lived species. Figure 5.7 depicts the ratio of the on/off intensities for the main β-delayed gamma ray transitions. These data was generated by examining the β-delayed γ-ray spectra gated on the beam-on and beam-off cycles. The gamma ray peaks were fit to Gaussians and their areas were

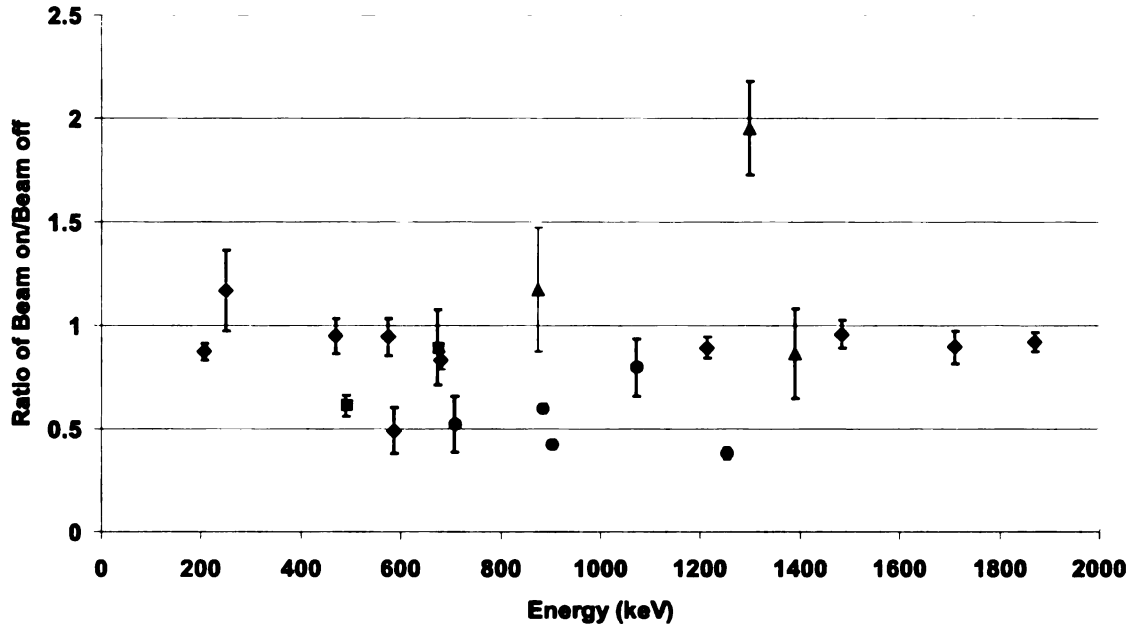

Figure 5.7: The ratio of gamma ray intensities during beam on and beam off cycles as a function of energy. The green diamonds correspond to gamma ray transitions following the beta decay of ^{69}Ni, the pink squares ^{71}Cu, the blue circles ^{70}Cu and the black triangles correspond to transitions of unknown origin. Note that no other transition is observed with an equivalent half-life to the 1296 keV gamma-ray.

extracted using DAMM. No evidence for other transitions having a similar half-life to the 1296-keV gamma ray were observed. This implies that the 1296-keV state in ^{69}Cu is the only excited state significantly populated following the beta decay of ^{69}Ni^{m1}.

Branching ratios following the beta decay of the $1/2^-$ isomer in ^{69}Ni to the 1296-keV and the ground state of ^{69}Cu were extracted. To perform this measurement, it was necessary to calculate the total number of ^{69}Ni nuclides implanted within the collection foil. A particle identification spectrum taken when the fragment analyzer was set for the peak production of ^{69}Ni is shown in Fig. 5.8a. Yellow ovals have been drawn around each of the radionuclides implanted within the collection foil. Assuming the counting efficiency of the upstream Si PIN detector (see Sec. 3.2.1) was ≈ 1, a one-to-one correlation could be made between the total number of ^{69}Ni observed in the Si PIN detector and the number of ^{69}Ni nuclides implanted within the collection foil. As one may note, however, there is an overlap between the ^{67}Co and ^{69}Ni nuclides

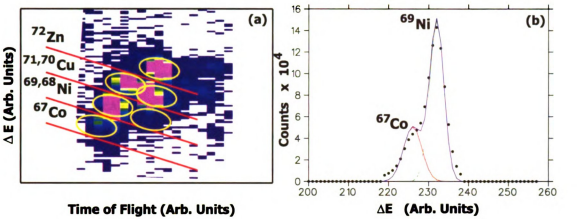

Figure 5.8: (a)Si PIN energy-loss as a function of time of flight. This particle identification spectrum was taken when the A1200 was set for the peak production of ^{69}Ni. The yellow ovals have been drawn around the individual radionuclides implanted within the collection foil. (b)Energy-loss in the Si PIN detector gated on the ^{69}Ni implants. The black circles represent the data, the red line is the fit to ^{67}Co, the green line is the fit to ^{69}Ni and the blue line is the summed Gaussian fits.

(see Fig. 5.8a).

To determine the total number of ^{69}Ni implants, a gate was drawn around ^{69}Ni in the PIN ΔE versus radiofrequency spectrum and projected onto the PIN energy loss spectrum. As shown in Fig. 5.8b, this condition produced a doublet peak in the PIN ΔE spectrum, consisting of a ^{67}Co and ^{69}Ni component. To resolve the ^{69}Ni peak, this doublet was fit with two Gaussian curves. The individual and summed Gaussians are shown in Fig. 5.8b. From the Gaussian fit, a total number of 7.23(26) x 10^5 ^{69}Ni implants were identified. Assuming that for each ^{69}Ni isotope implanted there is a corresponding beta decay, 2.89(18) x 10^5 beta particles should be observed, based on a 40(2)% β efficiency. Details on the beta efficiency calculation are provided in Appendix A. To determine the number of beta particles emitted following the decay of the $1/2^-$ isomeric state, it was first necessary to determine the total beta particles emitted from the ground state decay of ^{69}Ni, as

$$N_\beta(^{69}Ni) \;=\; N_\beta(g.s.) \;+\; N_\beta(1/2^-) \tag{5.3}$$

This was accomplished by applying a Gaussian fit to the 1871-keV gamma ray of ^{69}Cu, a known β-delayed gamma ray transition originating from the ground state of

^{69}Ni. Factoring in the beta efficiency, the gamma ray peak efficiency, 1.29%, and the relative gamma ray intensity, 0.41 [9], the total beta's attributed to the ground state decay of ^{69}Ni was determined to be 2.69(8) x 10^5. A description of the gamma-ray peak efficiency calculations are provided in Appendix B.

Based on Eq. 5.3, the total number of betas emitted following the decay of the $1/2^-$ isomeric state is 2.07(194) x 10^4. This consists of the number of beta's decaying to the $3/2_2^-$ 1296-keV excited state and the $3/2_1^-$ ground state of ^{69}Cu (see Fig. 5.2). A total of 2.54(31) x 10^4 beta particles were calculated to feed the $3/2_2^-$ state in ^{69}Cu. This value was deduced by considering the intensity of the 1296-keV transition in the β-delayed gamma ray spectrum, 3.73(46) x 10^2, corrected for the 1296 peak efficiency, 1.47%. Based on the errors of this calculation, an upper limit of 36% was extracted for the β-branch of the ^{69}Ni $1/2^-$ isomer proceeding to the ground state of ^{69}Cu. Considering the measured half-life, the beta branches and Eq. 2.7, the partial half-lives for the beta decay to the $3/2_1^-$ and $3/2_2^-$ states in ^{69}Cu were determined to be 9.44 s (lower limit) and 5.31 s (upper limit), respectively. In addition, taking Eq. 2.6 into account, where Q_β was taken from Ref. [9], log ft values of 4.54 (upper limit) and 5.23 (lower limit) to the $3/2_2^-$ and $3/2_1^-$ states in ^{69}Cu, respectively, have been deduced.

5.1.1.1 Configuration mixing in ^{69}Cu

From the experimental data for ^{69}Ni^{m1} decay, we can conclude that the β decay of the $1/2^-$ isomer in ^{69}Ni mainly proceeds through the excited $3/2^-$ state at 1296 keV in ^{69}Cu. No other excited state in ^{69}Cu has been observed in the isomer β decay, neither in the present study nor in the data of Mueller *et al.* [42]. The allowed character of the Gamow-Teller transition from the $1/2^-$ isomer in ^{69}Ni to the excited $3/2^-$ in ^{69}Cu can be understood schematically assuming the pure configurations indicated in Fig. 5.9. Taking the ground state of ^{68}Ni as the reference state, the initial $1/2^-$ configuration in ^{69}Ni can be written as:

$$\left|1/2^-\right\rangle = \left|\nu 2p_{1/2}^{-1}\left(\nu 1g_{9/2}^2\right)_{0^+}\right\rangle \tag{5.4}$$

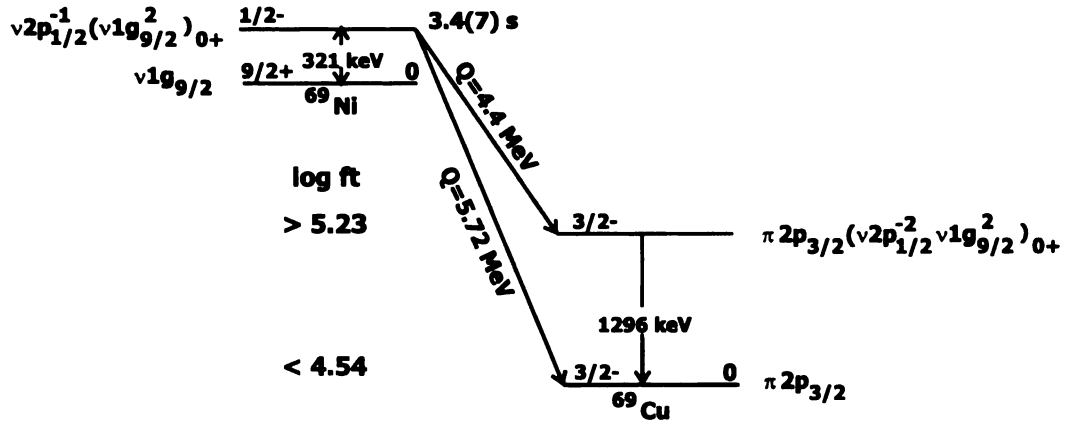

Figure 5.9: Schematic of the β decay of ^{69}Ni depicting the configurations discussed in the text [45].

and the final $3/2^-$ configurations in ^{69}Cu are:

$$\left|3/2_2^-\right\rangle = \left|\pi 2p_{3/2}\left(\nu 2p_{1/2}^{-2}\,\nu 1g_{9/2}^2\right)_{0^+}\right\rangle \tag{5.5}$$

$$\text{and} \quad \left|3/2_{\text{g.s.}}^-\right\rangle = \left|\pi 2p_{3/2}\right\rangle. \tag{5.6}$$

We can rewrite the configurations given in Eqs. 5.4–5.6 describing all the excitations in terms of particles instead of particles and holes. This reduces to using the ground state of ^{66}Ni as a reference state. The expressions become:

$$\left|1/2^-\right\rangle = \left|\nu 2p_{1/2}\left(\nu 1g_{9/2}^2\right)_{0^+}\right\rangle \tag{5.7}$$

for the $1/2^-$ state in ^{69}Ni and

$$\left|3/2_2^-\right\rangle = \left|\pi 2p_{3/2}\left(\nu 1g_{9/2}^2\right)_{0^+}\right\rangle \tag{5.8}$$

$$\text{and} \quad \left|3/2_{\text{g.s.}}^-\right\rangle = \left|\pi 2p_{3/2}\left(\nu 2p_{1/2}^2\right)_{0^+}\right\rangle \tag{5.9}$$

for the excited $3/2^-$ state and the ground state of the daughter nucleus ^{69}Cu.

It is a good approximation to assume that the pair of $1g_{9/2}$ neutrons, present in the wave function of the parent $1/2^-$ state, plays no role in the β decay process. The matrix elements for the Gamow-Teller decay then reduce to

$$\left\langle 3/2_2^- ||T(GT)||1/2^-\right\rangle = \left\langle \pi 2p_{3/2}||T(GT)||\nu 2p_{1/2}\right\rangle \tag{5.10}$$

$$\left\langle 3/2_{\text{g.s.}}^- ||T(GT)||1/2^-\right\rangle \simeq 0. \tag{5.11}$$

Therefore, assuming the wave functions of the parent and daughter states can be described by pure configurations, the β decay of the $1/2^-$ isomer of ^{69}Ni should proceed only to the excited $3/2^-$ state at 1296 keV in ^{69}Cu. Some configuration mixing, resulting in a fragment of the $\pi 2p_{3/2} \otimes \nu(1g_{9/2}^2 2p_{1/2}^{-2})$ configuration in the ground state of ^{69}Cu, can produce branching to the ground state from the decay of ^{69}Ni^{m1}.

The upper limit of 4.54 for the log ft value for the decay of the $1/2^-$ isomer in ^{69}Ni to the $3/2_2^-$ state in ^{69}Cu compares rather well with the value log $ft \simeq 4.7$ obtained for the decay of ^{67}Ni $1/2^-$ ground state ($T_{1/2} = 21(1)$ s) to the $3/2^-$ ground state of ^{67}Cu [32]. This agreement is only qualitative, since the variation of the reduced transition probability B(GT) is roughly a factor of 1.7 for the log $ft-$values quoted above. The configuration mixing in the $1/2^-$ and $3/2^-$ states connected by the GT transition seems to decrease when going from $A = 67$ to $A = 69$. The two particle-two hole (2p-2h) configuration involved in the structure of the $3/2_2^-$ state in ^{69}Cu is expected to be mainly concentrated in this state, and some fragmentation is needed to account for branching to the ground state. Using the upper limit of 36% obtained for the $\beta-$branching to the ground state of ^{69}Cu in the decay of ^{69}Ni^{m1}, the amount of 2p-2h configuration mixing in the ground-state was determined to be $< 15\%$. This value was deduced by relating the ft values for the isomeric beta decay to the ground and excited $3/2^-$ states in ^{69}Cu to the probabilities of observing these states with a $\pi 2p_{3/2} \otimes \nu(1g_{9/2}^2 2p_{1/2}^{-2})$, a^2, and a pure $\pi 2p_{3/2}$, b^2, configuration,

$$\frac{ft(3/2_1^-)}{ft(3/2_2^-)} = \frac{a^2}{b^2}$$

assuming that ^{69}Ni^{m1} would beta decay to only one of these two states ($a^2 + b^2 = 1$).

A similar 2p-2h admixture was calculated for the ground-state of ^{67}Co, using a QRPA approach, in a recent $\beta-$decay study of the ^{67}Co $\rightarrow$ ^{67}Ni by Weissman *et al.* [46]. In that case, the neutron 2p-2h admixture in the $7/2^-$ ground state of ^{67}Co can produce a $\beta-$branch to a state with mainly a $\nu 1f_{5/2}^{-1} \otimes \nu(1g_{9/2}^2 2p_{1/2}^{-2})$ configuration via the allowed $\nu 1f_{5/2} \rightarrow \pi 1f_{7/2}$ GT transition, see Fig. 5.10. Experimental evidence

was found for the population of a second $5/2^-$ state at 2.1 MeV with $\log ft = 5.5$. The interpretation in terms of the above configuration is only tentative. Particle-vibration coupling can give rise to fragmentation of the single-particle strength in nuclei around closed shells (see for example, the study of ^{57}Cu $\rightarrow$ ^{57}Ni by Trache *et al.* [47]), and a non-negligible fragment of the hole-state $f_{5/2}^{-1}$ in a state with mainly a $2^+(^{68}\mathrm{Ni}) \otimes p_{1/2}^{-1}$ structure can be expected around the energy of 2.1 MeV.

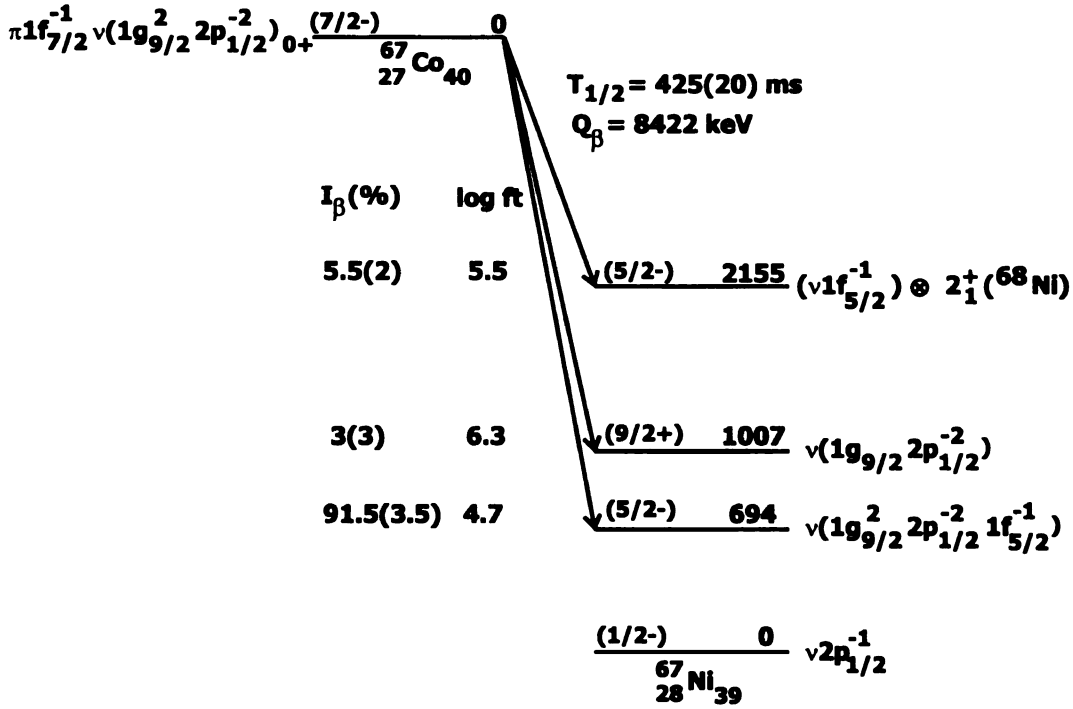

Figure 5.10: The low-energy level scheme of ^{67}Ni following the beta decay of ^{67}Co. The configurations for the excited and ground states of the parent and daughter nuclide have been labelled as discussed in Ref. [46].

The $< 15\%$ 2p-2h mixing deduced for the ground state of ^{69}Cu is only an upper limit, derived from the upper limit of 36% on the $\beta-$branching from the ^{69}Ni $1/2^-$ isomer to the ^{69}Cu ground state. Taking the β branch for this decay as zero, which would translate to no 2p-2h mixing in the ground state of ^{69}Cu, the $\log ft$ value for the $3/2_2^-$ state in ^{69}Cu becomes 4.3. It should be noted that if the branch for the $^{69}\mathrm{Ni}^{m1}$ decay to the ground state of ^{69}Cu is near the established upper limit, its origin can be readily explained by the configuration mixing arguments presented above. In fact,

the 2p-2h configuration is the only low-lying configuration expected to be populated in the allowed GT transition from the 2p-1h $1/2^-$ isomer. Another higher-energy GT transition $\nu 1f_{5/2} \rightarrow \pi 1f_{5/2}$ can lead to the $\pi 1f_{5/2} \otimes (\nu 2p_{1/2}^{-1} 1f_{5/2}^{-1} 1g_{9/2}^2)$ configuration. This has some overlap with the particle-vibration configuration $\pi 1f_{5/2} \otimes 2^+(^{68}\mathrm{Ni})$ and can give a small admixture in the $3/2^-_{g.s.}$. The quadrupole matrix element for $f_{5/2}$ - $p_{3/2}$ is small, due to the spin-flip involved. The resulting admixture would result in a $\beta-$ branch with a relatively large log ft value.

The degree of 2p-2h correlations in the ground state of ^{68}Ni, evident from the configuration mixing derived experimentally in ^{69}Cu, can provide a measure of the validity of the $N = 40$ subshell closure. Assuming the $\nu(2p_{1/2}^{-2} 1g_{9/2}^2)$ mixing in the ground state of ^{68}Ni is similar to that deduced for ^{67}Co and ^{69}Cu, such a small value ($< 15\%$) suggests "double-magic" (proton shell closure and neutron subshell closure) character of this nucleus. A reduced mixing is also consistent with the predicted deformed character of the 0_2^+ state in ^{68}Ni [39]. However, with limited mass measurements of Ni isotopes in this region, this interpretation cannot be substantiated by the present data available (experimental and extrapolated) for two-neutron separation energies [5].

5.1.1.2 Summary

A 3.4(7) s isomeric state has been directly populated in ^{69}Ni following fragmentation of a ^{76}Ge beam at 70 MeV/nucleon in a Be target. This state, proposed to have a configuration $\nu(p_{1/2}^{-1} g_{9/2}^2)$, was observed to populate a single excited $3/2^-$ state at 1296.1(2) keV in the daughter ^{69}Cu with an allowed GT transition ($\log ft \leq 4.54$). A β branch to the $3/2^-$ ground state of ^{69}Cu in the β decay of the ^{69}Ni $1/2^-$ isomer can result from a neutron two particle - two hole admixture in the ground state of ^{69}Cu. Based on an upper limit of 36% for this β branch, an upper limit of $< 15\%$ was deduced for the configuration mixing, similar to that deduced for ^{67}Co [46]. This small 2p-2h admixture in the ground state of ^{69}Cu suggests that this nucleus exhibits single-particle character and can be described as a proton coupled to a ^{68}Ni core. The

dominance of a ^{68}Ni core in the excited states of ^{69}Cu provides a strong case for the $N = 40$ subshell.

5.1.2 Neutron-Rich Nuclides Near $N = 32$

To determine the robustness of the $N = 40$ subshell, it was of interest to pursue increasingly neutron-rich nuclei in the vicinity of $N = 40$. If $N = 40$ is a good subshell closure for ^{68}Ni, then it may develop into a real shell closure for lighter mass systems [40]. Thus, in an attempt to characterize $N = 40$, nuclei in the midshell region of $N = 28 - 40$ were examined. One would expect the collective nature of these nuclei to be maximum at midshell. However, systematics for Ca isotopes in this region suggest the existence of a new subshell at $N = 32$. Such a subshell would diminish the extent of quadrupole collectivity associated with nuclei in this midshell region.

Based on self-consistent energy density calculations, Tondeur [48] proposed $N = 32$ as a new magic number for neutron-rich nuclides. Following the beta decay of ^{52}K, Huck *et al.* [2] assigned the 2.56 MeV state in $^{52}_{20}Ca_{32}$ a spin and parity of 2^+ at a significantly higher energy compared to the first excited 2^+ level in ^{50}Ca. Based on this finding, Huck *et al.* [2] suggested the rise at $N = 32$ was due to the $\nu 2p_{3/2}$ subshell closure, indicating that $N = 32$ was semi-magic. This assertion was consistent with Tondeur's theoretical prediction [48]. Following a mass measurement of ^{52}Ca [49], an increase in binding was also noted at $N = 32$. However, when considering the rise in $E(2_1^+)$ for ^{52}Ca, one must bear in mind the uncertainty associated with the spin and parity assignment of this state. In addition, in the absence of mass measurements for ^{54}Ca and more neutron-rich calcium isotopes, the systematic variations of pairing energy and two-neutron separations are inconclusive. Using a shell-model calculation, Richter *et al.* [50] predicted the first excited 2^+ state of ^{52}Ca will lie at 1.85 MeV. Recalculating the single-particle energies of this nuclide based on a shell-model plus Hartree-Fock approximation [51], the 2_1^+ state was predicted at 1.91 MeV. Both of these theoretical values are significantly lower than the suggested experimental value

of 2.56 MeV. Based on this finding, the authors [50,51] attributed the rise in $E(2_1^+)$ to the filling of the $\nu 2p_{3/2}$ subshell, suggesting $N = 32$ is a good subshell closure for calcium.

The motivation for the present study was to explore the mass region $A = 50 - 60$ to confirm the $N = 32$ subshell closure for neutron-rich nuclides. For this work, the properties of neutron-rich Cr isotopes were examined.

5.1.2.1 Beta decay of ^{58}V

Similar to the case of $^{52}_{20}Ca_{32}$, the first 2^+ state of $^{56}_{24}Cr_{32}$ lies higher in energy relative to its $N-2$ neighbor, $^{54}Cr_{30}$. However, unlike $^{52}Ca_{32}$, the spin and parity assignment of the 2^+ level for $^{56}Cr_{32}$ was deduced from the shape of proton angular distribution curves following its production via the (t,p) reaction [52]. A second (t,p) study confirmed the spin-parity assignments for a number of states, including the first excited 2^+ state at 1007 keV [53]. The authors also reported that shell model calculations reproduced the energy of the first excited 2^+ state. To determine whether the first excited 2^+ energies continued to rise or peaked at $N = 32$, it was necessary to measure $E(2_1^+)$ beyond $N = 32$. Thus, for this study, the low-lying levels of $^{58}Cr_{34}$ were investigated.

Ameil *et al.* [30] recently measured the β-decay half-lives of several neutron-rich isotopes of Ti to Ni following their production via the fragmentation of a 500 MeV/nucleon ^{86}Kr beam in a thick Be target at GSI. One of the nuclides produced during this reaction was ^{58}V. Following its beta decay, a half-life of 200(20) ms was extracted. Sorlin *et al.* [29] have also investigated the beta decay properties of neutron-rich nuclides in this region of the chart of the nuclides. Following the fragmentation of a 64.5 MeV/nucleon ^{65}Cu beam in a ^{9}Be target, neutron-rich Sc and V isotopes were produced at GANIL. During this study, a 205(20) ms beta decay half-life was measured following the decay of ^{58}V. In addition, a beta-delayed gamma ray spectrum was acquired, see Fig. 5.11. Sorlin *et al.* observed a broad peak at 900(100) keV in BGO scintillator detectors following the beta-delayed gamma emission of ^{58}V. This 900-

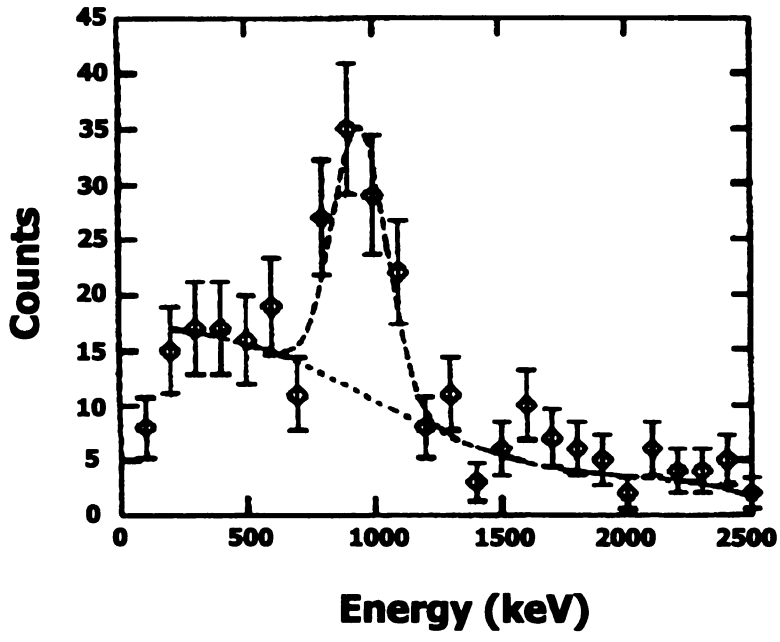

Figure 5.11: Beta-delayed gamma ray spectrum following the decay of ^{58}V observed by Sorlin *et al.* [29].

keV transition had a FWHM approximately twice that of other transitions observed in their BGO detectors. The authors proposed this peak as a doublet, which may contain the $4^+ \rightarrow 2^+ \rightarrow 0^+$ cascade. Assuming $E(2_1^+) = 800$ keV and $E(4_1^+) = 1800$, their $E(4_1^+)/E(2_1^+) = 2.25$, suggesting that ^{58}Cr was predominately governed by vibrational collective motion and that rotational collectivity near the middle of the $N = 28 - 40$ subshell was modest at best. In addition, Sorlin *et al.* extracted an 80(10)% beta branch to the 900(100) keV state following the ground state beta decay of ^{58}V.

To study the low-energy properties of ^{58}Cr, the decay of its parent nuclide, ^{58}V, was monitored using the DSSD experimental setup discussed in Sec. 3.2.2. Figure 4.1b shows the correlated fragment implant-decay events for all nine radionuclides produced during this experiment. By defining a gate in the correlated energy loss versus TOF spectrum, the decay properties of ^{58}V were deduced similar to the method discussed in Sec. 4.0.3. A half-life curve was obtained (see Fig. 5.12a) by taking the difference between the absolute time of fragment implant and subsequent beta decay.

A $T^{\beta}_{1/2}$ = 180(36) ms was extracted by fitting the data in Fig. 5.12a with a two component exponential, one component for ^{58}V and the other for the background, in PHYSICA. A lifetime curve was also obtained by correlating ^{58}V fragments with beta-delayed gamma rays of energy 880 keV within a 400 ms time window following implantation (see discussion below). Considering this half-life, $T^{\beta-\gamma}_{1/2}$ = 218(30) ms, along with $T^{\beta}_{1/2}$, an adopted half-life of 202(36) ms was obtained for the decay of ^{58}V. This half-life is consistent with previous measurements performed by Sorlin *et al.* [29] and Ameil *et al.* [30].

A beta-delayed gamma ray spectrum was obtained by accepting gamma rays observed within a 200 ms time window following the implantation of ^{58}V nuclides. This spectrum was corrected for random background as discussed in Chapter 4, with a background correction factor of 0.184. By multiplying the total gamma spectrum by this correction factor and subtracting the resulting spectrum from the ^{58}V-gamma spectrum, a background subtracted ^{58}Cr spectrum was obtained, see Fig. 5.12b. A single gamma-ray peak was observed at 879.9(2) keV in the background corrected beta-delayed gamma ray spectrum below 1.5 MeV (see Fig. 5.12b). This result is in general agreement with the work of Sorlin *et al.* [29] who observed a broad peak at 900(100) keV following the beta-delayed gamma emission of ^{58}V. Although the authors proposed this peak as a doublet, no evidence for a second transition in the range 800 - 1000 keV, with similar intensity to the 880-keV gamma ray, was observed in the present study.

In an attempt to extract a beta decay branch from the ground state of ^{58}V to the 880 keV state in ^{58}Cr, a second beta-delayed gamma ray spectrum was generated by gating the the total gamma ray spectrum on the ^{58}V contour discussed above. A peak at 880 keV was observed with 8±3 counts. Considering Eq. 4.2 and the number of ^{58}V implants (2.95(1) x 10^5), a 54^{+39}_{-44}% beta decay branch from the ground state of ^{58}V to the 880 keV state in ^{58}Cr was determined. From this branching ratio and the half-life of ^{58}V, a log ft range of $4.12 \leq \log ft \leq 6.01$ was extracted, suggesting that the 880 keV state is populated following an allowed beta transition.

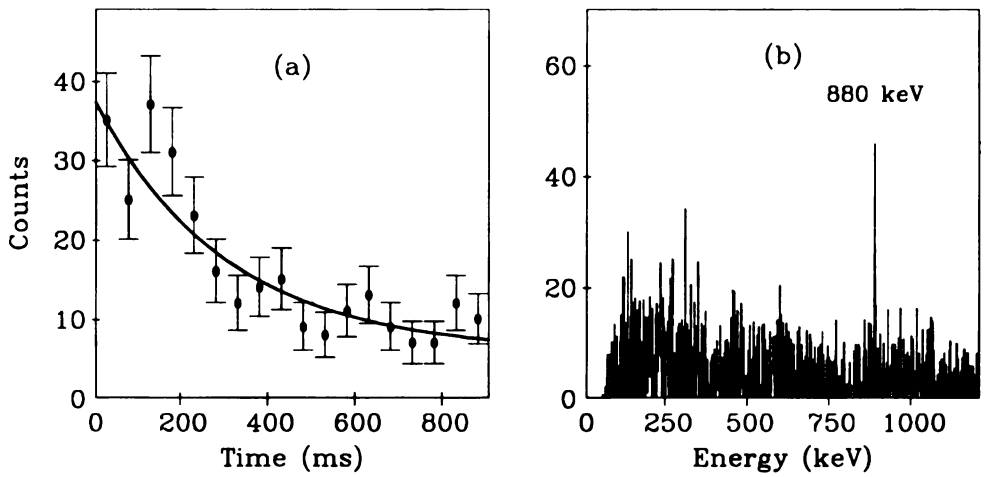

Figure 5.12: (a) Extracted ^{58}V life-time curve following the correlation of ^{58}V implants and subsequent beta decays. (b) β-delayed gamma-ray spectrum following the decay of ^{58}V.

In general, the depopulation of excited states in even-even nuclei is characterized by a significant portion of the gamma ray intensity passing through the first excited 2^+ state. Thus the $2_1^+ \rightarrow 0_1^+$ transition should be the most intense. One exception, in some even-even nuclei, is the presence of a 3^- state at similar energy to the 2_1^+ state. However, the systematics of the lighter Cr isotopes do not support a low-energy 3_1^- state in this mass region. Therefore, the 880-keV β-delayed gamma ray observed in the present study is proposed as the $2_1^+ \rightarrow 0_1^+$ transition in ^{58}Cr. The absence of a second beta-delayed gamma ray transition feeding the first excited 4^+ state in ^{58}Cr may be an indication of a low spin ground state for ^{58}V. Considering the jj-coupling model for odd-odd nuclei [54], the ground state spin of ^{58}V is predicted to be 1, which would result in strong beta feeding to the first excited 2^+ state and minimal feeding to the first excited 4^+ state. This ground-state spin-parity assignment for ^{58}V is also in agreement with an allowed beta transition feeding a 2^+ state in ^{58}Cr.

The low-energy level structures of the neutron-rich chromium isotopes in the range $N = 28 - 36$ are shown in Fig. 5.13, where the data were obtained from Ref. [9,55–57]. As compared to $^{54}Cr_{30}$ and the new measurement for $^{58}Cr_{34}$, there is a clear rise in $E(2_1^+)$ for $^{56}Cr_{32}$. This peak in the $E(2_1^+)$ value for $^{56}Cr_{32}$ provides empirical evidence for a significant subshell gap at $N = 32$.

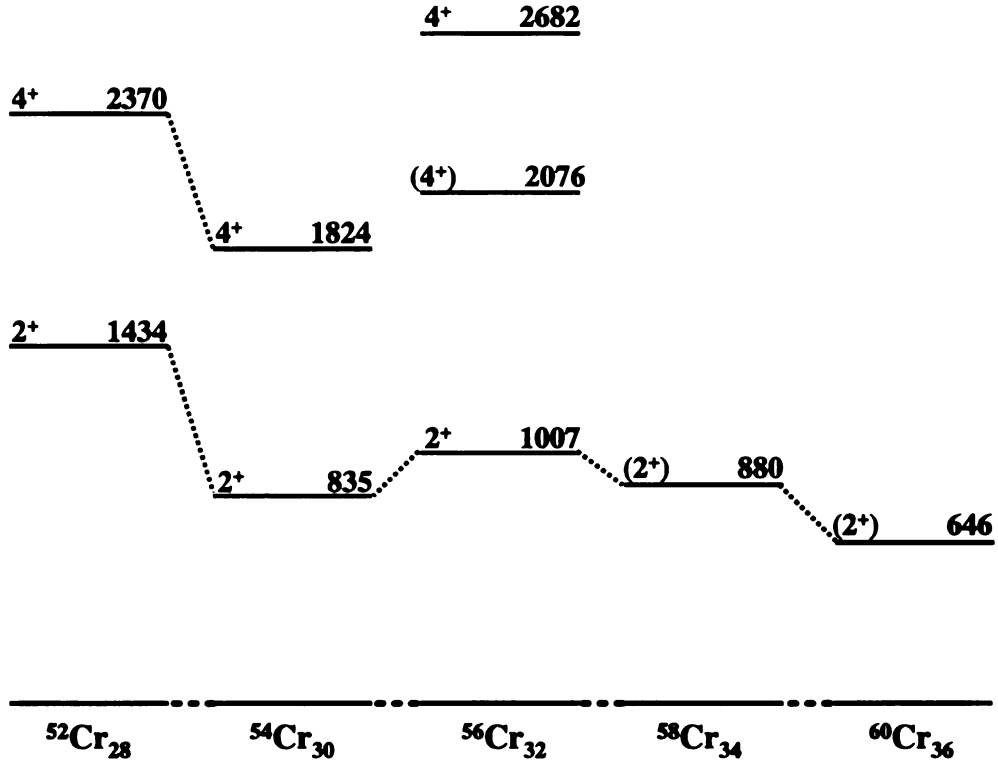

Figure 5.13: Low-energy level scheme for neutron-rich chromium isotopes in the range $28 \leq N \leq 36$. The $E(2_1^+)$ values were obtained from Ref. [9, 55–57].

Tu *et al.* [49] attributed the increase in binding at $N = 32$ for ^{52}Ca to the $Z = 20$ shell closure. However, based on the present measurement, a peak in $E(2_1^+)$ is now seen for $^{56}Cr_{32}$, which resides in the middle of the $Z = 20 - 28$ shell. In addition, although $E(2_1^+)$ values increased at $N = 32$ for the calcium isotopes, this behavior is not observed for nickel (see Fig. 5.14, data taken from Ref. [9, 19, 55, 56]), which has a closed proton shell. If the strength of $N = 32$ were reinforced by a proton shell closure, a similar peak in $E(2_1^+)$ would be expected for ^{60}Ni.

An alternative explanation for the appearance of the $N = 32$ subshell for neutron-rich systems is to consider a change in the proton-neutron monopole interaction strength. Nickel has a closed proton shell at $Z = 28$. According to Federman and Pittel [58], the proton-neutron interaction is strongest when the orbitals they occupy strongly overlap. To illustrate this point, consider the following interaction between

two particles at r_1 and r_2 [10]:

$$V(|r_1, r_2|) = \sum_{k=0}^{\infty} \nu_k(r_1, r_2) P_k(cos\theta_{12}) \tag{5.12}$$

which is summed over all multipoles, k. $P_k(cos\theta_{12})$ is a Legendre polynomial. The term $\nu_k(r_1, r_2)$ may be reduced to:

$$\nu_k(r_1, r_2) \approx \frac{2k + 1}{4\pi} \frac{\delta(r_1 - r_2)}{r_1 r_2} \tag{5.13}$$

where $\delta(r_1 - r_2)$ is a zero-range interaction. Reducing this expansion to its first term, the monopole term, gives:

$$V_M(|r_1, r_2|) = (\frac{1}{4\pi})^{3/2} \frac{\delta(r_1 - r_2)}{r_1 r_2} \tag{5.14}$$

The overlap between the proton and neutron orbitals is maximum when $\ell_n \approx \ell_p$ [58]. This results in a shift in the single-particle orbitals [59]:

$$\tilde{\varepsilon}_{j\nu} = \varepsilon_{j\nu} + \sum_{j\pi} < j_\pi j_\nu | V_M | j_\pi j_\nu > \nu^2_{j_\pi} \tag{5.15}$$

where $\nu^2_{j_\pi}$ is the proton occupation probability. When $Z = 28$, the $1f_{7/2}$ orbital is filled and the $\pi 1f_{7/2}$ - $\nu 1f_{5/2}$ interaction should be strong, depressing the energy of the $\nu 1f_{5/2}$ orbital [60]. The $1f_{5/2}$ neutrons would act to stabilize the $1f_{7/2}$ proton configuration [61]. As protons are removed from the $1f_{7/2}$ orbital, the $\pi 1f_{7/2}$ - $\nu 1f_{5/2}$ interaction weakens. When $Z = 20$, no protons occupy the $1f_{7/2}$ orbital in the ground state, thus the $\pi 1f_{7/2}$ - $\nu 1f_{5/2}$ interaction should be diminished. This reduced monopole interaction, and the significant $2p_{1/2} - 2p_{3/2}$ spin-orbit energy splitting, results in the emergence of the $N = 32$ subshell.

To probe the proton-neutron monopole interaction, ideally, the single-particle energies for the $2p_{3/2}$, $2p_{1/2}$ and the $1f_{5/2}$ orbitals should be measured. These energies may be deduced for the odd-A, $N = 29$ isotones using spectroscopic factors extracted from the analysis of transfer reactions. In an attempt to extract the single-particle energies for the $N = 29$ isotones, the spectroscopic factors for the known $3/2^-$, $1/2^-$, $5/2^-$ and $7/2^-$ states were tabulated (see Table 5.1, complete data for $N = 29$ isotones are provided in Appendix D). However, the experimental information is limited.

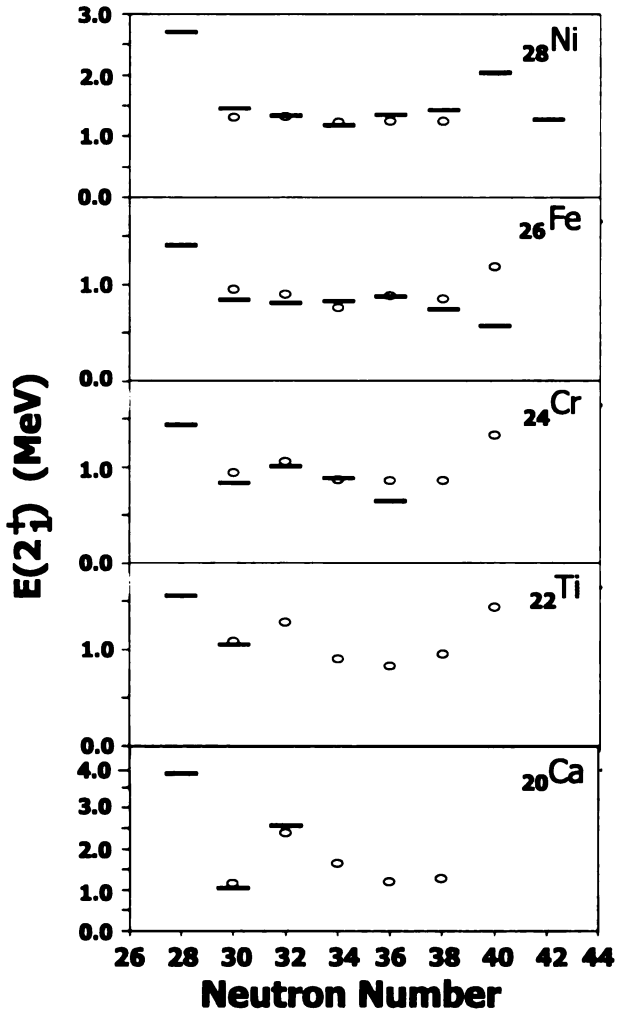

Figure 5.14: $E(2_1^+)$ systematics for neutron-rich nuclides between $20 \leq Z \leq 28$. The experimental values are denoted by dashes, where the data were obtained from Ref. [9, 19, 55, 56]. The open circles represent $E(2_1^+)$ values obtained from truncated shell-model calculations. See text for details.

Not all of the states have been assigned a spectroscopic factor, thus the single-particle energies cannot be correctly calculated. An additional complication may arise from the misassignment of spins. An example of such complications may be found in ^{53}Cr. A large spectroscopic factor has been extracted for a high-energy state at 3.63 MeV [62]. However, there is some uncertainty pertaining to the spin of this $\ell = 1$ state [62,63], which seriously impacts the ordering of the single-particle orbitals.

Due to the difficulty in extracting single-particle energies from experimental data for the $N = 29$ isotones, several authors have calculated these values. The single-

Table 5.1: Calculated single-particle energies (s.p. E(keV)) for the $N = 29$ isotones in the region $20 \leq Z \leq 28$ [9,64–68].

Nuclide	*Neutron Single-Particle Orbitals*	*Single-Particle Energy* (keV)
^{49}Ca	$2p_{3/2}$	95.2
	$2p_{1/2}$	2059.3
	$1f_{5/2}$	3986.1
^{51}Ti	$2p_{3/2}$	83.2
	$2p_{1/2}$	1671.0
	$1f_{5/2}$	2136.0
^{53}Cr	$2p_{3/2}$	366.6
	$2p_{1/2}$	1287.0
	$1f_{5/2}$	1009.0
	$1f_{7/2}$	1302.3
^{55}Fe	$2p_{3/2}$	215.4
	$2p_{1/2}$	482.8
	$1f_{5/2}$	997.2
	$1f_{7/2}$	1334.0
^{57}Ni	$2p_{3/2}$	30.0
	$2p_{1/2}$	1113.0
	$1f_{5/2}$	769.0
	$1f_{7/2}$	3547.7

particle energies for $2p_{3/2}$, $2p_{1/2}$ and $1f_{5/2}$ orbitals in the $N = 3$ shell for $^{57}Ni_{29}$ have been calculated by Trache *et al.* [47] and Duflo and Zuker [69]. Considering a ground state spin of 3/2 for ^{57}Ni [68], the lowest orbital in this shell would be $2p_{3/2}$. The $1f_{5/2}$ state was calculated at $\approx$ 1 MeV above $2p_{3/2}$, followed by $2p_{1/2}$. As protons are removed from $1f_{7/2}$, the single-particle energies for the $2p_{3/2}$, $2p_{1/2}$ and $1f_{5/2}$ orbitals shift. By $^{49}Ca_{29}$, the $\nu 1f_{5/2}$ and the $\nu 2p_{1/2}$ orbitals have inverted [69].

For this study, shell-model calculations[1] in the region $N = 28-40$ and $Z = 20-28$ were carried out in a *pf*-shell model space with an FPD6 effective interaction [55,70]. For the Ca isotopes the full basis calculation is feasible. The calculated energies of the lowest 2^+ states in the Ca isotopes are (in MeV) 3.66 (^{48}Ca), 1.33 (^{50}Ca), 2.75 (^{52}Ca), 1.47 (^{54}Ca), 1.37 (^{56}Ca) and 1.30 (^{58}Ca). The agreement with the experimental values in ^{48}Ca, ^{50}Ca and ^{52}Ca is good. The high energy of the 2^+ state in ^{48}Ca is due to a

[1]Shell model calculations were performed by B.A. Brown.

rather good $1f_{7/2}$ shell closure, and the relatively high energy for the 2^+ state in ^{52}Ca is due to a partial shell closure for the $2p_{3/2}$ shell. Beyond ^{52}Ca the effective single-particle energies of the $2p_{1/2}$ and $1f_{5/2}$ orbits are close and there are no other shell effects until the ^{60}Ca closed shell. In nuclides around ^{60}Ca the $1g_{9/2}$ orbit may become important, but this is not included in the model space and there is no experimental information available.

For nuclei with larger values of Z, the shell-model calculation in the full pf shell quickly becomes intractable because of the large dimensions. In a few cases such as ^{56}Ni, the Monte-Carlo shell-model has been used [71] (for which the FPD6 interaction still gives a good spectrum). However, the good closure of the $1f_{7/2}$ shell at ^{48}Ca means the nuclei beyond $N = 28$ may be treated as neutrons in the ($2p_{3/2}$, $2p_{1/2}$, $1f_{5/2}$) model space (to a good approximation). When this truncation is made for the Ca isotopes the energies of the 2^+ states (see Fig. 5.14) and their wave functions remain similar to those obtained with the full space, which includes $1f_{7/2}$. (These truncated calculations use as inputs the single-particle levels in ^{49}Ca as obtained from FPD6 which are close to the experimental values.) For higher Z there is clear evidence of the dominance of the $1f_{7/2}$ shell for protons in the 0^+, 2^+, 4^+, 6^+ spectra of ^{50}Ti, ^{52}Cr and ^{54}Fe. ^{56}Ni shows a partial $1f_{7/2}$ shell closure (e.g. the relatively high 2^+ energy). Thus for protons, the model space is truncated to the pure $1f_{7/2}$ shell with the proton two-body interaction taken as a function of Z to match exactly the 0^+, 2^+, 4^+, 6^+ spectra of ^{50}Ti, ^{52}Cr and ^{54}Fe. The neutron single-particle energies are linearly interpolated between ^{49}Ca and ^{57}Ni such that the spectrum of single-particle states in ^{57}Ni is reproduced. This defines the input to the shell-model interpretation of the 2^+ energies.

Figure 5.15 depicts the low-energy level structure for the odd A, $N = 29$ isotones within the vicinity $20 \leq Z \leq 28$, where data was taken from Ref. [9]. For comparison, the levels predicted via shell-model calculations for ^{49}Ca and ^{57}Ni are also shown. The energies of the $3/2^-$, $1/2^-$ and $5/2^-$ states follow the general behavior of the $\nu 2p_{3/2}$, $\nu 2p_{1/2}$ and $\nu 1f_{5/2}$ orbitals, respectively (see Table 5.1). At $Z = 20$, a substantial

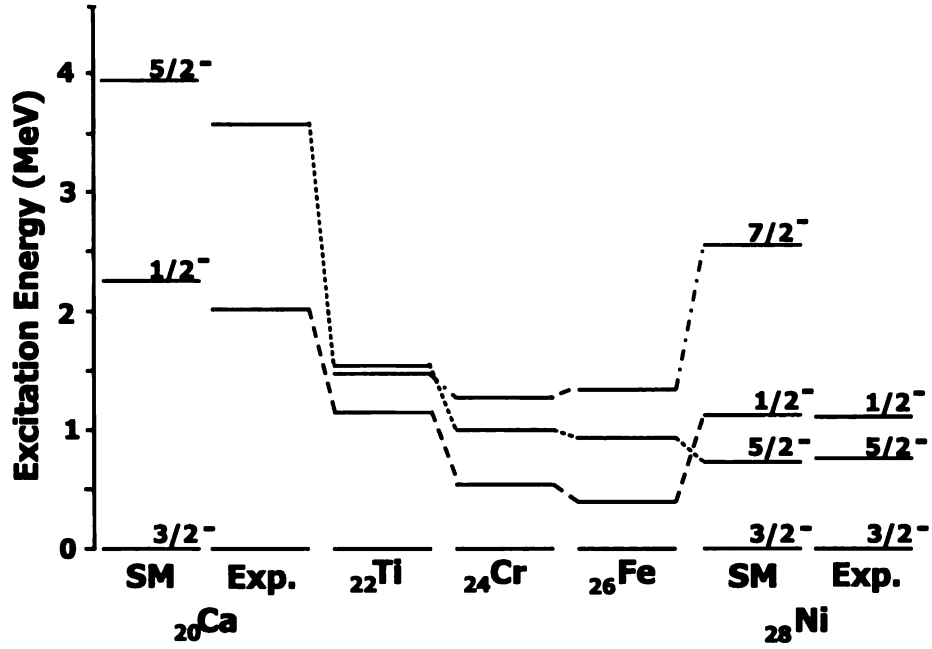

Figure 5.15: Low-energy states for the odd-A $N = 29$ isotones in the range $20 \leq Z \leq 28$ [9]. Shell-model results for ^{49}Ca and ^{57}Ni are also depicted.

gap is observed between the $\nu(2p_{1/2} - 1f_{5/2})$ and the $\nu(2p_{3/2} - 2p_{1/2})$ orbitals. The existence of these gaps suggests an $N = 32$ and possibly an $N = 34$ subshell for calcium isotopes. As protons begin to fill the $1f_{7/2}$ orbital, the $5/2^-$ state is lowered. By Ni, the $\pi 1f_{7/2}$ - $\nu 1f_{5/2}$ interaction is maximum and draws the $\nu 1f_{5/2}$ orbital below $\nu 2p_{1/2}$, which eliminates $N = 32$ subshell closure.

For chromium isotopes beyond $N = 32$, in addition to the present measurement, Sorlin *et al.* [56] observed the $2_1^+ \rightarrow 0_1^+$ transition of ^{60}Cr at 646 keV following the beta decay of ^{60}V. Considering the new $E(2_1^+)$ measurement for ^{58}Cr at 880 keV and Sorlin's measurement [56], a considerable decrease in $E(2_1^+)$ is observed beyond $N = 32$ for Cr (see Fig. 5.13). The overall $E(2_1^+)$ trends in neutron-rich chromium isotopes imply that as neutrons fill the $1f_{5/2}$ orbital, the $\pi 1f_{7/2}$-$\nu 1f_{5/2}$ quadrupole interaction strengthens, inducing nuclear deformation [58]. Such effects have been previously noted in, for example, the Mo isotopes, where a strong $\pi 1g_{9/2}$ - $\nu 1g_{7/2}$ proton-neutron interaction produces deformed ground state structures beginning at ^{100}Mo [72]. The relatively low energy of the first excited 2^+ state of Cr, as compared with Fe, Zn and

Ge isotopes (see Fig. 5.14), has been suggested as evidence of oblate-prolate shape coexistence predicted in this region [56]. As a result of the monopole proton-neutron interaction, shape coexistence may be rationalized as follows. As neutrons are added to a $^{56}Cr_{32}$ core, the $\pi(1f_{7/2})$-$\nu(1f_{5/2})$ interaction strengthens and may draw a pair of $1d_{3/2}$ protons into the $1f_{7/2}$ orbital. The energy required to promote the $d_{3/2}$ protons through the $Z = 20$ shell closure would be recovered from the monopole energy. Toward $N = 40$, the monopole proton-neutron interaction will become increasingly strong and may result in a new proton configuration, possibly leading to an oblate-prolate shape coexistence for Cr isotopes in this region. However, based on shell model calculations for chromium isotopes (see Fig. 5.14) the 2_1^+ energy level is predicted to remain fairly constant for $34 \leq N \leq 38$.

5.1.2.2 Summary

The decay properties of ^{58}Cr have been studied following the beta decay of ^{58}V. A beta-delayed gamma ray was observed at 879.9(2) keV and has been assigned to the $2_1^+ \rightarrow 0_1^+$ transition in ^{58}Cr. A beta decay branching ratio of 54^{+39}_{-44}% has been extracted for the ground state beta decay of ^{58}V to the 880 keV state in ^{58}Cr. A $\log ft$ range of $4.12 \leq \log ft \leq 6.01$ has been determined, which suggests that the 880 keV state is populated by an allowed beta transition from the ground state of ^{57}V. Considering that the 880 keV state is fed by an allowed beta transition and the jj-coupling model for odd-odd nuclei [54], the ground state spin and parity of ^{58}V is predicted to be 1^+.

The even-even systematics of the neutron-rich chromium isotopes indicate an increase in $E(2_1^+)$ at $N = 32$. Following the present measurement, $E(2_1^+)$ for chromium isotopes were found to peak at $N = 32$. This rise in $E(2_1^+)$ is consistent with the increase observed at $N = 32$ for calcium isotopes. Although this trend does not continue beyond $Z = 24$, this may be due to the lowering of the $\nu 1f_{5/2}$ orbital as a result of a strong $\pi 1f_{7/2}$ - $\nu 1f_{5/2}$ proton-neutron monopole interaction. The data is in agreement with shell-model calculations, which also show enhanced binding at $N = 32$ for $_{20}$Ca,

$_{22}$Ti and $_{24}$Cr.

Chapter 6

Summary

Two experiments have been performed to study the evolution of subshell gaps at $N = 32$ and $N = 40$ for neutron-rich nuclides within the $N = 28 - 50$ shell.

In the first experiment, a conventional beta detection system was used to study the beta decay of neutron-rich nuclides near $N = 40$. During this study, a 3.4(7) s isomeric state in ^{69}Ni was directly produced following the fragmentation of a ^{76}Ge beam at 70 MeV/nucleon in a Be target. The identification of this isomeric state was based on a newly discovered 1296 keV beta-delayed gamma ray. The decay of the $1/2^-$ isomer in ^{69}Ni was observed to proceed mainly through the excited $3/2^-$ state at 1296 keV in ^{69}Cu. No other excited states in ^{69}Cu have been observed to be fed following the β decay of this isomer. By comparing the total number of ^{69}Ni nuclei implanted within a Si PIN detector with the intensities of the beta-delayed γ rays following the decay of the $1/2^-$ isomeric state and the ground state of ^{69}Ni, a 36% upper limit has been extracted for the β branch from the isomeric state in ^{69}Ni to the ground state in ^{69}Cu. Based on this branching ratio, a small ($< 15\%$) 2p-2h mixing into the ground state of ^{69}Cu may be deduced. This small 2p-2h admixture in the ground state of ^{69}Cu suggests that this nucleus is predominately single-particle in character and may be described as a proton coupled to a ^{68}Ni core. The dominance of the ^{68}Ni core in the excited states of ^{69}Cu supports the case for an $N = 40$ subshell.

In the second experiment, a new beta detection system was employed to study the decay properties of neutron-rich nuclides in the midshell region $N = 28 - 40$. A

985 μm double-sided silicon strip detector (DSSD) was utilized to correlate implanted nuclei with subsequent beta particles on an event-by-event basis. For this study, the $N = 32$ subshell was investigated. An $N = 32$ subshell gap was first suggested following the measurement of the high-lying 2_1^+ state of $^{52}Ca_{32}$ [2]. Although extending the $E(2_1^+)$ systematics to heavier calcium isotopes would be of value, such nuclei were difficult to produce with sufficient statistics during the time of this experiment. Thus, in this work, the low-energy properties of ^{58}Cr were studied following the beta decay of ^{58}V. A beta decay half-life of 202(36) ms was extracted which was consistent with Sorlin *et al.* [29] and Ameil *et al.* [30] measurements. In addition, a beta-delayed gamma ray was observed at 879.9(2) keV and has been assigned to the $2_1^+ \rightarrow 0_1^+$ transition in ^{58}Cr. Based on a beta decay branch of $54^{+39}_{-44}\%$, a range of $\log ft$ values of $4.12 \leq \log ft \leq 6.01$ have been extracted, suggesting the 880 keV state in ^{58}Cr is populated by an allowed beta transition from the ground state of ^{58}V.

Considering the $E(2_1^+)$ value for $^{54}Cr_{30}$ and the present measurement for $^{58}Cr_{34}$, a clear peak in $E(2_1^+)$ is apparent at $N = 32$. This rise in $E(2_1^+)$ is consistent with the calcium systematics. However, this trend does not seem to continue beyond $Z = 24$. The presence of a substantial $N = 32$ subshell gap has been attributed to the lowering of the $\nu 1f_{5/2}$ orbital as a result of a strong $\pi 1f_{7/2}$ - $\nu 1f_{5/2}$ proton-neutron monopole interaction.

The systematics of even-even, neutron-rich chromium isotopes indicate a gradual increase in $E(2_1^+)$ toward $N = 40$, see Fig. 5.15. This evolution suggests a slow onset of collectivity in the midshell region $N = 28 - 50$. However, this is in contrast to the shell model predictions shown in Fig. 5.14. Based on shell model calculations, $E(2_1^+)$ values for neutron-rich nuclides between $20 \leq Z \leq 28$ increase toward $N = 40$, in support of an $N = 40$ subshell. Discrepancies such as those observed between the experimental systematics and the shell model predictions toward $N = 40$ illustrate the need for continued experimental studies of exotic nuclear systems. It would be of interest to extend the study of the $N = 28 - 40$ midshell and the $N = 40$ subshell to lighter mass systems.

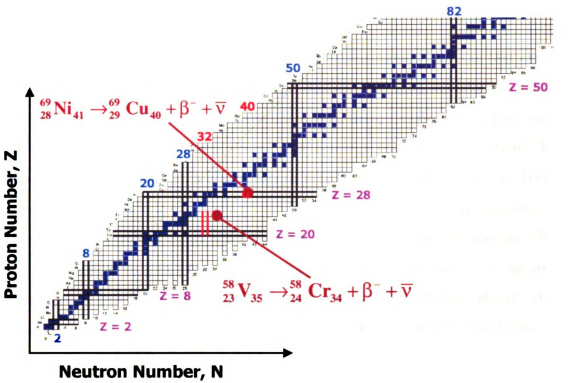

Figure 6.1: A table of the isotopes with the magic neutron (labelled with blue numbers) and magic proton (labelled with pink numbers) shell closures indicated. The $N = 40$ and $N = 32$ subshells have also been included. The blue squares that run nearly along the diagonal represent stable nuclei.

In summary, two subshell gaps within the $N = 28 - 50$ shell have been explored. As a result of the $^{69}Ni^{m1}$ beta-decay study, further support for an $N = 40$ subshell has been provided. However, based on this study, this subshell can only be confined to the nickel isotopes (see Fig. 6.1). Following the beta decay study of ^{58}V, new empirical evidence for an $N = 32$ subshell has been established. This subshell has been attributed to a proton-neutron monopole interaction and is believed to extend from calcium to chromium (see Fig. 6.1). To validate this hypothesis it would be of interest to measure the $E(2_1^+)$ values for neutron-rich Ca and Ti isotopes, in particular $^{52,54}Ca$ and $^{54,56}Ti$.

6.0.3 Outlook

The beta detection system discussed for the ^{57,58}V measurement was the first experiment of its kind run at the NSCL utilizing a double-sided strip detector to directly correlate fragments of interest with subsequent beta decays during continuous beam implantation. As such, there were several shortcomings that were encountered. For instance, using single high gain electronics to process energy signals from the DSSD allowed us to isolate a beta event to a given pixel, however, in terms of an implant, one could only isolate such an event to a 6 x 6 strip area. An implant pixel was identified as the most central strip in x and y in this 36 pixel array. In addition, i$\pm$1 strips were also labelled as possible implant pixels. As a result of this limitation, shortly after this experiment, 160 channels of integrated pre-amplifier and amplifier electronics to outfit one 40 x 40 DSSD with dual (high and low) gain electronics were purchased.

At present, three experiments have been performed with the DSSD beta detection system and the new electronics. As a result of efficiency related problems, prior to these experiments, a ^{207}Bi source run was performed. ^{207}Bi is an electron and gamma ray emitter, thus by using this source the ADC gates for the Ge detectors could be properly set for an e^{-}-γ coincidence, a serious problem that may have effected the efficiency calculations for the present study. Using this new system, implant events have been characterized as predominately multiplicity one events and may be easily correlated with subsequent beta particles identified within the same pixel. In addition, by properly setting the gates on the ADC's for the Ge detectors, the ϵ_{β}*ϵ_{γ} efficiency has vastly improved.

Appendix A

Beta Efficiency Calculations

A.0.4 Experimental Efficiency for Exp. 97004

To determine the total beta efficiency for the rotating target wheel setup detailed in Sec. 3.2.1, the intensities of the gamma ray singles and the beta-delayed gamma ray peaks were compared. The prominent gamma ray peaks were fit to Gaussians using the program DAMM. The area of the background subtracted peaks in gamma ray singles, N_γ, and the beta-delayed gamma ray data, $N_{\gamma-\beta}$, were determined. The beta efficiency was extracted by taking the ratio of $N_{\gamma-\beta}/N_\gamma$,

$$\frac{N_{\gamma-\beta}}{N_\gamma} = \frac{I_\gamma \epsilon_\gamma \epsilon_\beta}{I_\gamma \epsilon_\gamma} \tag{A.1}$$

where I_γ is the intensity of the gamma ray transition, ϵ_γ is the peak gamma ray efficiency and ϵ_β is the beta efficiency.

The beta efficiency reported in Ref. [45,73] was 40.0(24)%. In an attempt to reproduce this measurement, the N_γ and $N_{\gamma-\beta}$ values for the prominent gamma ray transitions were extracted. Table A.1 provides a list of calculated N_γ, $N_{\gamma-\beta}$ and efficiencies. Taking the weighted average of these values, a total beta efficiency of 32.0(5)% has been determined, which is close, but does not match the quoted value. Any additional factors considered in the earlier beta efficiency calculation are unknown.

A.0.5 Simulated Beta Efficiency for Exp. 98020

In an attempt to simulate the beta efficiency for Exp. 98020, GEANT was utilized. To determine whether the simulation was working properly, the results were compared to

Table A.1: Calculated beta efficiency for Exp. 97004. The errors are listed in the parentheses for N_γ, $N_{\gamma-\beta}$ and ϵ_β.

E (keV)	N_γ	$N_{\gamma-\beta}$	ϵ_β (%)
143.0	2.90(5) x 10^4	6.08(58)	21.0(20)
156.0	2.54(4) x 10^4	8.42(65)	33.1(26)
175.0	4.01(160) x 10^3	2.39(44)	59.7(261)
193.0	7.33(184) x 10^3	3.49(48)	47.6(136)
410.0	9.02(31) x 10^3	2.46(9)	27.3(13)
432.0	1.78(4) x 10^4	6.85(12)	38.5(10)
450.0	1.24(3) x 10^4	5.10(11)	41.2(13)
596.0	3.54(12) x 10^4	8.94(24)	25.2(11)
620.0	5.75(82) x 10^3	1.06(11)	18.4(32)
628.0	6.27(83) x 10^3	2.06(13)	32.9(49)

the experimental beta efficiency for a ^{90}Sr source placed 26.7 cm upstream from the strip detector. The source was mounted at the center of a 7 cm x 7 cm, 1458 mg/cm^2 Al degrader. The chamber was placed under vacuum and data were collected for 30 minutes. Based on the certificate of calibration, the ^{90}Sr source was produced on March 1, 1997 with an activity of 41.0(1.3) kBq. As ^{90}Sr decays, a secular equilibrium is established with ^{90}Y, thus A(^{90}Sr) $\approx$ A(^{90}Y). At the time of the measurement, the calculated activity of ^{90}Sr was 36.8(1.2) kBq and a total of 1.41 x 10^8 beta particles were emitted by the source from ^{90}Sr and ^{90}Y combined. During this 30 minute measurement, 4.12(1) x 10^5 beta particles were observed in the strip detector. This value has been corrected for the computer dead time, however, the electronics dead time has not been considered. Taking this dead time correction into account, a lower limit experimental beta efficiency of 0.291(9)% was calculated at this source-to-detector distance.

A geometrical efficiency, $\epsilon_{geom}=\Omega/4\pi$, of 0.175% was calculated considering the solid angle of a rectangular detector [74],

$$\Omega = \arctan\left[\frac{(x2-xp)(y2-yp)}{zp\sqrt{(x2-xp)^2+(y2-yp)^2+zp^2}}\right] - \arctan\left[\frac{(-xp)(y2-yp)}{zp\sqrt{(-xp)^2+(y2-yp)^2+zp^2}}\right]$$

$$- \arctan\left[\frac{(x2 - xp)(-yp)}{zp\sqrt{(x2 - xp)^2 + (-yp)^2 + zp^2}}\right]$$
$$+ \arctan\left[\frac{(-xp)(-yp)}{zp\sqrt{(-xp)^2 + (-yp)^2 + zp^2}}\right] \qquad (A.2)$$

where xp, yp and zp represent the x, y and z coordinates (2 cm, 2 cm, 26.7 cm) of the source relative to the detector and x2 and y2 represent the horizontal and vertical dimensions of the strip detector (4 cm x 4 cm).

Based on the experimental total efficiency and the geometrical efficiency, an intrinsic efficiency of 166.3 % has been determined considering data for a point source. This efficiency is much larger than intuitively expected. The increase in the intrinsic efficiency has been attributed to beta particles scattering off the walls of the Al chamber and the Al degrader to which the source was mounted. The scattered beta particles may be directed back into the path of the DSSD, adding to the total beta efficiency. In this sense, the beta source may be thought of as a collimated source.

Using GEANT, the beta efficiency for the above geometry was simulated. A 985 μm, segmented Si strip detector was placed at a distance of 26.7 cm from a beta source. A 6.44 μm mylar window was placed in front and behind the source to mimic the 0.9 mg/cm^2 aluminized mylar covering and backing. A 0.254 mm layer of stainless steel was added to the backing to account for the disk the source was mounted upon. The 1458 mg/cm^2 Al holder has also been included within the simulation. Two separate simulations were performed, the first considering a beta particle with a maximum energy of 546 keV and a second with E_{max} = 2281 keV, the Q_β values for ^{90}Sr and ^{90}Y, respectively. A separate subroutine was written to generate a realistic beta energy spectrum, ranging from zero to Q_β. In addition, the thresholds for each of the front and back strips were read in using a separate FORTRAN call.

Considering the emission of three million ^{90}Sr and ^{90}Y beta particles, simulated beta efficiencies of 0.188(3)% and 0.318(3)%, respectively, were calculated. Thus, a total beta efficiency of 0.236(2)% was deduced from the GEANT simulation. Considering the simulated total beta efficiency and the geometrical efficiency calculated

above, an intrinsic efficiency of 134.9% was determined. This simulated intrinsic efficiency is within 82% of the value determined experimentally, indicating that the simulation is physically correct.

To calculate the intrinsic efficiency for 98020, the current simulation would need to be modified. During Exp. 98020, the secondary beam was defocussed to illuminate $\approx 2/3$ of the active area of the DSSD. Thus, the beta particles that were emitted from the DSSD were not localized to a single pixel. The true beta source was an extended source centered at $\text{strip}_x = 24$ and $\text{strip}_y = 24$ (see Fig. 3.7). To simulate an extended source, the current code would need to be modified to account for the distribution of the beam in the x-y plane.

A simple algorithm has been included in the code to vary the implantation depth and straggling of an ion within the DSSD. This algorithm allows the position of a beta particle to be varied in the z axis. However, at present, this routine has been commented out.

A.0.5.1 GEANT Program

The following is the GEANT program used to simulate experiment 98020. Three detector volumes have been defined in this program, DSSD, PIN2 and PIN3. For the simulation discussed above, PIN2 and PIN3 were not utilized, therefore they have been commented out. The definitions for the various materials incorporated within the experimental setup may be found in the dssd_mate subroutine. Careful consideration was taken for the maximum number of steps a particle would take in any given volume. The parameter dmaxms, which defines the maximum step size, was set to 1/3 the thickness of each of the defined volumes, in dssd_mate. In addition, the geometries and positions of each of the user defined volumes have been defined in the dssd_geom subroutine.

References to the beta source may be found in the dssd_kine subroutine. The position of the source is defined by the array vert(3), where vert(1) provides the x position, vert(2) the y and vert(3) the z. In the program listed below, the source has

been positioned 26.7 cm from the DSSD. This distance may be modified by adjusting vert(3).

```
*************************************************************
*                   dssd_geant.for
*************************************************************
*  dssd_imain
*************************************************************
*  This is the main code for running interactive GEANT
*  simulation runs.
*************************************************************
*  Special note:
*       !!!!!    GEANT UNITS ARE "cm." and "GeV"  !!!!!!
*************************************************************
        parameter (nwgean=5000000,nwpaw=5000000)
        common/PAWC/h(nwpaw)
        common/GCBANK/q(nwgean)

        call gpaw(nwgean,nwpaw)
        call HistOut
end

*************************************************************
*  dssd_init
*************************************************************
*  This is the main body code for initiating and nicely
*  ending GEANT simulation runs.
*************************************************************
*  Special notes:
*       To start type: progname [file1] [file2]
*         if both file1 and 2 are missing user.inp and
*   user.hbook are used if only file2 is missing,
*   file1-extension+.hbook is used
*************************************************************
subroutine uginit

* GEANT common blocks
        INCLUDE 'nscl_bnmr:[prisc.geant.beta.ginc]gcflag.ins'
* User defined common blocks
        INCLUDE 'nscl_bnmr:[prisc.geant.beta.uinc]uresol.ins'
INCLUDE 'nscl_bnmr:[prisc.geant.beta.uinc]ukine.ins'
        INCLUDE 'nscl_bnmr:[prisc.geant.beta.uinc]uoutput.ins'
        INCLUDE 'nscl_bnmr:[prisc.geant.beta.uinc]uedep.ins'

Integer NumInArgs,FileLen,Len2,x,y,counter
character*2 x2,y2
real thres_x(40),thres_y(40)
```

```
* read in values from command line to determine input and
* output data files
NumInArgs = iargc()
if( NumInArgs.eq.0 ) then
   FileIn = 'user.inp'
   FileOut = 'user.hbook'
else if ( NumInArgs.eq.1 ) then
   call getarg(1,FileIn)
   call white_out(FileIn,FileOut,FileLen)
   if (FileLen.eq.0) FileLen = len(FileOut)
   Len2 = index(fileout,'.')
   Len2 = min(FileLen+1,Len2)
   FileOut(Len2:) = '.hbook'
else
   call getarg(1,FileIn)
   call getarg(2,FileOut)
endif

write(*,*) 'The input file:',FileIn
write(*,*) 'The hbook file:',FileOut

* initialize GEANT variables

*--Presets labelled COMMON block variables to default values.
call GINIT

* read data cards

* STANDARD INPUT
open (5,file = FileIn, status = 'unknown')

* Reads in user defined variables from user.inp.
* CALL FFKEY('KEY',VAR(1),NVAR,'TYPE')
* Control values for event creation
CALL FFKEY('KINEOPT',KineOpt,1,'INTE')
CALL FFKEY('BETOPT',BetaOpt,1,'INTE')
CALL FFKEY('PARTICLE',Particle,1,'INTE')
CALL FFKEY('ENERGY',Energy,1,'REAL')
CALL FFKEY('THETA',ThetaMax,1,'REAL')
CALL FFKEY('PHI',PhiMax,1,'REAL')
CALL FFKEY('Z',Znumber,1,'INTE')
CALL FFKEY('AVER_DEPTH',avg,1,'INTE')
CALL FFKEY('STD',std,1,'REAL')
* Control values for output
CALL FFKEY('EVTPRT',evtprt,1,'INTE')
CALL FFKEY('OUTPUT',output,1,'INTE')
```

```
*--Reads a set of data cards with the FFREAD package.
        call gffgo

* check for crazy entries.  If problems, change them:
if (ThetaMax.gt.180) then
  write(*,*) 'Theta too large, set to 180'
  ThetaMax = 180
endif

* initialize data structures
call gzinit

* initialize drawing package
call gdinit

* DEFINE STANDARD PARTICLES (SEE [CONS300])
CALL ugmate

* define the geometrical set-up
call ugeom

* compute cross-sections and energy loss tables
call gphysi

* Initialize output histograms
call MakeHists

* Initialize user variables
        Begin = 1
EnP2 = 0.0
EnP3 = 0.0
        EnDs = 0.0
        eBeta = 0.0
betact = 0
CtP2 = 0
CtP3 = 0
CtDSSD = 0
EffP2 = 0.0
EffP3 = 0.0
EffDSSD = 0.0

* draw setup
call gsatt ('WRLD','SEEN',0)

* CALL GDRAW('VOLUME NAME',THETA,PHI,PSI,UO,VO,SU,SV)
* UO - u-coordinate on the screen of the volume origin.
```

```
*  V0 - v-coordinate on the screen of the volume origin.
* SU - scale factor for u-coordinate.
* SV - scale factor for v-coordinate.

call gdraw ('WRLD',30.,30.,0.,10.,10.,0.5,0.5)

*   Init. BetaMax if a beta particle distribution is desired
if (BetaOpt.eq.0) then
   if (Particle.eq.2.or.Particle.eq.3) then
     call FindMax(Energy,MaxBeta,Particle,Znumber)
   endif
endif

* Reads in threshold setting for individual strips, front and back.

Open(unit = 1,file ='back_thres.txt',status='old')
  do j = 1,40,1
    Read(1,*,end=77), thres_x(j)
  enddo
77 Continue
Close(1)
Open(unit = 2,file ='front_thres.txt',status='old')
  do j = 1,40,1
    Read(2,*,end=78), thres_y(j)
  enddo
78   Continue
Close(2)

* For a given pixel, will take the higher of the two thresholds
* x or y for the pixel threshold.  During analysis, we required
* a double-sided event to be a true implant and beta decay event.
* Threshold is stored in the thres_pixi array and is compared to
* the energy deposited in that pixel in dssd_out.

do y = 1,40,1
  do x = 1,40,1
    counter = x + 40*(y-1)
      if(thres_x(x).gt.thres_y(y))then
thres_pixi(counter) = thres_x(x)
c print *, 'thres ',counter,'=',thres_pixi(counter)
    else
thres_pixi(counter) = thres_y(y)
c print *, 'thres ',counter,'=',thres_pixi(counter)
    endif
  enddo
enddo
```

```
return
end
*************************************************************
*  white_out: See description below.
*************************************************************
* LIBRARY:      /usr/users/beene/lib/jblibf1.a
*************************************************************
*  This package is a set of fortran utility routines.
* -----------------------------------------------------------
*  Routines included:
* -----------------------------------------------------------
*   subroutine white_out(cin,cout,length)
*      Moves cin to cout deleting leading and trailing white
*      space (tab or space), and returns length of cout.
*      NO**Also puts a null at end of cout.**NO, NOT ANY MORE!!!
*      copied from utility01.f /pt

       subroutine white_out(cin,cout,length)
       implicit integer*4 (a-z)
       byte btab
       character *(*) cin, cout
       character *1 blank,tab
       data blank/' '/,btab/9/
       equivalence (tab,btab)
       i=1
       lench=len(cin)
       leno=len(cout)
       do while(cin(i:i).eq.blank.or.cin(i:i).eq.tab)
          i=i+1
          if(i.gt.lench)then
             length=0
             return
          endif
       enddo
       j=lench
       do while(cin(j:j).eq.blank.or.cin(j:j).eq.tab)
          j=j-1
          if(j.lt.0)then
             length=0
             return
          endif
       enddo
       length=j-i+1
       length=min(leno,length)
       cout(1:length)=cin(i:j)
       return
       end
```

```
************************************************************
*  MakeHists: Make output histograms (HBOOK type).
************************************************************
subroutine MakeHists

* GEANT common blocks
        INCLUDE 'nscl_bnmr:[prisc.geant.beta.ginc]gcflag.ins'
* User common blocks

* HBOOK1(id,'Hist title',#bins,low end energy, high end energy, 0. )

call HTITLE('From GEANT program  JP GEANT')
        call HBOOK1(1,'Energy PIN2',100,1.,11000.,0.)
        call HBOOK1(2,'Energy PIN3',100,1.,11000.,0.)
        call HBOOK1(3,'Energy DSSD',100,1.,11000.,0.)
        call HBOOK1(4,'Summed Energy',100,1.,11000.,0.)
call HBOOK1(5,'Total E(beta)',100,1.,11000.,0.)
        call HBOOK1(6,'PIN2 [e] vs. E',100,1.,11000.,0.)
        call HBOOK1(7,'PIN3 [e] vs. E',100,1.,11000.,0.)
        call HBOOK1(8,'DSSD [e] vs. E',100,1.,11000.,0.)
* To determine eff. of silicon detectors, need to count how
* many betas impinged on the detectors.
call HCOPY(5,11,'E(beta) when [b] detected in PIN2')
call HCOPY(5,12,'E(beta) when [b] detected in PIN3')
call HCOPY(5,13,'E(beta) when [b] detected in DSSD')
return
end
************************************************************
*  dssd_mate
************************************************************
*  The materials and particles are defined here.
************************************************************
      SUBROUTINE UGMATE

* GEANT common blocks
        INCLUDE 'nscl_bnmr:[prisc.geant.beta.ginc]gcbank.ins'
        INCLUDE 'nscl_bnmr:[prisc.geant.beta.ginc]gcflag.ins'
        INCLUDE 'nscl_bnmr:[prisc.geant.beta.ginc]gctmed.ins'
        INCLUDE 'nscl_bnmr:[prisc.geant.beta.ginc]gctrak.ins'

* USER common blocks
        INCLUDE 'nscl_bnmr:[prisc.geant.beta.uinc]umaterials.ins'

*   statements for the various material parameters
        real AGE,ZGE,DGE,RGE,ABGE
        real ASI,ZSI,DSI,RSI,ABSI
real AMYL(3),ZMYL(3),WMYL(3),DMYL
```

```
real ASTE(3),ZSTE(3),WSTE(3),DSTE

*   Ge compound parameters
      DATA AGE/72.59/ !Atomic mass
      DATA ZGE/32.0/            !Atomic number
      DATA DGE/5.323/           !Density (g/cm-3)
      DATA RGE/2.3017/          !Radiation length (cm)
      DATA ABGE/30.3/           !Absorption length (cm)

*   Si compound parameters
      DATA ASI/28.09/           !Atomic mass
      DATA ZSI/14.0/            !Atomic number
      DATA DSI/2.33/            !Density (g/cm-3)
      DATA RSI/9.351/           !Radiation length (cm)
      DATA ABSI/53.45/          !Absorption length (cm)

* store standard particle definitions (see CONS[300])
call gpart
* store standard material definitions (see CONS[100])
call gmate

* user material number
matVac = 16
matAir = 15
matAl  = 9
matGe  = 20
matSi  = 21
        matpla = 25
        matSt = 30

*       define user materials and compounds

* CALL GSMATE(IMATE,NAMATE,A,Z,DENS,RADL,ABSL,UBUF,NWBUF)
* IMATE - user material number.
* NAMATE - material name.
* A - atomic weight.
* Z - atomic number.
*  DENS - density (g/cm^3).
*  RADL - radiation length.
* ABSL - absorption length.
* UBUF - array of NWBUF additional user parameters.

       call gsmate(matGe,'ge',age,zge,dge,rge,abge,0.0,0)
       call gsmate(matSi,'si',asi,zsi,dsi,rsi,absi,0.0,0)

* Mylar is a plastic, which is composed of a mixture of C, H, and O.
```

```
* atomic masses of the components
data AMYL/12.011,1.00794,15.9994/
* nuclear charges of the components
data ZMYL/6.0,1.0,8.0/
* number of atoms of each component
data WMYL/10.0,8.0,4.0/
* density
data DMYL/1.397/

* Stainless steel is an alloy of Cr, Fe and Ni.

* atomic masses of the components
data ASTE/51.9961,55.847,58.6934/
* nuclear charges of the components
data ZSTE/24.0,26.0,28.0/
* number of atoms of each component
data WSTE/8.0,74.0,18.0/
* density
data DSTE/8.0/

*--Definition of mixtures and compounds.
* CALL GSMIXT(IMATE,NAMATE,A,Z,DENS,NLMAT,WMAT)
* IMATE - user material number.
* NAMATE - material name.
* A - array of atomic weights.
* Z - array of atomic numbers.
* DENS - density (g/cm^3).
*  NLMAT - number of different components in the mixture.
* If NLMAT > 0, then WMAT contains the proportion by weights
* of each basic material in the mixture.
* If NLMAT < 0, then WMAT contains the number of atoms of a
* given kind in the compound.

call gsmixt(matpla,'mylar',AMYL,ZMYL,DMYL,-3,WMYL)
call gsmixt(matSt,'steel',ASTE,ZSTE,DSTE,-3,WSTE)

* print out material parameters
call gpmate(0)

*  set up user media & tracking parameters

* tracking medium number.
medVac = 1
medAir = 2
medAl  = 3
medGe  = 4
medSi  = 5
```

```
medpla = 6
        medSt  = 7

*--Tracking medium parameters. Default values used when values
* of < 1 are entered.
      dmaxms = -1. !Maximum step size permitted (cm)
      deemax = -1. !Maximum Fractional E loss in one step
      epsil = 1e-14 !Boundary crossing precision (cm)
      stmin = -1.    !Minimum step size (cm)

* CALL GSTMED(ITMED,NATMED,NMAT,ISVOL,IFIELD,FIELDM,
* TMAXFD,DMAXMS,DEEMAX,EPSIL,STMIN,UBUF,NWBUF)
* ITMED - tracking medium number.
*  NATMED - tracking medium name.
*  NMAT - material number corresponding to ITMED.
* ISVOL - =0 if not a sensitive volume (not a detector).
* IFIELD = 0 no magnetic field.
*        other options detailed in CONS200
* FIELDM - maximum field value (kG)
* TMAXFD - maximum angle due to field permitted in one step.
* DMAXMS - maximum step size.
* DEEMAX - maximum fractional energy loss in one step.
* EPSIL - tracking precision.
* STMIN - minimum step size.
* UBUF - array of NWBUF additional parameters.

      call gstmed(medVac,'vacuum$',matVac,0,0,0.0,0.0,dmaxms,
     +     deemax,epsil,stmin,0,0)
      call gstmed(medAir,'air$',matAir,0,0,0.0,0.0,dmaxms,
     +     deemax,epsil,stmin,0,0)

* dmaxms for detectors and degrading material calculated as 1/3 of
* the thickness of the given medium.

      call gstmed(medAl,'al$',matAl,0,0,0.0,0.0,0.08,
     +     deemax,epsil,stmin,0,0)
      call gstmed(medGe,'ge$',matGe,1,0,0.0,0.0,dmaxms,
     +     deemax,epsil,stmin,0,0)
      call gstmed(medSi,'si$',matSi,1,0,0.0,0.0,0.02,
     $     0.8,epsil,stmin,0,0)
      call gstmed(medpla,'mylar$',matpla,0,0,0.0,0.0,2e-4,
     +    0.8,epsil,stmin,0,0)
      call gstmed(medSt,'steel$',matSt,0,0,0.0,0.0,0.005,
     +    0.8,epsil,stmin,0,0)

* print the tracking medium parameters
call gptmed(0)
```

```
      RETURN
      END
*************************************************************
*  dssd_geom
*************************************************************
*  Detector types and geometries are defined here.
*************************************************************
      SUBROUTINE UGEOM

* GEANT common blocks
        INCLUDE 'nscl_bnmr:[prisc.geant.beta.ginc]gcbank.ins'
        INCLUDE 'nscl_bnmr:[prisc.geant.beta.ginc]gcflag.ins'
        INCLUDE 'nscl_bnmr:[prisc.geant.beta.ginc]gctmed.ins'
* USER defined common blocks
        INCLUDE 'nscl_bnmr:[prisc.geant.beta.uinc]umaterials.ins'

integer testset,testdet,slot,strip
real    dssdpos
character eloss*4,num*4,name*4

* A few of the overall parameters are defined here.
real WRLD(3)
real FLGE(3), CHMB(5), VACC(5), VAC2(3), BEAM(3)
real PLAS(3), RING(3), DISK(3), DEGR(3)
real PIN2(3), PIN3(3), DSSD(3), PIXI(3)

*--Definition of volume shape.  Here are several shapes that may
* be defined and the information necessary to create such a volume.
* 'BOX ' - the x, y and z half lengths must be provided.
* 'TUBE' - inner radius, outer radius and half length in z.
* 'CONE' - half length in z, inner and outer radii at low z
*    and inner and outer radii at high z limit.


* Outside world, 'BOX '.
        DATA WRLD/70.,70.,70./
* Vacuum chamber, 'TUBE'.
DATA FLGE/0.0, 8.35, 0.65/
DATA CHMB/12.15, 5.0, 5.35, 8.0, 8.35/
DATA VACC/12.15, 0.0, 5.0, 0.0, 8.0/
* Source holder, 'TUBE'.
DATA PLAS/0.0, 1.19, 3.22E-4/
DATA RING/1.19, 1.27, 0.159/
DATA DISK/0.0, 1.19, 0.0127/
* The source was mounted on an Al degrader, 'BOX '.
        DATA DEGR/3.5, 3.5, 0.27/
```

```
* Beam line and vacuum, 'TUBE'.
DATA BEAM/5.0, 5.35, 12.15/
DATA VAC2/0.0, 5.0, 12.15/
* Create a detector, 'BOX '.
DATA PIN2/2.5, 2.5, 0.02515/
   DATA PIN3/2.5, 2.5, 0.01545/
DATA DSSD/2.0, 2.0, 0.04925/
DATA PIXI/0.05, 0.05, 0.04925/

*--Creates mother volume or master system
* CALL GSVOLU(NAME,SHAPE,NMED,PAR,NPAR,IVOLU*)
*       NAME - unique four character name.
*    SHAPE - 4 character name of system shape, see GEOM050.
* NMED - tracking medium number.
* PAR - array containing shape parameter.
* NPAR - number of such parameters.
* IVOLU - number returned by subroutine as system volume number.

       CALL GSVOLU('WRLD','BOX ',medAir,WRLD,3,ibox)
CALL GSVOLU('FLGE','TUBE',medAl,FLGE,3,ibox)
CALL GSVOLU('CHMB','CONE',medAl,CHMB,5,ibox)
CALL GSVOLU('VACC','CONE',medVac,VACC,5,ibox)
CALL GSVOLU('VAC2','TUBE',medVac,VAC2,3,ibox)
CALL GSVOLU('BEAM','TUBE',medAl,BEAM,3,ibox)
c Call gsvolu('PIN2','BOX ',medSi,PIN2,3,ibox)
c call gsvolu('PIN3','BOX ',medSi,PIN3,3,ibox)
call gsvolu('DSSD','BOX ',medVac,DSSD,3,ibox)
CALL GSVOLU('PLAS','TUBE',medpla,PLAS,3,ibox)
CALL GSVOLU('RING','TUBE',medAl,RING,3,ibox)
CALL GSVOLU('DISK','TUBE',medSt,DISK,3,ibox)
        CALL GSVOLU('DEGR','BOX ',medAl,DEGR,3,ibox)

* Creating the individual pixel volumes for DSSD.
do i = 1, 1600, 1
* Converts integer value to character notation, 0001 - 1600.
          encode(4,17,num) i
c   print *, 'num = ',num
  call gsvolu(num,'BOX ',medSi,PIXI,3,ibox)
enddo

*--Prints the volume parameters.
c        call gpvolu(0)

*--Creates a rotation matrix
* CALL GSROTM(IROT,THETA1,PHI1,THETA2,PHI2,THETA3,PHI3)
* IROT - rotation matrix number.
* THETA1 - polar angle for axis x'.
```

```
* PHI1 - azimuthal angle for axis x'.
* THETA2 - polar angle for axis y'.
* PHI2 - azimuthal angle for axis y'.
* THETA3 - polar angle for axis z'.
* PHI3 - azimuthal angle for axis z'.

* PIN2 is orientated such that the distance from the top of
* the PIN to the flange is 8.2 cm and the distance from the
* bottom of the PIN to the flange is 8.7 cm.  Thus, there
* is a 4.1 degree angle with respect to theta_z.
CALL GSROTM(1,90.0,0.0,85.9,90.0,4.1,270.0)

*--Positioning volume inside its mother.
* CALL GSPOS(NAME,NR,MOTHER,X,Y,Z,IROT,KONLY)
* NAME - four character volume name.
*  NR - copy number of volume.
* MOTHER - four character name of volume in which this
*   volume is placed.
* X,Y,Z - position of volume in reference to the mother
*   volume. Position is defined as the center of volume
*   relative to the center of the mother volume.
* IROT - rotation matrix number describing orientation
*   of volume relative to the mother volume.
* KONLY - flag indicating if a point found in this volume
*   may also be in other volumes.

* VACC and WRLD have been shifted such that they are centered
* at the position of the DSSD.

        dssdpos = 5.83075

CALL GSPOS('VACC',1,'WRLD',0.0,0.0,-dssdpos,0,'ONLY')
CALL GSPOS('CHMB',1,'WRLD',0.0,0.0,-dssdpos,0,'ONLY')
CALL GSPOS('FLGE',1,'WRLD',0.0,0.0,12.8-dssdpos,0,'ONLY')
CALL GSPOS('VAC2',1,'WRLD',0.0,0.0,-24.3-dssdpos,0,'ONLY')
CALL GSPOS('BEAM',1,'WRLD',0.0,0.0,-24.3-dssdpos,0,'ONLY')
* Distance of detectors relative to center of chamber.
c CALL GSPOS('PIN2',1,'VACC',0.0,0.0,3.72487,1,'ONLY')
CALL GSPOS('DSSD',1,'VACC',0.0,0.0,dssdpos,0,'ONLY')
c CALL GSPOS('PIN3',1,'VACC',0.0,0.0,7.63455,0,'ONLY')
* Source distance for 33Mg run.  Note position is relative to VAC2.
CALL GSPOS('RING',1,'VAC2',0.0,0.0,24.3-20.9,0,'ONLY')
CALL GSPOS('DISK',1,'VAC2',0.0,0.0,24.3-20.875988,0,'ONLY')
CALL GSPOS('PLAS',1,'VAC2',0.0,0.0,24.3-20.862966,0,'ONLY')
CALL GSPOS('PLAS',2,'VAC2',0.0,0.0,24.3-20.862322,0,'ONLY')
        CALL GSPOS('DEGR',1,'VAC2',0.0,0.0,24.3-21.32,0,'ONLY')
* Source distance for 33Al run.  Note position is relative to VACC.
```

```
c CALL GSPOS('RING',1,'VACC',0.0,0.0,-7.309,0,'ONLY')
c CALL GSPOS('DISK',1,'VACC',0.0,0.0,-7.284988,0,'ONLY')
c CALL GSPOS('PLAS',1,'VACC',0.0,0.0,-7.271966,0,'ONLY')
c CALL GSPOS('PLAS',2,'VACC',0.0,0.0,-7.271322,0,'ONLY')

* Positioning individual pixels within DSSD mother volume.
do y = 1,40, 1
  do x= 1,40,1
* Each pixel will be labelled 0001 - 1600.
    slot = x+40*(y-1)
* Converts integer value to character notation, 0001-1600.
    encode(4,17,name) slot
c     print *, name
* Positioning individual pixels starting at lower lefthand corner.
  call gspos(name,1,'DSSD',(-2.05+0.1*x),
     1 (-2.05+0.1*y),0.0,0,'ONLY')
  enddo
enddo

*--Declaring active detector volumes.
*  CALL GSDETV(CHSET,CHDET,IDTYP,NWHI,NWDI,ISET,IDET)
* CHSET - four character set identifier
*  CHDET - four character detector identifier, has to be the
*   name of an existing volume
* IDTYP - detector type.
* NWHI - initial size of HITS banks.
* NWDI - initial size of DIGI banks.
* ISET - position of set in back JSET.
* IDET - position of detector in back JS=LQ(JSET-ISET)

* Declaring PIN2 an active detector volume.
c CALL GSDETV('DEP2','PIN2',medSi,100,100,testset,testdet)

* Declaring individual pixel volumes as active detectors.
do j = 1, 1600, 1
* Converts integer value to character notation, 0001 - 1600.
    encode(4,17,name) j
c     print *,name
* Active detector pixels labelled from 1001 - 2600.
    encode(4,17,eloss) j+1000
c     print *,eloss
  CALL GSDETV(eloss,name,medSi,100,100,testset,testdet)
enddo

* Declaring PIN3 an active detector volume.
c CALL GSDETV('DEP3','PIN3',medSi,100,100,testset,testdet)
```

```
17 format(i4.4)

*--This routine should be called after all volumes and positions
* have been defined.
       CALL GGCLOS

return
end
*************************************************************
*  dssd_kine
*************************************************************
*  Emission of particles with defined E and angle.
*************************************************************
subroutine gukine

* GEANT common blocks
        INCLUDE 'nscl_bnmr:[prisc.geant.beta.ginc]gcflag.ins'
        INCLUDE 'nscl_bnmr:[prisc.geant.beta.ginc]gconst.ins'
* User common blocks
INCLUDE 'nscl_bnmr:[prisc.geant.beta.uinc]ukine.ins'
        INCLUDE 'nscl_bnmr:[prisc.geant.beta.uinc]uedep.ins'

real vert(3),RNDM(2),plab(3),dssd_z
*
real eTheta,ePhi,eEnergy
integer iloop,counter,evnts,tab_evnts
character*1 respon

* Determine where the particle will be emitted

* IEVENT is a trigger counter.  It counts from 1 to NEVENT
* (total particles emitted).  Counter is a variable used
* to count from 1 to inputted trigger.  This variable needs
* to be initialized the first time through the program.

c if(IEVENT.eq.1) counter = 1
c if(counter.eq.1) then
c respon = 'y'

* EVNTS is the total number of particles in a given trigger,
* whereas tab_evnts is an evnts counter.

c               evnts = NEVENT - tab_evnts
c endif

* Position of the source.
vert(1) = 0.0 !x position
```

```
vert(2) = 0.0   !y position

* Considering a gaussian distribution of implantation depth.
* Sigma and avg are read in from user.inp file.
c Print *,'I am bombing here I'
c call Gaussian(std,avg,evnts,dssd_z,respon)
c vert(3) = dssd_z !z position

* Source distance for 33Mg run.
vert(3) = -26.693394 !z position
* Source distance for 33Al run.
c vert(3) = -13.102394 !z position
c Print *,'x=',vert(1),'y=',vert(2),'z=',vert(3)
c counter = counter + 1
c if(counter.eq.(evnts+1)) then
c counter = 1
c                tab_evnts = evnts + tab_evnts
c endif
stepct = 0

*--Storing/retrieving vertex and track parameters.
* CALL GSVERT(VERT,NTBEAM,NTTARG,UBUF,NUBUF,NVTX)
* VERT - array of (x,y,z) position of the vertex.
* NTBEAM - beam track number origin of vertex, =0 if
*   none exists.
* NTTARG - target track number origin of vertex.
* UBUF - user array of NUBUF floating point numbers.
* NVTX - new vertex number.

call gsvert(vert,0,0,0,0,Nvert)

if(Nvert .eq. 0) then
  write(6,1000)
  stop
endif
1000 format(' error in gukine calling gsvert')

* Prints vertex parameters.
c call gpvert(0)

* Prints initial track parameters.
c call gpkine(0)

* Determine the angle of the emitted event
if (KineOpt.eq.0) then
* emit 4pi
  Call GRNDM(RNDM,2)
```

```
  eTheta=ACOS(-1. + 2. * RNDM(1))
  ePhi=TWOPI*RNDM(2)
else if (KineOpt.eq.1) then
* emit in cone of <ThetaMax
  Call GRNDM(RNDM,2)
  eTheta=ACOS(-1. + 0.01111111*ThetaMax*RNDM(1))
  ePhi=TWOPI*RNDM(2)
else
* emit at fixed angle
  eTheta = ThetaMax*0.017453293
  ePhi   = PhiMax*0.017453293
endif

* Calculate modified energies here.
if (Particle.eq.2.or.Particle.eq.3) then
  if (BetaOpt.eq.0) then
    eEnergy = BetaMom(Energy,MaxBeta,Particle,Znumber)
  else
    eEnergy = Energy
  endif
else
  eEnergy = Energy
endif

eBeta = eEnergy
c print *,eBeta

* Convert Energy and angles into x, y and z momenta
plab(1)=0.000001*eEnergy*SIN(eTheta)*COS(ePhi)
plab(2)=0.000001*eEnergy*SIN(eTheta)*SIN(ePhi)
plab(3)=0.000001*eEnergy*COS(eTheta)

* Create the event
c write(*,*) 'Particle =',Particle
c write(*,*) 'eEnergy =',eEnergy
c write(*,*) 'eTheta =',eTheta
c write(*,*) 'ePhi =',ePhi

* CALL GSKINE(PLAB,IPART,NV,UBUF,NUBUF,NT)
* PLAB - components of momentum.
* IPART - type of particle.
* NV - vertex number origin of track.
* UBUF - array of NUBUF floating point user parameters.
* NT - track number.

CALL GSKINE(plab,Particle,Nvert,0,0,NT)
```

```
return
end
*************************************************************
*  FINDMAX: This subroutine determines the maximum value of
*    the beta energy function, which is necessary for the
*    beta energy simulation.
*************************************************************
        subroutine FindMax(BetaQ,BetaMax,particle,Z)

        real BetaQ,BetaMax
        real rtemp,OldTestVal,TestVal
        integer iloop,particle,Z

        rtemp=1.0
        iloop=0
        OldTestVal = BetaEnergy(betaQ,rtemp,1.0,particle,Z)
        do while (iloop.ne.1)
          rtemp = rtemp + 0.00001*betaQ
          TestVal = BetaEnergy(betaQ,rtemp,1.0,particle,Z)
          if (TestVal.lt.OldTestVal) then
            iloop=1
            TestVal = OldTestVal
          else if (rtemp.gt.betaQ) then
            iloop=1
            write(*,*) 'Improper initialization of BetaMax'
          endif
          OldTestVal = TestVal
        enddo
        BetaMax = 1/TestVal

        return
end
*************************************************************
*  BETAMOM (function): This subroutine determines the beta
*    Energy and emits a Beta Particle
*
*  This is a basic monte carlo routine that samples a simulated
*  beta spectrum (defined by BetaEnergy) to randomly determine
*  the emitted beta energy.
*
*  The accepted beta energy is in variable BetaEner and in units
*  of MeV!
*************************************************************
        real function BetaMom(BetaQ,BetaMax,particle,Z)

        real BetaQ,BetaMax,BetaEner,NTe
        real RNDM(2)
```

```
        integer particle,iloop,Z

        iloop = 0
        do while (iloop.ne.1)
          CALL GRNDM(RNDM,2)
          BetaEner = BetaQ*RNDM(1)
          NTe = BetaEnergy(BetaQ,BetaEner,BetaMax,particle,Z)
          if ( RNDM(2).le.NTe ) then
            iloop = 1
          endif
        enddo

        betaMom = sqrt(BetaEner*BetaEner + 2*BetaEner*510.99906)

        return
end
*************************************************************
* BETAENERGY (function):  This function is used to simulate
*   the energy distribution of beta decays.
*
* Note:  This is Eq. 9.25 from "Introductory Nuclear Physics"
*   by Krane and corrected with the fermi correction function
*   F(Z,E)
*
* Because the function becomes too large when the values are
*  in keV, we use them in MeV.
*************************************************************
        real function BetaEnergy(BetaQ,Test,MaxFactor,particle,Z)

        integer particle,Z
        real BetaQ,Test,Q,Te,MaxFactor,nom,denom

        Te=Test*0.001
        Q=BetaQ*0.001

        if (particle.eq.3) then
           nom = MaxFactor*Z*(Q-Te)*(Q-Te)*(Te+0.51099906)
     +           *(Te+0.51099906)
           denom = 1-exp(-2*3.1415*Z*(Te+0.51099906)/
     +     (137*sqrt(Te*Te+2*Te*0.51099906)))
           BetaEnergy=nom/denom
        else if (particle.eq.2) then
           if (Te.lt.0.003) then
              BetaEnergy=0.
           else
              nom = MaxFactor*Z*(Q-Te)*(Q-Te)*(Te+0.51099906)
     +              *(Te+0.51099906)
```

```
            denom = 1-exp(2*3.1415*Z*(Te+0.51099906)/
     +      (137*sqrt(Te*Te+2*Te*0.51099906)))
            BetaEnergy=nom/(-denom)
         end if
      else
         type*,'particle should be 2 or 3'
      end if

return
      end
*************************************************************
Subroutine Gaussian(sig,aver,totevt,z,resp)

      Real W_mod(986),Prob(986),W(986),Tot_Prob,z,y,sig
integer Weight(986),depth,hit(986),aver,totevt,fwhm
logical first
character*1 resp
parameter (pi = 3.141592654)

c print *,'gaussian subroutine'
* Initialize parameters.
if(resp.eq.'y') then
do j = 1,985,1
Prob(j) = 0.0
W_mod(j) = 0.0
W(j) = 0.0
      Weight(j) = 0
hit(j) = 0
W_mod(j) = 0.0
enddo
  Tot_Prob = 0.0
depth = 0
    z = 0.0
y = 0.0
               resp = 'n'

* Probability that ion implanted z um within a 985 um DSSD.
* Sig = FWHM/2.354.  See equation 3-30 and 4-12 in Krane's
* "Radiation Detection and Measurement."

c Print *,'I am bombing here II'
c fwhm = nint(sig*2.354)
do j=1,985,1
Prob(j) = ((2.0*pi*(sig)**2)**(-0.5))*Exp(-((j-
     1   aver)**2.0)/(2.0*(sig)**2))
               Tot_Prob = Tot_Prob + Prob(j)
enddo
```

```
c Print *,'I am bombing here III'
do j=1,985,1
  Prob(j) = Prob(j)/Tot_Prob   !Normalized Prob.
W(j) = Prob(j)*totevt      !Weight
* When triggering 1 - 6 beta events, calculated probabilities
* were all below acceptable limits.  Needed to artificially
* adjust this to prevent the program from getting trapped in
* this section.

if(totevt.ge.1.and.totevt.le.6)then
W(j) = W(j)*6
endif
W_mod(j) = AMOD(W(j),1.0)
if(W(j).ge.0.2.and.W(j).lt.0.5) then
W(j) = 0.5
endif
weight(j) = nint(W(j))
if(weight(j).ge.1) then
Print *,j
endif
enddo
endif

* Determine the number of times an implant will occur at z.
x = 5

20 Call Random(x)
depth = nint(985.0*x)
if(weight(depth).ge.1) then
Weight(depth) = Weight(depth) - 1
else
goto 20
endif
y = real(depth)
c PRINT *,Y
y = y/10000.0
z =  -0.04925 + y  !penetration w/in DSSD
c Print *,z
return
end
*************************************************************
      Subroutine Random(Rannum)

Integer N, Const1
Real Rannum, Const2
Parameter (Const1 = 2147483647, Const2 = 1./Const1)
Save
```

```
Data N /0/

If(N.eq.0) N = Int(Rannum)
N = N * 65539
If(N.lt.0) N = (N + 1) + Const1
Rannum = N * Const2
RETURN
end

* The subroutine Random has been taken from "FORTRAN77 for
* Engineers and Scientists" by Larry Nyhoff and Sanford Leestma,
* page 420.  The values Const1 and Const2 have been arrived at
* by using the following equations 2**M - 1 and 1/(2**M -1),
* respectively.  M respresents the number of
* bit memory words of the computer, in this case M = 32.
*************************************************************
*  dssd_step
*************************************************************
*  Step size and energy loss is determined here.
*************************************************************
subroutine GUSTEP
*
* GEANT common blocks
        INCLUDE 'nscl_bnmr:[prisc.geant.beta.ginc]gcsets.ins'
        INCLUDE 'nscl_bnmr:[prisc.geant.beta.ginc]gctrak.ins'
        INCLUDE 'nscl_bnmr:[prisc.geant.beta.ginc]gckine.ins'
        INCLUDE 'nscl_bnmr:[prisc.geant.beta.ginc]gcflag.ins'
        INCLUDE 'nscl_bnmr:[prisc.geant.beta.ginc]gconst.ins'
        INCLUDE 'nscl_bnmr:[prisc.geant.beta.ginc]gcvolu.ins'
        INCLUDE 'nscl_bnmr:[prisc.geant.beta.ginc]gctmed.ins'
* User common blocks
        INCLUDE 'nscl_bnmr:[prisc.geant.beta.uinc]uedep.ins'

character set*4,det*4
integer  name,eloss

* store secondary particles
call gsking(0)

*--Prints the tracking and physics parameters after the current
* step.
c call gpcxyz

* if (ISWIT(1).eq.1) then
*--Stores current space point.
   call gsxyz
* endif
```

```
c write(*,*) '##############################################'
c write(*,*) 'IPART=',ipart,' NSTEP=',nstep,' ISTAK=',istak
c write(*,*) ' X=',vect(1),' Y=',vect(2),' Z=',vect(3)
c write(*,*) 'NMEC=',nmec
c do iiii = 1,nmec
c    write(*,1492) namec(lmec(iiii)),lmec(iiii)
1492    format(5x,A4,i10)
c enddo
c write(*,*) 'destep=',destep
c write(*,*) 'istop=',istop
c write(*,*) 'kcase=',kcase,' ngkine=',ngkine
c write(*,*) 'ihset=',ihset
c write(*,*) 'ihdet=',ihdet
c do 70 j=1,42,1
c   write(*,*) ' numbv(',j,') ',numbv(j)
c70      continue
c write(*,*) 'The total number of elements in numbv is ',nvname


* IHSET is an integer.  Comparing IHSET to the integer value of 'DEP2'.
c if (IHSET.eq.'DEP2') then
* IHDET is an integer.  Comparing IHDET to the integer value of 'PIN2'.
c   if (IHDET.eq.'PIN2') then
c     write(*,*) 'Energy deposited'
* Multiply destep by 10^6 so that energy is in terms of keV.
c     EnP2 = EnP2 + destep*1000000
c     write(*,*) 'EnP2,destep =',EnP2,destep
c   endif
c endif

c if (IHSET.eq.'DEP3') then
c   if (IHDET.eq.'PIN3') then
c     write(*,*) 'Energy deposited'
c     EnP3 = EnP3 + destep*1000000
c     write(*,*) 'EnP3,destep =',EnP3,destep
c   endif
c endif

* If active detector volume isn't DEP2 or DEP3, then...
if(IHSET.gt.0.and.IHSET.ne.'DEP2'.and.IHSET.ne.'DEP3') then
* Converts the integer IHSET to its internal character form.
  encode(4,17,set) IHSET
c   print *, 'set =',set
* Converts the character set to the equivalent integer.
  decode(4,21,set) eloss
c   print *, 'eloss =',eloss
```

```
* If not within PIN2 or PIN3, then...
  if(IHDET.gt.0.and.IHDET.ne.'PIN2'.and.IHDET.ne.'PIN3')then
* Converts the integer IHSET to its internal character form.
    encode(4,17,det) IHDET
* Converts the character set to the equivalent integer.
    decode(4,21,det) name
c            print *, 'IHDET',name
c     write(*,*) 'Energy deposited'
    Ener(name) = Ener(name) + destep*1000000
c     write(*,*) 'En ',name,' destep =',ener(name),destep
         endif
endif

if (NSTEP.eq.oldSTEP) then
  return
endif

oldSTEP = NSTEP

17 format(A4)
21   format(i4.4)
return
end
*************************************************************
*  dssd_out
*************************************************************
*  The output of tracking information is performed here.
*************************************************************
subroutine GUOUT

* GEANT common blocks
        INCLUDE 'nscl_bnmr:[prisc.geant.beta.ginc]gcflag.ins'
        INCLUDE 'nscl_bnmr:[prisc.geant.beta.ginc]gctmed.ins'
* User common blocks
        INCLUDE 'nscl_bnmr:[prisc.geant.beta.uinc]uedep.ins'
        INCLUDE 'nscl_bnmr:[prisc.geant.beta.uinc]uresol.ins'
        INCLUDE 'nscl_bnmr:[prisc.geant.beta.uinc]uoutput.ins'
INCLUDE 'nscl_bnmr:[prisc.geant.beta.uinc]ukine.ins'

        real Sigma
        logical thres_DS
integer  mult_DSSD

* initialize threshold
thres_DS = .false.

* initialize multiplicity
```

```
mult_DSSD = 0

* draw the particle tracks
c if (ISWIT(1).eq.1) then
  call gdxyz(0)
c endif

* Prints particle name and track.
c call gdpart(0,11,0.25)

* Draws hit points in sensitive detectors.
c call gdhits(0,0,0,0,0.25)

* Fill Histogram
*   HFILL( id, xValue(REAL), yValue(REAL), Weight )
CALL HFILL(1,EnP2,0,1.0)
CALL HFILL(2,EnP3,0,1.0)

*  Check threshold on each of the pixels on the strip detector.
  do j = 1,1600,1
  if(ener(j).gt.thres_pixi(j))then
    thres_DS = .true.
    EnDs = ener(j) + EnDs
    mult_DSSD = mult_DSSD + 1
          endif
enddo

if(Thres_DS.eq..true.) then
  CALL HFILL(3,EnDs,0,1.0)
CALL HFILL(4,EnP2+EnP3+EnDs,0,1.0)
endif

CALL HFILL(5,eBeta,0,1.0)

* Checking beta efficiency for PIN2.
c if(EnP2.gt.0.and.Thres_DS.eq..true.) then
c CALL HFILL(11,eBeta,0,1.0)
c CtP2 = CtP2 + 1
c EffP2 = real(CtP2)/real(IDEVT)
c ErrP2 = EffP2*Sqrt((1.0/real(CtP2))+(1.0/
c     1 real(IDEVT)))
c print *, 'EffP2',EffP2,'+/-',ErrP2

* CALL HOPERA(ID1,CHOPER,ID2,ID3,C1,C2)
* ID3 = C1*ID1 (OPERATION) C2*ID2
* ID1,ID2 operand histogram identifiers
* CHOPER identifies the operation, +,-,*,/ along will the
```

```
* computed errors
*    'B' computes binomial errors
*    'E' computes errors on resulting hist. assuming ID1
*       and ID2 are indep
* ID3 identifier for the hist containing operation
* C1,C2 multiplicative constants

c CALL HOPERA(11,'/E',5,6,1.0,1.0)
c        endif

* Checking beta efficiency for PIN3.
if(EnP3.gt.0.and.Thres_DS.eq..true.)then
CALL HFILL(12,eBeta,0,1.0)
CtP3 = CtP3 + 1
EffP3 = real(CtP3)/real(IDEVT)
ErrP3 = EffP3*Sqrt((1.0/real(CtP3))+(1.0/
     1 real(IDEVT)))
c print *, 'EffP3',EffP3,'+/-',ErrP3
CALL HOPERA(12,'/E',5,7,1.0,1.0)
        endif

* Checking beta efficiency for DSSD.
c if(Thres_DS.eq..true..and.mult_DSSD.eq.1) then
if(Thres_DS.eq..true.) then
c print *,'Above threshold'
CALL HFILL(13,eBeta,0,1.0)
CtDSSD = CtDSSD + 1
EffDSSD = real(CtDSSD)/real(IDEVT)
ErrDSSD = EffDSSD*Sqrt((1.0/real(CtDSSD))+
     1 (1.0/real(IDEVT)))
  CALL HOPERA(13,'/E',5,8,1.0,1.0)
        endif

EnP2 = 0.0
EnP3 = 0.0
EnDs = 0.0
do j = 1,1600,1
  ener(j) = 0.0
enddo

* don't write spectra until number of events is a factor of
* 'output'
IF (MOD(IDEVT,output).EQ.0) then
  CALL HistOut
        endif
c print *,'stuck in jp_outii'
```

```
return
end
*************************************************************
*  HistOut: Write the Histograms to disk
*************************************************************
subroutine HistOut
* GEANT common blocks
        INCLUDE 'nscl_bnmr:[prisc.geant.beta.ginc]gcflag.ins'
        INCLUDE 'nscl_bnmr:[prisc.geant.beta.ginc]gctmed.ins'
* User common blocks
        INCLUDE 'nscl_bnmr:[prisc.geant.beta.uinc]uoutput.ins'
INCLUDE 'nscl_bnmr:[prisc.geant.beta.uinc]uedep.ins'

write(*,*) 'On Event #',IDEVT
c write(*,*) 'EffP2 = ',EffP2,'+/-',ErrP2
write(*,*) 'EffP3 = ',EffP3,'+/-',ErrP3
write(*,*) 'EffDSSD',EffDSSD,'+/-',ErrDSSD
        write(*,*) 'Counts DSSD',CtDSSD

if (Begin.eq.1) then
     CALL HROPEN(20,'JIP',FileOut,'N',1024,ISTAT)
  CALL HROUT(0,VersNum,' ')
  CALL HREND('JIP')
  close(20)
  Begin = 0
else
  OPEN(20,File=FileOut,STATUS='OLD')
  close(20,STATUS='DELETE')
     CALL HROPEN(20,'JIP',FileOut,'N',1024,ISTAT)
  CALL HROUT(0,VersNum,' ')
  CALL HREND('JIP')
  close(20)
endif

return
end
*************************************************************
*  GAUSSRAN (function): Generate a random gaussian distribution
*************************************************************
real function GAUSSRAN(mu,sigma)

real mu,sigma,rndm(12),sum

call grndm(rndm,12)
sum=0.
do i=1,12
 sum=sum+rndm(i)
```

```
end do
gaussran=mu+(sum-6)*sigma
return
end
*************************************************************
*  dssd_last
*************************************************************
*  This is the main body code for initiating and nicely ending
*  GEANT simulation runs.
*************************************************************
subroutine UGLAST

* GEANT common blocks
        INCLUDE 'nscl_bnmr:[prisc.geant.beta.ginc]gcflag.ins'
* User common blocks
        INCLUDE 'nscl_bnmr:[prisc.geant.beta.uinc]uoutput.ins'
INCLUDE 'nscl_bnmr:[prisc.geant.beta.uinc]uedep.ins'

print *,'in jp_last'
        IF (MOD(IDEVT,output).NE.0) then
  print *,'before histout call'
          type*,'On Event #',idevt
* output all histograms into the hbook file.
call HistOut
  print *,'after histout call'
        endif
        print *,'before glast call'

*--Call standard GEANT termination routine.
call glast

return
end
```

A.0.5.2 Sample Input File

The following is a sample input file used to calculate the beta efficiency of ^{90}Sr ($Q_\beta = 546$ keV).

```
RNDM     5126527    35277282    !Initial random numbers
RUNG      1      1              !User run number
AUTO      0                     !=0 reads user defined tracking parameters
                                !=1 uses default tracking parameters
TRIG         25                 !Number of events to process
CUTS  0.000010 0.00001 0.000010 !Low energy cuts for particles
0.000010 0.000010 0.000010      !(see BASE040)
0.000010 1.e4 1.e4
```

```
0.000010 1.e10 0. 0. 0. 0. 0.
MUNU      0                      !Muon nuclear interaction flag
HADR      0                      !Hadronic process flag
DRAY      0                      !Delta-ray flag
DEBU      0      0     0         !1st event to debug, last, print freq.
TIME 100000  1  10000000         !Time left after initialization,
                                 !time required for termination,
                                 !test every itime events
ERAN   1.e-6    0.01    90       !
EVTPRT 1000              !Obsolete, used to print details of this event
KINEOPT   0                 !=0 emits particle w/ ENERGY in 4pi
                                 !=1 emits particle w/ ENERGY from 0-theta
                                 !=2 emits particle w/ ENERGY at theta & phi
BETOPT 0                 !=0 emits beta particle w/ realistic beta
                                 !spectrum w/ Qbeta = ENERGY
                                 !=1 emits beta with ENERGY
PARTICLE 3                 !Type of particle to emit [CONS300]
Z 38               !Proton number of emitting nucleus
AVER_DEPTH 691              !Aver. implantation depth (um) for
                                 !given nuclide
STD 6.28             !Sigma=FWHM/2.354 for AVER_DEPTH
ENERGY  546              !Energy of the particle (in keV)
OUTPUT 1000              !After OUTPUT number of evnts triggered,
                                 !HistOut subroutine triggered
                                 !(see dssd_out)
```

A.0.5.3 Running the GEANT simulation

Before the GEANT simulation can be run, the FORTRAN program shown in Sec. A.0.5.1 needs to be compiled. To compile the program, the following command file should be executed:

```
$ define cernlib DISK$SYS_LIB:[ALPHA.NSCL.CERNV5.97A.lib]
$ for dssd_geant
$ link/exe=dssd_geant.exe -
dssd_geant, -
CERNLIB:czdummy.obj, -
CERNLIB:ctldummy.obj, -
CERNLIB:gethostname.obj, -
CERNLIB:geant321/lib, -
CERNLIB:pawlib/lib, -
CERNLIB:graflib/lib, -
CERNLIB:grafx11/lib, -
CERNLIB:packlib/lib, -
CERNLIB:mathlib/lib, -
```

```
CERNLIB:kernlib/lib, -
grafmotif/opt
$ exit
```

Running this command file will generate an executable named dssd_geant.exe. To run this program in VMS, simply type:

```
run dssd_geant
```

This action will load the GEANT program, resulting in the GEANT prompt and a graphics window showing the detector setup (see Fig. A.1). To produce a given number of beta particles, N(beta), emitted from the source, type:

```
trigger N(beta).
```

As the program is currently set up, the calculated β efficiency from the simulation will be printed after every 1000 beta events. This may be modified by changing the OUTPUT number in the input file. Further instructions for using GEANT may be obtained from the GEANT online manual [75].

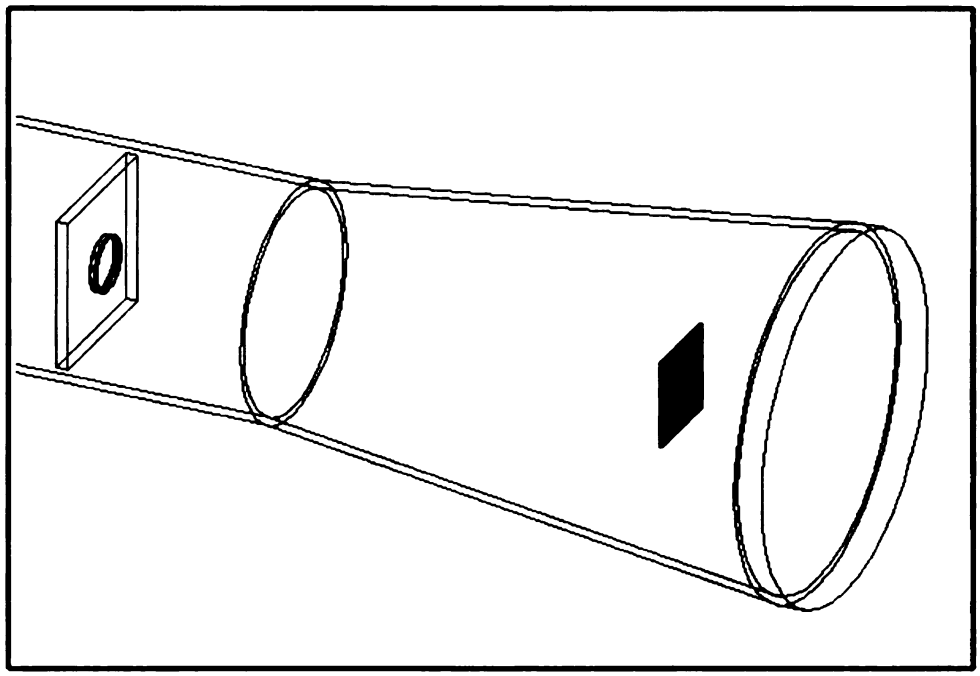

Figure A.1: GEANT simulated DSSD setup.

Appendix B

Gamma-ray Efficiency Calculations

B.0.6 Experimental Efficiency for Exp. 97004

To extract a peak gamma ray efficiency for the rotating target wheel experiment, a mixed gamma ray source consisting of ^{125}Sb and ^{154,155}Eu and a ^{228}Th source were utilized. The mixed source was produced at noon eastern standard time on September 1, 1988. The source consisted of 2.277 μCi ^{154}Eu, 0.7527 μCi ^{155}Eu and 1.630 μCi ^{125}Sb. The activity of each component of this mixed source has been determined from the tabulated emission rates for the gamma ray transitions associated with each of the radionuclides as provided by NIST. The activity of the ^{228}Th source was determined to be 0.5 μCi shortly after the measurement by Reg Ronningen. A 30 minute gamma ray singles spectrum was acquired for each source at the same source-to-detector distance used during the experiment (15 mm for the 80% HPGe detector and 45 mm for the 120% detector).

The prominent gamma ray peaks were fit to Gaussians using DAMM, providing the area of each fit, the error and the FWHM. An emission rate was calculated for each peak by dividing the area of the fit by the duration of measurement, 30 minutes. To correct for the computer and electronic dead time of the system, a pulser signal was transported through the test input of the Ge detectors. The ratio of the number of counts in the pulser peak to the number of counts emitted by the pulser provided a dead time correction factor of 0.252. Theoretical emission rates were calculated using Eq. 2.1 and an elapsed time of 3392.9 days from the time the source was

Table B.1: Sources used for total efficiency measurement.

Source	*Activity*(T_o) (μCi)	T_o	E_γ (keV)
^{57}Co	6.00	March 30, 1979	122, 136
^{60}Co	9.992	November 15, 1997	1173, 1332
^{137}Cs	10.11	November 1, 1988	667
^{228}Th	13.91	October 1, 1988	583, 2615

manufactured. By taking the ratio of the experimental to the theoretical emission rates, peak efficiencies were determined for the prominent gamma ray peaks. The data was fit with a fifth order polynomial of the form:

$$\log \epsilon_{peak} = 3.689 (\log E)^5 - 48.068 (\log E)^4 + 249.69 (\log E)^3 - 646.47 (\log E)^2 + 833.87 \log E - 429.83. \quad \text{(B.1)}$$

To correct the peak efficiency data for summing effects, it was necessary to extract a total efficiency curve for the Ge detectors. For this measurement, four sources were used, ^{57,60}Co, ^{137}Cs and ^{228}Th, see Table B.1.

To determine the total gamma ray efficiency for each of the sources listed in Table B.1, a gamma ray singles spectrum was acquired for 30 minutes. After the collection period, the gamma ray spectrum was summed from above a low energy threshold to a channel just below the pulser peak. A dead time correction factor was calculated similar to the method discussed above. The spectrum area was divided by the dead time correction factor, yielding a corrected spectrum area. To obtain the total efficiency, the corrected spectrum area was divided by the number of counts expected from the source (the theoretical activity of the source multiplied by the run time).

To calculate the total efficiency for the ^{57}Co source, several additional factors were taken into consideration. ^{57}Co emits two low-energy gamma rays of energy 122 keV and 136 keV in parallel. Thus, for each beta particle emitted by the source, one of the two gamma ray transitions is observed. The calculated total efficiency was calculated for the average of the two energies, 129 keV. In addition, since the two emitted

photons are low in energy, one must also consider a competing nuclear de-excitation mode, internal conversion. In this process, the excitation energy is transferred to an orbital electron within the atom, and the electron is emitted with an energy equal to the excitation energy minus the binding energy of the electron [76]. Thus, the total activity of the source is:

$$A = A_\gamma + A_{e-} = A_\gamma(1 + \alpha_T)$$

where A_γ is the activity due to the emission of gamma radiation, A_{e-} is the activity due to the conversion electron process and α_T is the total conversion coefficient, A_{e-}/A_γ. To correct for this process, the calculated ϵ_T was multiplied by $(1 + \alpha_T)$, 1.177 [77], where α_T was the average α_T for the 122 keV and 136 keV transitions.

When calculating the total efficiency for ^{60}Co, one needs to consider that for each emitted beta particle, two gamma rays, 1173 keV and 1332 keV, are emitted in series. Thus, the calculated total efficiency was divided by two. In addition, the total efficiency was calculated for the average of the two energies, 1253 keV.

In the case of ^{228}Th, the three prominent gamma rays emitted by the source are 269 keV, 583 keV and 2615 keV. To determine the total efficiency at an energy of 2615 keV, the gamma ray spectrum was summed from above 586 keV. To account for the Compton scattered gamma rays below 586 keV, a background line extending to the beginning of the spectrum was drawn. The area encompassed by this box was extracted and added to area of the spectrum above 586 keV. To determine the total efficiency at 2614 keV, the number of counts in the pulser peak was deducted from the calculated value. To correct for dead time, this value was divided by the dead time correction factor. The total efficiency was determined by dividing the corrected spectrum area by the number of counts expected from the source (the theoretical number of counts).

Figure B.1 depicts the total efficiency for the four sources detailed above. The data was fit with a second order polynomial of the form:

$$\epsilon_{Total} = 1\text{x}10^{-8}\ \text{E}^2 - 5\text{x}10^{-5}\ \text{E} + 0.097 \qquad \text{(B.2)}$$

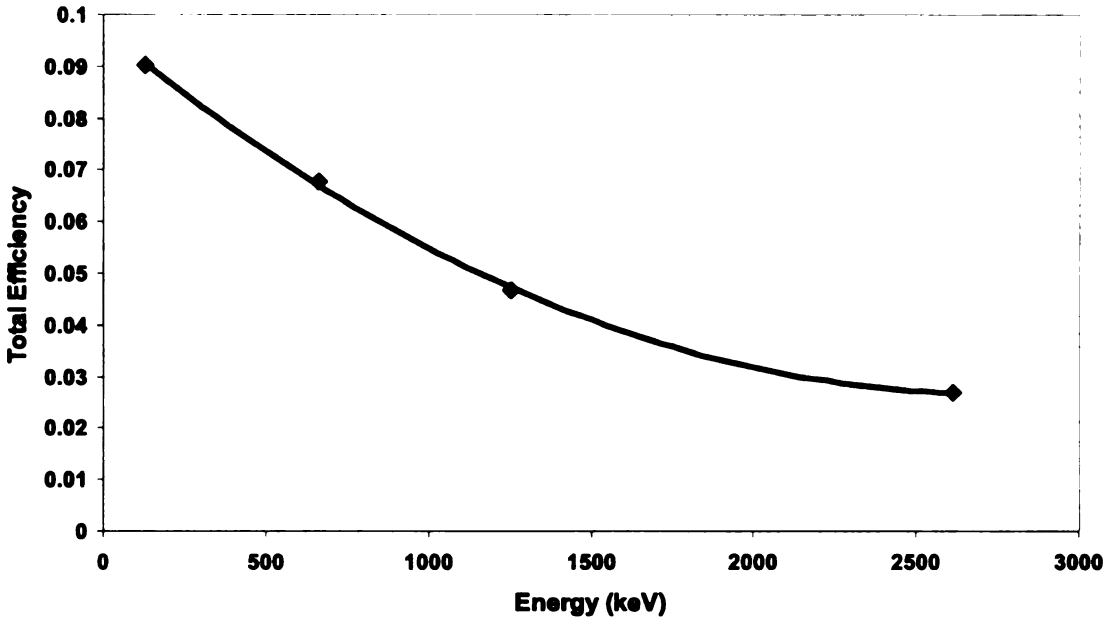

Figure B.1: Total efficiency for the 120% Ge detector at a source-to-detector distance of 45 mm. The solid line is a second order polynomial fit to the data.

Using the fits to the uncorrected peak and total efficiency data, the summing correction factors listed in Table B.2 were calculated (see discussion in Appendix C). Sum corrected peak efficiencies were determined by dividing the uncorrected peak efficiencies by the correction factors. To extend the peak efficiency data to higher energies, a ^{228}Th source was utilized. ^{228}Th emits three prominent gamma rays of energy 269 keV, 583 keV and 2614 keV. The peak efficiencies for the 583 keV and 2615 keV gamma rays were calculated in a similar manner discussed for the mixed source.

The correction factors for the 583 and 2615 keV peaks were deduced from Eq. C.5. p_γ was calculated by multiplying the relative intensity of the photon of interest by 0.9916 [9]. Table B.3 lists gamma rays coincident with the 583 keV and 2615 keV transitions, and the calculated coefficients (p_γ/p_{583} and p_γ/p_{2615}) for the summing corrections. Neglecting terms with coefficients less than 0.01, the summing corrections

Table B.2: Summing corrections for the prominent gamma rays emitted by the mixed gamma ray source as documented by NIST. {E} is the uncorrected peak efficiency for a gamma ray emitted with energy E and [E] is the total efficiency at energy E. To get the correction factor in the same form as discussed in Appendix C, take the inverse of the correction term.

E (keV)	*Correction*
86.6	1.0
105.3	1.0
123.1	(1.0-0.072[248.0]-0.055[591.7]-0.019[692.4]-0.120[723.3] -0.049[756.9]-0.130[873.2]-0.201[1004.8]-0.010[1246.2] -0.401[1274.4]-0.021[1596.5])
176.4	(1.0-0.035[204.1]-0.057[321.0])
248.0	(1.0-0.287[42.8]-0.455[123.1]-0.072[444.4]-0.022[582.0] -0.134[591.7]-0.015[612.2]-0.043[625.2]-0.022[676.6] -0.039[723.3]-0.613[756.9]-0.059[892.7]-0.022[904.1] -0.130[1246.2]
380.5	(1.0+0.157{176.4}{204.1}/{380.5})*(1.0-0.010[27.4] -0.190[116.9])
427.9	(1.0-0.598[27.4]-0.059[35.5])
463.4	(1.0+0.169{35.5}{427.9}/{463.4})
591.7	(1.0-0.297[42.8]-0.455[123.1]-0.178[248.0]-0.196[756.9] -0.800[1004.8])
600.6	(1.0+0.010{427.9}{172.6}/{600.6})*(1.0-0.597[27.4] -0.059[35.5])
635.9	(1.0+0.012{427.9}{208.0}/{635.9})*(1.0-0.597[27.4] -0.059[35.5])
723.3	(1.0-0.154[42.8]-0.243[123.1]-0.013[248.0]-0.014[625.2] -0.518[873.2]-0.465[996.4])
873.2	(1.0+0.024{248.0}{625.2}/{873.2})*(1.0-0.282[42.8] -0.455[123.1]-0.894[723.3])
996.4	(1.0+0.507{123.1}{873.2}/{996.4})*(1.0-0.894[723.3])
1004.8	(1.0+0.221{248.0}{756.9}/{1004.8})*(1.0-0.282[42.8] -0.455[123.1]-0.217[591.7])
1274.4	(1.0+0.014{692.4}{582.0}/{1274.4})*(1.0-0.281[42.8] -0.455[123.1])
1596.5	(1.0+0.275{692.4}{904.1}/{1596.5}+5.568{873.2} *{723.3}/{1596.5}+2.094{1004.8}{591.7}/{1596.5} +0.052{1118.5}{478.3}/{1596.5})*(1.0-0.281[42.8] -0.455[123.1])

Table B.3: Summing correction coefficients for the 583 keV and 2615 keV gamma rays emitted following the decay of ^{208}Tl, a member of ^{228}Th decay chain.

E (keV)	*Rel. Intensity*	p_γ	*Coefficient*(583)
277.4	6.36×10^{-2}	6.31×10^{-2}	7.46×10^{-2}
510.8	2.28×10^{-1}	2.26×10^{-1}	2.68×10^{-1}
722.0	2.03×10^{-3}	2.03×10^{-3}	2.38×10^{-3}
748.7	4.30×10^{-4}	4.26×10^{-4}	5.05×10^{-4}
763.1	1.83×10^{-2}	1.81×10^{-2}	2.15×10^{-2}
927.6	1.32×10^{-3}	1.31×10^{-3}	1.55×10^{-3}
982.7	2.05×10^{-3}	2.03×10^{-3}	2.41×10^{-3}
1160.8	1.10×10^{-4}	1.09×10^{-4}	1.29×10^{-4}
1185.1	1.70×10^{-4}	1.69×10^{-4}	2.00×10^{-4}
1282.8	5.20×10^{-4}	5.16×10^{-4}	6.10×10^{-4}
2614.5	1.00	0.9916	1.17
E (keV)	*Rel. Intensity*	p_γ	*Coefficient*(2615)
583.1	8.52×10^{-1}	8.45×10^{-1}	8.52×10^{-1}
860.6	1.25×10^{-1}	1.24×10^{-1}	1.25×10^{-1}
1093.9	4.00×10^{-3}	3.97×10^{-4}	4.00×10^{-4}
1381.1	7.00×10^{-5}	6.94×10^{-5}	7.00×10^{-5}
1744.0	2.00×10^{-5}	1.98×10^{-5}	2.00×10^{-5}

have been calculated as follows:

$$C_{583} = \frac{1}{(1 - 0.0746[277.4] - 0.268[510.8] - 0.0215[763.1] - 0.992[2614.5])} \quad \text{(B.3)}$$

$$C_{2615} = \frac{1}{(1 - 0.852[583.1] - 0.125[860.6])} \quad \text{(B.4)}$$

To incorporate these data points into the corrected peak efficiency plot determined for the mixed source, these value were first normalized. A linear regression of the peak efficiencies at energies 463 keV and 592 keV, scaled the 583 keV efficiency from 1.48% to 2.31%. To properly adjust the peak efficiency for the 2615 keV gamma ray, the calculated peak efficiency was multiplied by a scaling factor,

$$ScalingFactor = \frac{Normalized\ \epsilon_{pk}(583)}{Calculated\ \epsilon_{pk}(583)}.$$

Figure B.2 depicts the peak efficiency data points for the mixed source and the ^{228}Th source. Table B.4 provides a list of the energies, calculated peak efficiencies and errors shown in Fig. B.2. To determine the peak efficiency at an unknown energy, the data

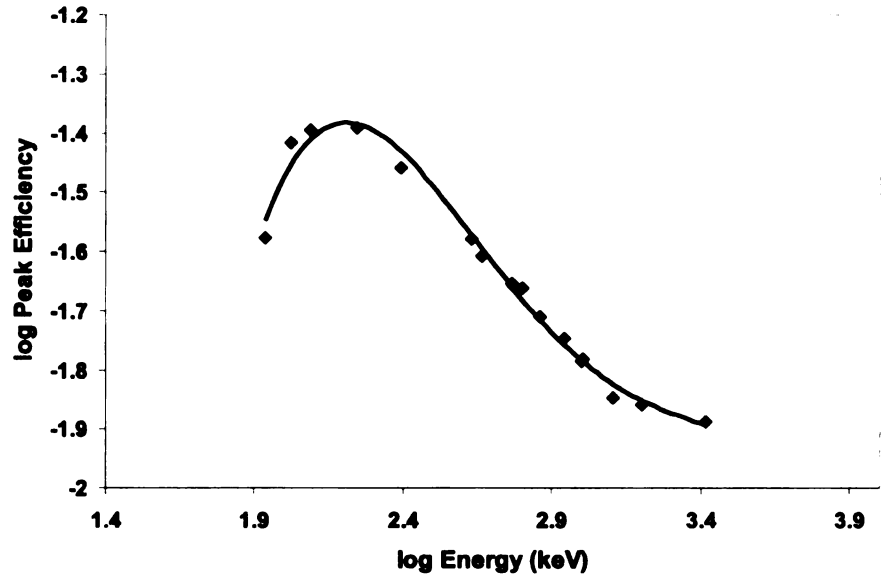

Figure B.2: Sum corrected peak efficiency for the 120% Ge detector at a source-to-detector distance of 45 mm. The solid line represents a fifth order polynomial fit to the data.

was fit to a fifth order polynomial of the form:

$$\log \epsilon_{peak}(120\%) = 1.5093\,(\log E)^5 - 20.79\,(\log E)^4 + 114.2\,(\log E)^3 - 312.65\,(\log E)^2 + 426.02\log E - 232.16. \quad \text{(B.5)}$$

The peak efficiency for the 80% detector at a source-to-detector distance of 15 mm was determined in a similar manner as the 120% HPGe. Table B.4 provides a list of the energies, peak efficiencies and errors calculated for this second Ge detector. The data was fit to a fifth order polynomial of the form:

$$\log \epsilon_{peak}(80\%) = -1.2848\,(\log E)^5 + 16.499\,(\log E)^4 - 82.019\,(\log E)^3 + 194.97\,(\log E)^2 - 217.38\,(\log E) + 86.276. \quad \text{(B.6)}$$

In the orientation discussed above for the 80% and the 120% Ge detectors, a peak γ-ray efficiency of 4.5% at 1.274 MeV was attained.

Table B.4: Peak efficiency data for the 120% and 80% Ge detector used in Exp. 97004.

E (keV)	*Ge 120%*		*Ge 80%*	
	ϵ_{peak} (%)	*Error*	ϵ_{peak} (%)	*Error*
86.6	2.65	0.13	0.708	0.11
105.3	3.83	0.18	1.43	0.16
123.1	4.03	0.06	3.10	0.06
176.4	4.07	0.45	3.34	0.53
248.0	3.63	0.03	8.83	0.12
427.9	2.75	0.03	6.64	0.08
463.4	2.48	0.05	5.36	0.11
583.1	2.31	0.01	5.01	0.01
591.7	2.30	0.03	4.98	0.09
600.6	2.27	0.04	5.14	0.13
635.9	2.26	0.04	4.80	0.12
723.3	1.98	0.02	4.21	0.07
873.2	1.86	0.02	3.80	0.06
996.4	1.64	0.02	3.38	0.08
1004.8	1.72	0.02	3.52	0.06
1274.4	1.48	0.01	2.98	0.03
1596.5	1.39	0.03	3.13	0.05
2614.5	1.35	0.03	2.47	0.01

Table B.5: Peak efficiency data for the 120% and 80% Ge detectors used in Exp. 98020.

E (keV)	*Ge 120%*		*Ge 80%*	
	ϵ_{peak} (%)	*Error*	ϵ_{peak} (%)	*Error*
123.1	0.755	0.015	0.753	0.029
248.0	1.020	0.110	0.940	0.067
427.9	0.825	0.073	0.826	0.077
463.4	0.849	0.138	0.705	0.156
591.7	0.885	0.085	0.622	0.051
600.6	0.369	0.186	0.691	0.094
635.9	0.577	0.151	0.596	0.130
723.3	0.713	0.021	0.567	0.031
873.2	0.672	0.022	0.560	0.021
996.4	0.635	0.031	0.529	0.031
1004.8	0.676	0.021	0.506	0.022
1274.4	0.590	0.009	0.432	0.009
1596.5	0.588	0.033	0.380	0.026

B.0.7 Experimental Efficiency for Exp. 98020

To determine the peak gamma ray efficiency for the DSSD experiment, the mixed gamma ray source was used. The peak efficiencies were calculated using the same method discussed above. The calculated efficiencies for the 120% and the 80% Ge detectors were corrected for summing. However, since the clover detector consisted of smaller crystals (four 25% crystals), and were further removed from the source, summing corrections were not performed on the clover detectors. To determine the peak efficiencies for each of the clover detectors, the gamma ray spectra for each crystal within a given clover were summed on an event-by-event basis. A dead time correction factor was obtained for each detector by taking the ratio of the number of counts in the master gate live scaler to the master gate scaler. The peak efficiencies for the prominent gamma ray transitions are listed in Tables B.5–B.6, however, note that these efficiencies were determined for a point source.

B.0.7.1 Computer Simulation

In the DSSD experiment, the secondary beam was defocussed to illuminate $\approx 2/3$ of the active area of the strip detector. To determine the peak efficiency for an extended

Table B.6: Peak efficiency data for the Ge clover detectors used in Exp. 98020.

E (keV)	*GeC1*		*GeC2*		*GeC3*	
	ϵ_{peak} (%)	*Error*	ϵ_{peak} (%)	*Error*	ϵ_{peak} (%)	*Error*
86.6	1.56	0.28	1.48	0.22	1.54	0.26
105.3	2.18	0.38	2.02	0.30	2.60	0.38
123.1	2.15	0.09	2.24	0.08	2.48	0.09
248.0	1.93	0.08	2.03	0.09	2.25	0.13
427.9	1.58	0.11	1.62	0.11	1.72	0.13
463.4	1.64	0.21	1.27	0.20	1.66	0.25
591.7	1.28	0.08	1.23	0.07	1.37	0.07
600.6	1.13	0.13	1.34	0.13	1.47	0.13
635.9	1.21	0.17	1.26	0.16	1.32	0.17
723.3	1.20	0.04	1.17	0.02	1.28	0.04
873.2	1.01	0.02	1.02	0.03	1.14	0.05
996.4	0.978	0.035	1.01	0.04	1.10	0.07
1004.8	1.01	0.03	0.993	0.031	1.09	0.05
1274.4	0.875	0.022	0.852	0.040	0.953	0.045
1596.5	0.849	0.049	0.854	0.054	0.964	0.039

gamma ray source, MCNP, a general Monte Carlo N-particle transport code, was utilized.

To perform the simulation, it was necessary to enter the dimensions and the geometries of the Ge detectors within the MCNP input file.

The Ge crystal in the 120% detector is 105.8 mm in length, and 80.8 mm in diameter. The distance from the endcap to the crystal is 4 mm. The closed-ended coaxial detector has a hole 8 mm in diameter and 92 mm deep running through the core of the crystal. The core of the detector was removed to provide an electrical contact. A second contact was produced by placing an electrode on the outer surface of the Ge crystal. A 0.7 mm layer of inactive Ge runs along the outer perimeter of the crystal.

The crystal in the 80% detector is 92.0 mm in length and 75.5 mm in diameter. There is a 4 mm distance between the crystal and the endcap of the detector. This coaxial detector has a hole 8 mm in diameter and 78 mm in length through its core. Similar to the 120% Ge detector, a 0.7 mm layer of inactive Ge runs along the outer

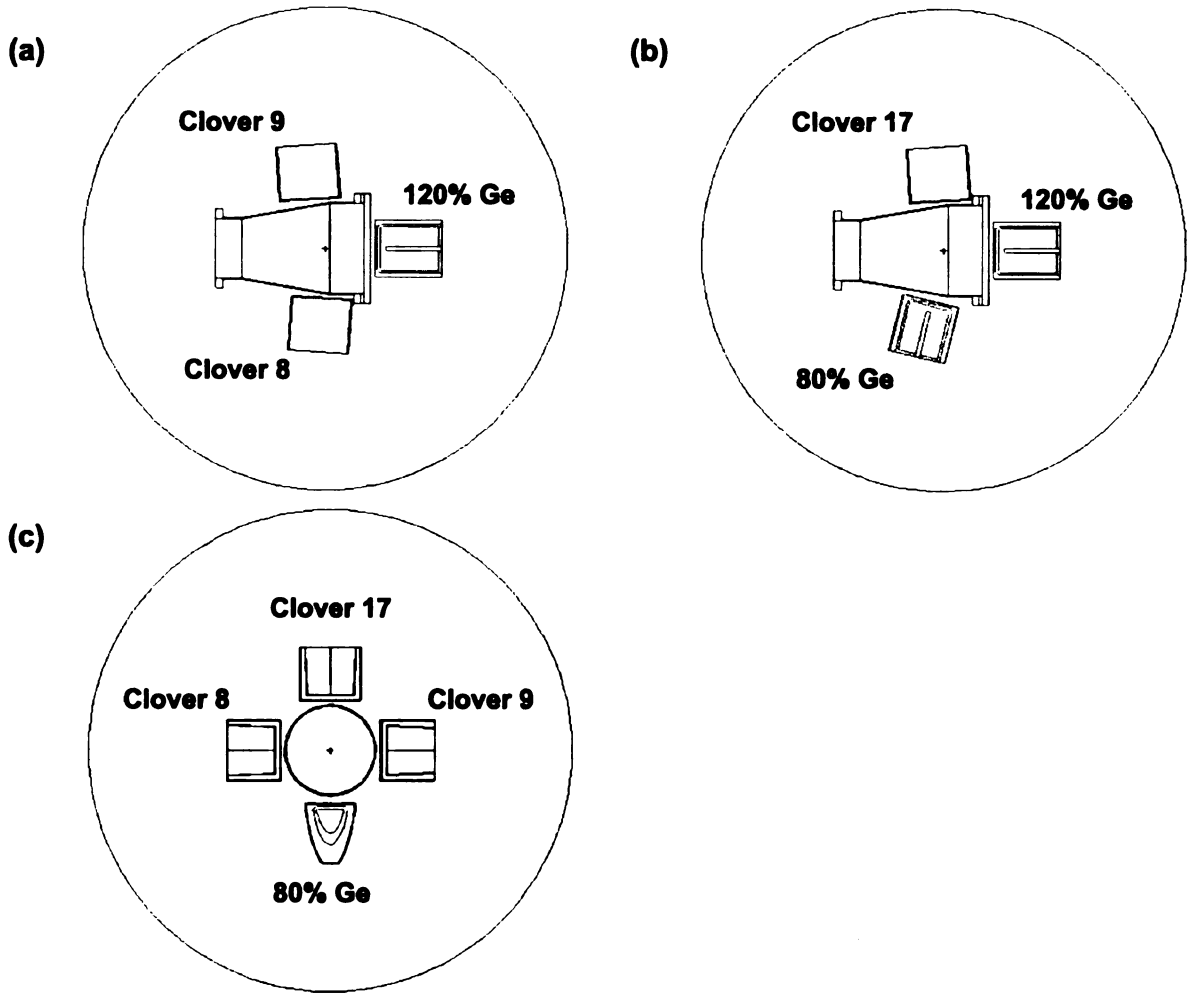

Figure B.3: The simulated Ge detector orientations in the (a)x-y plane, (b)x-z plane and (c)y-z plane.

perimeter the 80% crystal.

The crystals in the clover detectors are 80 mm in length and 45 mm wide. The inner edges of the crystals have been shaved to configure four crystals in clover geometry. There is a 0.2 mm gap between each pair of crystals. In addition, the distance from the crystal to the endcap of the detector is 10 mm.

Once the dimensions and the geometries of the Ge detectors were entered into MCNP (see Fig. B.3), a simulation was performed to compare the experimental peak efficiencies of the detectors with the simulated efficiencies. To make this comparison, a point source was simulated using the energies listed in Tables B.5–B.6. The simulated and experimental measurements were in good agreement for the 80% and 120% Ge

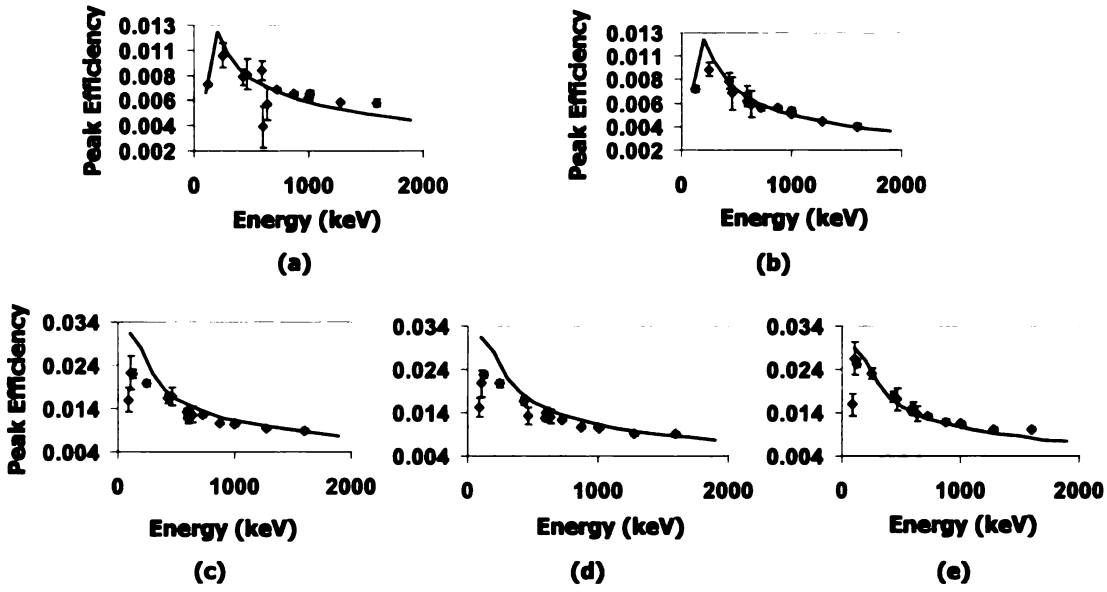

Figure B.4: The experimental and simulated peak efficiencies for a point source for (a) the 120% Ge detector, (b) the 80% detector, (c) clover 8, (d) clover 17 and (e) clover 9. The energy spectra for each crystal within a given clover has been summed yielding a total energy spectrum for the clover. The solid line represents the MCNP simulation. Note that a dead layer was not considered in the MCNP simulation for the clover detectors.

detector when a 4.5 mm dead layer was considered (see Fig. B.4). The inactive Ge layer in both the 80% and 120% Ge detectors were extended from the manufacturer's quoted value to better match the experimental peak efficiencies at low energy. One would expect a larger dead layer on these detectors because both crystals are p-type. In p-type detectors, the high voltage contact is placed on the outside of the crystal, thereby increasing the inactive layer of germanium. The clover detectors, on the other hand, are n-type crystals. In n-type detectors, the high voltage contact is along the core of the crystal. Thus, one would expect a much smaller inactive Ge layer in n-type detectors.

To determine the peak efficiency for the DSSD setup, an extended gamma source was simulated in MCNP. An extended source 2.5 cm in diameter and offset by 4 mm up and 4 mm to the right of the center of the DSSD was considered to mimic the beam profile shown in Fig. 3.7. A 1 mm dead layer on the face and outer perimeter of the clover detectors was considered to improve the agreement between the experimental

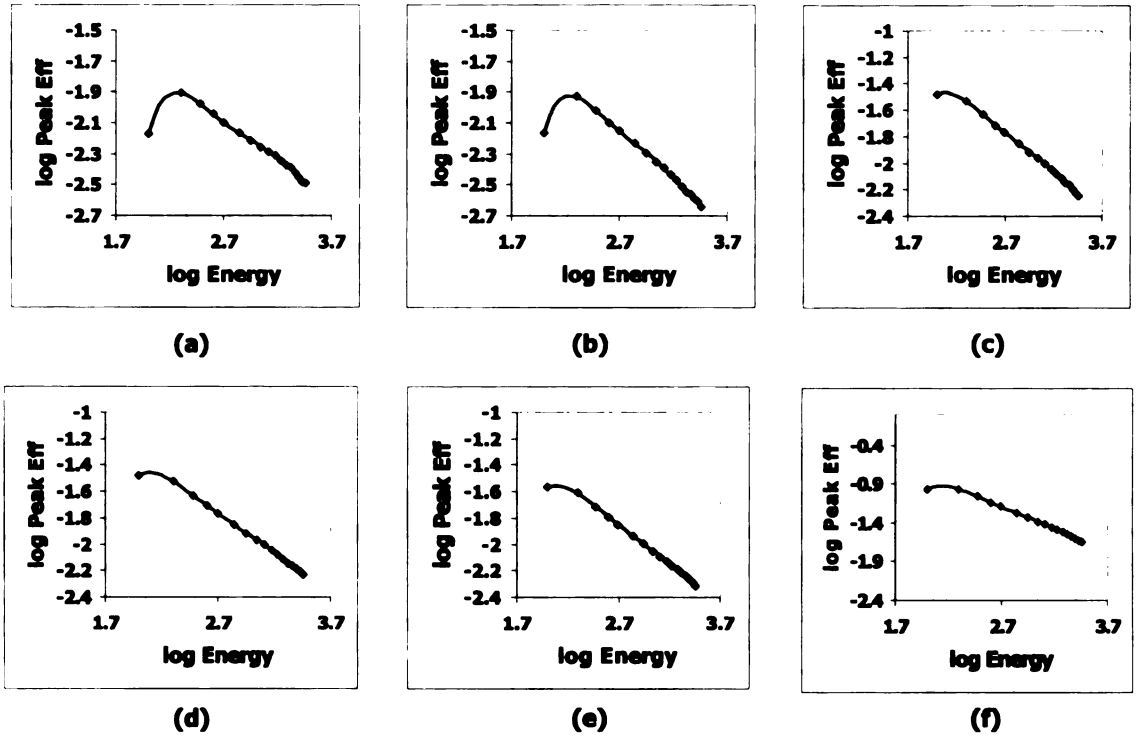

Figure B.5: The simulated peak efficiencies for an extended source for (a) the 120% Ge detector, (b) the 80% detector, (c) clover 8, (d) clover 17, (e) clover 9 and (f) the Ge array. The solid line is a fifth order polynomial fit to the simulated efficiency data.

and simulated peak efficiencies. Figure B.5 shows the simulated peak efficiencies for the extended source and Table B.7 lists the fit parameters.

To ensure that the MCNP simulation was treating the extended source properly, several experimental runs were performed with a ^{22}Na source. The location of the point source was varied for each run. Thirty minute measurements were made with the source placed at the center and four corners of the DSSD position. The area of the 511 keV peak was extracted for each source position and normalized by dividing the area by the real time of the measurement. To compare the results with the simulation, a ratio of the corrected area of the 511 keV peak when the source was placed on each corner was divided by the area of the 511 when the source was located at the center position. Table B.8 lists the experimental and simulated 511 keV ratios. The values are in good agreement, suggesting that the simulation was indeed treating the extended

Table B.7: A fit to the simulated peak efficiency for an extended source for the Ge detectors used in Exp. 98020. The fit is in the form: $\log \epsilon_{peak}$ = A*(log E)^5 + B*(log E)^4 + C *(log E)^3 + D*(log E)^2 + E*log E + F.

Detector	*A*	*B*	*C*	*D*	*E*	*F*
80% Ge	1.351	-19.566	112.71	-322.88	459.43	-261.39
120% Ge	0.9035	-13.621	81.452	-241.54	354.79	-208.18
Clover 8	0.3931	-5.8652	34.639	-101.27	146.05	-84.348
Clover 9	0.1868	-2.9707	18.603	-57.42	86.865	-52.884
Clover 17	0.4849	-7.0859	41.124	-118.48	168.85	-96.395
Ge Array	0.4982	-7.3746	43.324	-126.29	182.16	-104.66

Table B.8: Comparison of the experimental and simulated ratios of the 511 keV peak area for the ^{22}Na at the four corners of the DSSD position to its central position. The positions are designated as UR (upper right), UL (upper left), LR (lower right), LL (lower left) and CC (center).

Ratio	*Ge 120%*		*Ge 80%*	
	Exp.	*MCNP*	*Exp.*	*MCNP*
UR/CC	0.797(14)	0.833	0.683(33)	0.615
UL/CC	0.810(13)	0.830	0.647(31)	0.599
LR/CC	0.888(13)	0.836	1.660(76)	1.438
LL/CC	0.870(17)	0.828	1.196(58)	1.443

source properly. However, it should be noted that the peak efficiencies calculated for an extended source did not differ greatly from the peak efficiencies calculated for a point source (ϵ_{peak}(extended) = 0.33% and ϵ_{peak}(point) = 0.43% at 1.27 MeV for the 80% HPGe).

B.0.7.2 Sample Input File

The following is a sample input file. It specifies the dimensions and geometries of the 80%, the 120% and the three clover Ge detectors. In addition, an extended source has been simulated. In this simulation, 500000 photons of energy 900 keV were emitted by the source.

```
c 98020 experiment with extended source
1       0 1  $outside world
2       2 -0.00114 -1 #3 #4 #5 #6 #7 #8 #9
        #10 #11 #12 #(30 -31 -20) #(44 -45 -34)
        #(47 -49 50 -51 52 -57)
```

Table B.9: Continued:Comparison of the experimental and simulated ratios of the 511 keV peak area for the ^{22}Na at the four corners of the DSSD position to its central position. The positions are designated as UR (upper right), UL (upper left), LR (lower right), LL (lower left) and CC (center). Each crystal of the clover detectors is labelled as A, B, C and D. In addition, the MCNP simulation is listed as A, B, C and D.

Ratio	*Clover 8*							
	Exp. A	*A*	*Exp. B*	*B*	*Exp. C*	*C*	*Exp. D*	*D*
UR/CC	1.20(13)	1.28	1.32(8)	1.22	1.73(19)	1.82	1.93(11)	1.72
UL/CC	0.65(7)	0.61	0.67(4)	0.62	0.71(8)	0.66	0.68(4)	0.68
LR/CC	1.80(20)	1.75	2.00(11)	1.82	1.26(14)	1.22	1.38(9)	1.17
LL/CC	0.74(8)	0.67	0.75(4)	0.72	0.64(7)	0.57	0.67(4)	0.59
Ratio	*Clover 17*							
	Exp. A	*A*	*Exp. B*	*B*	*Exp. C*	*C*	*Exp. D*	*D*
UR/CC	1.75(16)	1.79	2.08(20)	1.74	1.31(14)	1.21	1.41(16)	1.24
UL/CC	1.22(11)	1.20	1.38(14)	1.23	1.75(19)	1.80	1.85(21)	1.80
LR/CC	0.65(6)	0.71	0.68(7)	0.65	0.58(7)	0.57	0.62(7)	0.60
LL/CC	0.59(6)	0.60	0.64(7)	0.58	0.68(7)	0.69	0.66(8)	0.66
Ratio	*Clover 9*							
	Exp. A	*A*	*Exp. B*	*B*	*Exp. C*	*C*	*Exp. D*	*D*
UR/CC	0.58(5)	0.56	0.55(6)	0.62	0.62(8)	0.71	0.63(7)	0.73
UL/CC	1.10(9)	1.29	1.03(11)	1.09	1.72(22)	1.89	1.52(16)	1.49
LR/CC	0.61(5)	0.66	0.66(7)	0.71	0.60(8)	0.56	0.56(6)	0.61
LL/CC	1.72(14)	1.82	1.69(18)	1.52	1.29(16)	1.31	1.24(13)	1.08

```
      #(76 -78 79 -80 81 -86)
      #(105 -107 108 -80 81 -115) $inside world
3     3 -2.71 -2 3 -4          $iso160 backplate
4     3 -2.71  7 -3 -4 6       $iso160 oring
5     3 -2.71  8 -7 -4 6       $iso160 flange
6     3 -2.71  -5 6 -8 9       $chamber wall 1
7     3 -2.71  -9 11 -12 13    $chamber wall 2
8     3 -2.71  -13 15 -14 16   $chamber wall 3
9     3 -2.71  18 -16 15 -17   $iso100 flange
10    0 -6 -3  9               $chamber vacuum 1
11    0 -11 -9 13              $chamber vacuum 2
12    0 -15 -13 18             $chamber vacuum 3
13    0 22 -20 -23                      $Ge080 center contact
14    1 -5.32 24 -25 -26 -28 #13        $Ge080 active area
15    1 -5.32 19 -20 -21 -27 #13 #14    $Ge080 crystal
16    0 29 -32 -20 #15 #14 #13          $Ge080 vacuum region
17    3 -2.71 30 -31 -20 #16 #15 #14 #13   $Ge080 cryostat
18    0 36 -34 -37                      $Ge120 center contact
19    1 -5.32 38 -39 -40 -42 #18        $Ge120 active area
20    1 -5.32 33 -34 -35 -41 #18 #19    $Ge120 crystal
21    0 43 -46 -34 #20 #19 #18          $Ge120 vacuum region
22    3 -2.71 44 -45 -34 #21 #20 #19 #18   $Ge120 cryostat
23    1 -5.32 -72 67 -57 -69  70           $clover Ge active area red
24    1 -5.32 -73 67 -57 -69 -71           $clover Ge active area green
25    1 -5.32 -74 67 -57  68  70           $clover Ge active area blue
26    1 -5.32 -75 67 -57  68 -71           $clover Ge active area black
27    1 -5.32 -62 66 -57 -59  60 #23       $clover Ge crystal red
28    1 -5.32 -63 66 -57 -59 -61 #24       $clover Ge crystal green
29    1 -5.32 -64 66 -57  58  60 #25       $clover Ge crystal blue
30    1 -5.32 -65 66 -57  58 -61 #26       $clover Ge crystal black
31    0 48 -53 54 -55 56 -57 #27 #28
      #29 #30 #23 #24 #25 #26  $clover vaccum region
32    3 -2.71 47 -49 50 -51 52 -57 #31
      #27 #28 #29 #30 #23 #24 #25 #26  $clover cryostat
33    1 -5.32 -101 96 -86 -98   99        $clover Ge active area blue
34    1 -5.32 -102 96 -86 -98 -100        $clover Ge active area red
35    1 -5.32 -103 96 -86  97   99        $clover Ge active area black
36    1 -5.32 -104 96 -86  97 -100        $clover Ge active area green
37    1 -5.32  -91 95 -86 -88   89 #33    $clover Ge crystal blue
38    1 -5.32  -92 95 -86 -88  -90 #34    $clover Ge crystal red
39    1 -5.32  -93 95 -86  87   89 #35    $clover Ge crystal black
40    1 -5.32  -94 95 -86  87  -90 #36    $clover Ge crystal green
41    0 77 -82 83 -84 85 -86 #37 #38 #39
      #40 #33 #34 #35 #36  $clover vacuum region
42    3 -2.71 76 -78 79 -80 81 -86 #41
      #37 #38 #39 #40 #33 #34 #35 #36  $clover cryostat
43    1 -5.32 -130 125 -115 -127   99      $clover Ge active area blue
```

```
44     1 -5.32 -131 125 -115 -127 -100      $clover Ge active area red
45     1 -5.32 -132 125 -115  126   99      $clover Ge active area black
46     1 -5.32 -133 125 -115  126 -100      $clover Ge active area green
47     1 -5.32 -120 124 -115 -117   89 #43  $clover Ge crystal blue
48     1 -5.32 -121 124 -115 -117  -90 #44  $clover Ge crystal red
49     1 -5.32 -122 124 -115  116   89 #45  $clover Ge crystal black
50     1 -5.32 -123 124 -115  116  -90 #46  $clover Ge crystal green
51     0 106 -111 112 -84 85 -115 #47 #48
       #49 #50 #43 #44 #45 #46  $clover vaccum region
52     3 -2.71 105 -107 108 -80 81 -115
       #51 #47 #48 #49 #50 #43 #44 #45 #46  $clover cryostat

1     so 40           $world
2     px 7.50               $chamber backplate
3     px 6.30               $chamber backplate
4     cx 9.00               $chamber backplate od
5     cx 7.70               $chamber od iso160 end
6     cx 7.40               $chamber id iso160 end
7     px 5.90               $chamber iso160 o-ring
8     px 4.70               $chamber iso160 flange
9     px 0.70               $chamber transition iso160 end
11     kx -41.668 .0305 1   $chamber transition id
12     kx -43.386 .0305 1   $chamber transition od
13     px -13.90            $chamber transition iso100 end
14     cx 5.15              $chamber od iso100 end
15     cx 4.85              $chamber id iso100 end
16     px -16.90            $chamber iso100 flange
17     cx 6.50              $chamber od iso100 flange
18     px -18.10            $chamber end
19     1  px 9.00            $Ge080 front crystal
20     1  px 18.20           $Ge080 back crystal
21     1  cx 3.775           $Ge080 crystal od
22     1  px 10.40           $Ge080 central contact
23     1  cx 0.4             $Ge080 crystal id
24     1  px 9.45            $Ge080 front active area
25     1  cx 3.325           $Ge080 active area od
26     1  px 17.75           $Ge080 back active area
27     1  kx 5.70 1          $Ge080 bullet crystal
28     1  kx 6.35 1          $Ge080 bullet active area
29     1  px 8.6             $Ge080 inner face cryostat
30     1  px 8.5             $Ge080 outer face cryostat
31     1  cx 4.75            $Ge080 od cryostat
32     1  cx 4.65            $Ge080 id cryostat
33     px 8.6          $Ge120 front crystal
34     px 19.18        $Ge120 back crystal
35     cx 4.04         $Ge120 crystal od
36     px 9.98         $Ge120 central contact
```

```
37      cx 0.4          $Ge120 crystal id
38      px 9.05         $Ge120 front active area
39      cx 3.59         $Ge120 active area od
40      px 18.73        $Ge120 back active area
41      kx 5.0 1        $Ge120 bullet crystal
42      kx 5.6 1        $Ge120 bullet active area
43      px 8.2          $Ge120 inner face cryostat
44      px 8.1          $Ge120 outer face cryostat
45      cx 4.75         $Ge120 od cryostat
46      cx 4.65         $Ge120 id cryostat
47      2  px 8.1                  $clover outer face cryostat
48      2  px 8.3                  $clover inner face cryostat
49      2  py 5.05                 $clover left cryostat outer wall
50      2  py -5.05                $clover right cryostat outer wall
51      2  pz 5.05                 $clover top cryostat outer wall
52      2  pz -5.05                $clover bottom cryostat outer wall
53      2  py 4.85                 $clover left cryostat inner wall
54      2  py -4.85                $clover right cryostat inner wall
55      2  pz 4.85                 $clover top cryostat inner wall
56      2  pz -4.85                $clover bottom cryostate inner wall
57      2  px 17.1                 $clover back crystal
58      2  py 0.01                 $clover spacing +y
59      2  py -0.01                $clover spacing -y
60      2  pz 0.01                 $clover spacing +z
61      2  pz -0.01                $clover spacing -z
62      2  c/x -1.7777 1.7777 2.5    $clover Ge crystal red
63      2  c/x -1.7777 -1.7777 2.5   $clover Ge crystal green
64      2  c/x 1.7777 1.7777 2.5     $clover Ge crystal blue
65      2  c/x 1.7777 -1.7777 2.5    $clover Ge crystal black
66      2  px 9.1                   $clover front crystal
67      2  px 9.2                   $clover front active area
68      2  py 0.02                  $clover active spacing +y
69      2  py -0.02                 $clover active spacing -y
70      2  pz 0.02                  $clover active spacing +z
71      2  pz -0.02                 $clover active spacing -z
72      2  c/x -1.7777 1.7777 2.4    $clover Ge active area red
73      2  c/x -1.7777 -1.7777 2.4   $clover Ge active area green
74      2  c/x 1.7777 1.7777 2.4     $clover Ge active area blue
75      2  c/x 1.7777 -1.7777 2.4    $clover Ge active area black
76      3  px 8.1                   $clover outer face cryostat
77      3  px 8.3                   $clover inner face cryostat
78      3  py 5.05                  $clover left cryostat outer wall
79      3  py -5.05                 $clover right cryostat outer wall
80      3  pz 5.05                  $clover top cryostat outer wall
81      3  pz -5.05                 $clover bottom cryostat outer wall
82      3  py 4.85                  $clover left cryostat inner wall
83      3  py -4.85                 $clover right cryostat inner wall
```

```
84     3  pz 4.85                  $clover top cryostat inner wall
85     3  pz -4.85                 $clover bottom cryostate inner wall
86     3  px 17.1                  $clover back crystal
87     3  py 0.01                  $clover spacing +y
88     3  py -0.01                 $clover spacing -y
89     3  pz 0.01                  $clover spacing +z
90     3  pz -0.01                 $clover spacing -z
91     3  c/x -1.7777 1.7777 2.5   $clover Ge crystal blue
92     3  c/x -1.7777 -1.7777 2.5  $clover Ge crystal red
93     3  c/x 1.7777 1.7777 2.5    $clover Ge crystal black
94     3  c/x 1.7777 -1.7777 2.5   $clover Ge crystal green
95     3  px 9.1                   $clover front crystal
96     3  px 9.2                   $clover front active area
97     3  py 0.02                  $clover active spacing +y
98     3  py -0.02                 $clover active spacing -y
99     3  pz 0.02                  $clover active spacing +z
100    3  pz -0.02                  $clover active spacing -z
101    3  c/x -1.7777 1.7777 2.4   $clover Ge active area blue
102    3  c/x -1.7777 -1.7777 2.4  $clover Ge active area red
103    3  c/x 1.7777 1.7777 2.4    $clover Ge active area black
104    3  c/x 1.7777 -1.7777 2.4   $clover Ge active area green
105    4  px 8.1                   $clover outer face cryostat
106    4  px 8.3                   $clover inner face cryostat
107    4  py 5.05                  $clover left cryostat outer wall
108    4  py -5.05                 $clover right cryostat outer wall
c    109     4  pz 5.05                 $clover top cryostat outer wall
c    110     4  pz -5.05                $clover bottom cryostat outer wall
111    4  py 4.85                  $clover left cryostat inner wall
112    4  py -4.85                 $clover right cryostat inner wall
c    113     4  pz 4.85                 $clover top cryostat inner wall
c    114     4  pz -4.85                $clover bottom cryostate inner wall
115    4  px 17.1                  $clover back crystal
116    4  py 0.01                  $clover spacing +y
117    4  py -0.01                 $clover spacing -y
c    118     4  pz 0.01                 $clover spacing +z
c    119     4  pz -0.01                $clover spacing -z
120    4  c/x -1.7777 1.7777 2.5   $clover Ge crystal blue
121    4  c/x -1.7777 -1.7777 2.5  $clover Ge crystal red
122    4  c/x 1.7777 1.7777 2.5    $clover Ge crystal black
123    4  c/x 1.7777 -1.7777 2.5   $clover Ge crystal green
124    4  px 9.1                   $clover front crystal
125    4  px 9.2                   $clover front active area
126    4  py 0.02                  $clover active spacing +y
127    4  py -0.02                 $clover active spacing -y
c    128     4  pz 0.02                 $clover active spacing +z
c    129     4  pz -0.02                $clover active spacing -z
130    4  c/x -1.7777 1.7777 2.4   $clover Ge active area blue
```

```
131     4  c/x -1.7777 -1.7777 2.4  $clover Ge active area red
132     4  c/x 1.7777 1.7777 2.4    $clover Ge active area black
133     4  c/x 1.7777 -1.7777 2.4   $clover Ge active area green

*tr1   0 0 0 -104 90 -166 90 0 90 -194 90 -284
*tr2   0 0 0   94 90    4 90 0 90  184 90   94
*tr3   0 0 0  -94 -184 90 -184 86 90 90 90 0
*tr4   -2.0 0 0   94 4 90 184 94 90 90 90 0
mode   p
imp:p  0 1 50R
sdef    par=2 pos=0 -0.4 0.4 axs=1 0 0 rad=D1 ext=D2 erg=2.900
sp1    -21 0
si1    1.25
sp2    -21 0
si2    0.05
cut:p  1j 0.001 0
m1     32000 1
m2     8016 0.25 7014 0.75
m3     13000 1
e8     0. 1e-05 2.880 2.920
f8:p   14 19 23 24 25 26 33 34 35 36 43 44 45 46 (23 24 25 26)
       (33 34 35 36) (43 44 45 46)
       (14 19 23 24 25 26 33 34 35 36 43 44 45 46)
nps    500000
```

Appendix C

Gamma ray Summing Corrections

When two or more gamma rays are emitted by a radionuclide within the resolving time of a Ge detector, any two of them may sum and deposit their energy in a composite peak. Each count that results from coincidence summing will result in losses in the full energy peaks, E_γ, of each of the individual emitted gamma rays. During this process, each of the photons may deposit their full energy or a fraction of their energy. The sum of the pulses will result in a peak whose energy is less than or equal to $E_1 + E_2$. If a third gamma ray with energy $E_3 = E_1 + E_2$ were also a member of this decay scheme, then in the event of coincident summing its photopeak would gain counts.

The probability of coincidence summing increases with decreasing source-to-detector distance. To correct for summing effects, it is necessary to calculate the appropriate correction factors for the photopeaks of interest.

Debertin and Schötzig [78] have derived the summing correction factors for the case of a simple, two photon cascade. Fig. C.1 illustrates a simple decay scheme involving three photons. Assuming that the emitted beta particles are absorbed in the endcap of the detector and neglecting bremsstrahlung (electromagnetic radiation emitted when an electron is accelerated in the $\vec{E}$ field of the nucleus [23]), then the rate of the observed pulses depositing their full energy in the Ge detector may be calculated as:

$$N_1 = Ap_1\epsilon_1 \qquad (C.1)$$

$$N_2 = Ap_2\epsilon_2$$

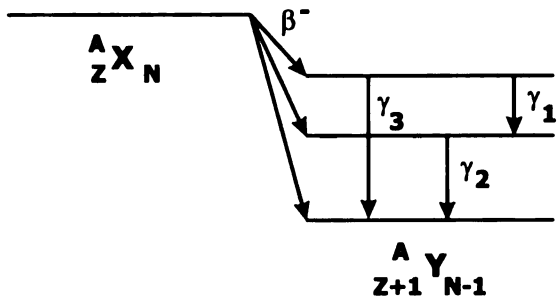

Figure C.1: Simple two photon decay scheme used to illustrate summing corrections calculation.

$$N_3 = A p_3 \epsilon_3$$

where A is the activity of the source, p_x is the probability γ_x will be emitted by the source and ϵ_x is the peak efficiency for a γ-ray with energy E_x. However, due to summing, the actual pulse rate will differ from N_1, N_2 and N_3.

The observed pulse rate for γ_1, N_1', will be smaller than N_1 due to summing out effects. γ_1 will always be followed by γ_2. As a result, the probability that the full energy of γ_1 will be absorbed and sum with γ_2 is $p_1\epsilon_1\epsilon_{T2}$, where ϵ_{T2} is the total efficiency of detecting γ_2. Thus, the sum corrected rate of γ_1 is:

$$N_1' = N_1 - A\, p_1\epsilon_1\epsilon_{T2} \tag{C.2}$$

The summing correction factor for γ_1 is:

$$C_1 = \frac{N_1}{N_1'} = \frac{1}{1 - \epsilon_{T2}} \tag{C.3}$$

The correction factor for peak 2 is calculated differently than peak 1, because γ_2 is not always preceded by γ_1. In this case, the probability that γ_2 will deposit its full energy and sum with γ_1 is $p_1\epsilon_2\epsilon_{T1}$. The sum corrected rate of γ_2 is:

$$N_2' = N_2 - A\, p_1\epsilon_2\epsilon_{T1} \tag{C.4}$$

and the calculated summing correction factor is:

$$C_2 = \frac{1}{1 - (p_1/p_2)\epsilon_{T1}} \tag{C.5}$$

In the case of peak 3, rather than losing counts within its full energy peak, it will gain counts as a result of summing in effects. To correct for this gain in photopeak intensity, the corrected pulse rate must take into account the probability that both γ_1 and γ_2 deposit their full energy within the detectors resolving time, $p_1\epsilon_1\epsilon_2$. The sum corrected rate for peak 3 is:

$$N_3' = N_3 + A\, p_1\epsilon_1\epsilon_2 \tag{C.6}$$

and the summing correction factor for this peak is:

$$C_3 = \frac{1}{1 + p_1\epsilon_1\epsilon_2/(p_3\epsilon_3)} \tag{C.7}$$

The correction factors for complex decay schemes have been derived in Ref. [79-82]. A summary of these corrections have been provided by the National Institute of Standards and Technology (NIST). For summing in gains, the correction factor is calculated as follows:

$$C = \frac{1}{1 + \Sigma[K(a_i, b_i, c)\epsilon_p(a_i)\epsilon_p(b_i)/\epsilon_p(c)]} \tag{C.8}$$

where $K(a_i, b_i, c)$ is the probability that γ_a and γ_b will be emitted in coincidence relative to the emission probability of γ_c, and ϵ_{px} is the peak efficiency for a γ-ray with energy E_x. For summing out losses, the correction factor is:

$$C = \frac{1}{1 - \Sigma[K(s_j, r)\epsilon_T(s_j)]} \tag{C.9}$$

where $K(s_j, r)$ is the probability for the emission of two gamma rays in cascade and $\epsilon_T(s_j)$ is the total efficiency of observing radiation s (for summing losses, the energy of the coincidence gamma rays may range from a fraction to their total energy) summing with the peak area of radiation r.

To correct for summing losses and gains, the experimental emission rates for a number of prominent gamma ray transitions were multiplied by the appropriate correction factors.

Appendix D

Single-Particle Calculations for $N = 29$ Isotones

To extract the energies of the $2p_{3/2}$, $2p_{1/2}$, $1f_{5/2}$ and $1f_{7/2}$ single-particle orbitals, the known spectroscopic factors were compiled. Tables D.1-D.5 provide a list of estimated single-particle energies for the $N = 29$ isotones in the region $20 \leq Z \leq 28$. The spectroscopic factors have been normalized and a weight, W, for each state assigned with the same J^{π} was calculated as the square of the normalized spectroscopic factor. The single-particle energies for each of the states were calculated as,

$$\frac{\sum_{i=1}^{n} E_i(keV) * W_i}{\sum_{i=1}^{n} W_i} \tag{D.1}$$

However, experimental data is limited. The correct single-particle energies cannot be calculated with the present information. Thus, the values tabulated below should only be considered as estimates to the single-particle energies.

Table D.1: Calculated single-particle energies (s.p. E(keV)) for ^{49}Ca [9,64].

J^π	E (keV)	C^2S	*Normalized* C^2S	*Weight*	*s.p.* E (keV)
$3/2^-$	0.0	0.840	0.866	0.750	
	4069.0	0.130	0.134	0.018	
	5539.5	—	—	—	
	6492.0	—	—	—	
					95.2
$1/2^-$	2021.0	0.910	0.883	0.781	
	4261.0	0.120	0.117	0.014	
	4272.0	—	—	—	
	5443.9	—	—	—	
	5568.0	—	—	—	
	5587.7	—	—	—	
					2059.3
$5/2^-$	3586.0	0.110	0.116	0.013	
	3993.0	0.840	0.884	0.782	
					3986.1

Table D.2: Calculated single-particle energies (s.p. E(keV)) for ^{51}Ti [9,65].

J^π	E (keV)	C^2S	*Normalized* C^2S	*Weight*	*s.p.* E (keV)
$3/2^-$	0.0	2.500	0.804	0.646	
	2189.0	0.260	0.084	0.007	
	3164.0	0.350	0.113	0.013	
					83.2
$1/2^-$	1160.0	0.960	0.608	0.369	
	2896.0	0.620	0.392	0.154	
					1671.0
$5/2^-$	2136.0	2.000	1.000	1.000	
					2136.0
$7/2^-$	1437.3	—	—	—	
	2691.4	—	—	—	

Table D.3: Calculated single-particle energies (s.p. E(keV)) for ^{53}Cr [9,66].

J^{π}	E (keV)	S	*Normalized S*	*Weight*	*s.p. E* (keV)
$3/2^-$	0.0	2.220	0.698	0.487	
	2327.0	0.960	0.302	0.091	
	2708.5	—	—	—	
	7940.2	—	—	—	
					366.6
$1/2^-$	565.0	0.710	0.589	0.347	
	2676.0	0.110	0.091	0.008	
	3629.0	0.385	0.320	0.102	
					1287.0
$5/2^-$	1009.0	1.000	1.000	1.000	
	1968.0	—	—	—	
					1009.0
$7/2^-$	1281.0	0.430	0.768	0.590	
	1535.0	0.130	0.232	0.054	
	3381.7	—	—	—	
	10650.0	—	—	—	
					1302.3

Table D.4: Calculated single-particle energies (s.p. E(keV)) for ^{55}Fe [9,67].

J^π	E (keV)	S	*Normalized S*	*Weight*	*s.p. E* (keV)
$3/2^-$	0.0	3.100	0.658	0.433	
	2058.0	0.350	0.074	0.006	
	2478.0	0.680	0.144	0.021	
	3035.0	0.100	0.021	$4e^{-4}$	
	3800.6	—	—	—	
	3906.7	—	—	—	
					215.4
$1/2^-$	413.0	1.200	0.805	0.649	
	1925.0	0.200	0.134	0.018	
	3599.0	—	—	—	
	3790.0	—	—	—	
	4495.1	—	—	—	
	5775.0	0.090	0.060	0.004	
					482.8
$5/2^-$	933.0	3.900	0.809	0.655	
	2151.0	0.920	0.191	0.036	
	2577.4	—	—	—	
					997.2
$7/2^-$	1322.0	0.360	0.720	0.518	
	1413.0	0.140	0.280	0.078	
	2938.9	—	—	—	
	7780.0	—	—	—	
					1334.0

Table D.5: Calculated single-particle energies (s.p. E(keV)) for ^{57}Ni [9, 68].

J^{π}	E (keV)	C^2S	*Normalized* C^2S	*Weight*	*s.p.* E (keV)
$3/2^-$	0.0	1.040	0.832	0.692	
	3007.1	—	—	—	
	3840.0	—	—	—	
	4932.0	0.030	0.024	0.001	
	5089.0	0.030	0.024	0.001	
	5190.0	0.020	0.016	0.0003	
	5668.0	0.030	0.024	0.001	
	6230.0	0.010	0.008	0.0001	
	6550.0	0.030	0.024	0.001	
	6592.0	0.030	0.024	0.001	
	6695.0	0.010	0.008	0.0001	
	7042.0	0.020	0.016	0.0003	
					30.0
$1/2^-$	1113.0	0.210	1.000	1.000	
					1113.0
$5/2^-$	769.0	1.050	1.000	1.000	
	2443.3	—	—	—	
					769.0
$7/2^-$	2570.0	3.100	0.381	0.145	
	3232.0	0.580	0.071	0.005	
	3362.0	0.160	0.020	0.0004	
	4220.0	0.320	0.320	0.002	
	4572.0	0.250	0.031	0.001	
	4892.0	0.020	0.002	$4e^{-6}$	
	5132.0	0.110	0.014	0.0002	
	5235.0	2.050	0.252	0.064	
	5367.0	0.240	0.030	0.001	
	5710.0	0.050	0.006	$4e^{-5}$	
	5795.0	0.060	0.007	$5e^{-5}$	
	5850.0	0.090	0.011	0.0001	
	6115.0	0.050	0.006	$4e^{-5}$	
	6280.0	0.020	0.002	$4e^{-6}$	
	6427.0	0.020	0.002	$4e^{-6}$	
	6520.0	0.040	0.005	$3e^{-5}$	
	6845.0	0.070	0.009	$8e^{-5}$	
	6880.0	0.040	0.005	$3e^{-5}$	
	7130.0	0.760	0.093	0.009	
	7580.0	0.060	0.007	$5e^{-5}$	
	7985.0	0.040	0.005	$3e^{-5}$	
					3547.7

Bibliography

[1] R. Broda, B. Fornal, W. Królas, T. Pawlatt, D. Bazzacco, S. Lunardi, C. Rossi-Alavarez, R. Menegazzo, G. de Angelis, P. Bednarczyk, J. Rico, D. De Acu na, P.J. Daly, R.H. Mayer, M. Sferrazza, H. Grawe, K.H. Maier, and R. Schubart, *$N = 40$ neutron subshell closure in ^{68}Ni nucleus.* Phys. Rev. Lett. **74**:868–871, 1995.

[2] A. Huck, G. Klotz, A. Knipper, G. Marguier, C. Miehé, A. Poves, H.L. Ravn, C. Richard-Serre, and G. Walter, *Beta decay of the new isotopes ^{52}K, ^{52}Ca, and ^{52}Sc; a test of the shell model far from stability.* Phys. Rev. C **31**:2226–2237, 1985.

[3] K.S. Krane, *Introductory Nuclear Physics.* John Wiley & Sons, New York, 1988.

[4] D.R. Lide, *CRC Handbook of Chemistry and Physics.* CRC Press LLC, Florida, 1999.

[5] G. Audi and A.H. Wapstra, *The 1995 update to the atomic mass evaluation.* Nucl. Phys. **A595**:409, 1995.

[6] M.A. Melkanoff, J.S. Nodvik, D.S. Saxon, and R.D. Woods, *Diffuse-surface optical model analysis of elastic scattering of 17- and 31.5 MeV protons.* Phys. Rev. **106**:793–801, 1957.

[7] M.G. Mayer, *Nuclear configurations in the spin orbit coupling model. I. Empirical evidence.* Phys. Rev. **78**:16, 1950.

[8] O. Haxel, J.H.D. Jensen, and H.E. Suess, *Modellmässige deutung der ausgezeichneten nukleonen-zahlen im kernbau.* Z. Phys. **128**:295, 1950.

[9] R.B. Firestone, *Table of Isotopes.* John Wiley & Sons, New York, 1996.

[10] K.L.G. Heyde, *The Nuclear Shell Model.* Springer-Verlag, Berlin, 1994.

[11] G. Brown, A. Denning, and J.G.B. Haigh, *The magnitude of compound nucleus effects in Ca(d,p) reactions.* Nucl. Phys. **A225**:267–299, 1974.

[12] R.F. Casten, *Nuclear Structure from a Simple Perspective.* Oxford University Press, New York, 1990.

[13] R.F. Casten, Jing ye Zhang, N.V. Zamfir, M.A. Caprio, Haibin Zhang, and Fei Du, *Morphologically distinct trajectories of structural evolution in nuclei and their empirical signatures.* Phys. Lett. B **481**:1–6, 2000.

[14] L. Grodzins, *The uniform behaviour of electric quadrupole transition probabilities from first 2^+ states in even-even nuclei.* Phys. Lett. **2**:88–91, 1962.

[15] F.S. Stephens, R.M. Diamond, T. Kammuri, J.R. Leigh, and K. Nakai, *Decoupled yrast states in odd-mass nuclei.* Phys. Rev. Lett. **29**:438–441, 1972.

[16] W.F. Mueller, B. Bruyneel, S. Franchoo, M. Huyse, J. Kurpeta, K. Kruglov, Y. Kudryavtsev, N.V.S.V. Prasad, R. Raabe, I. Reusen, P. Van Duppen, J. Van Roosbroeck, L. Vermeeren, and L. Weissman, *β decay of ^{66}Co, ^{68}Co, and ^{70}Co.* Phys. Rev. C **61**:054308–1–12, 2000.

[17] M. Górska, M. Lipoglavsek, H. Grawe, J. Nyberg, A. Atac, A. Axelsson, R. Bark, J. Blomqvist, J. Cederkall, B. Cederwall, G. de Angelis, C. Fahlander, A. Johnson, S. Leoni, A. Likar, M. Matiuzzi, S. Mitarai, L.-O. Norlin, M. Palacz, J. Persson, H.A. Roth, R. Schubart, D. Seweryniak, T. Shizuma, O. Skeppstedt, G. Sletten, W.B. Walters, and M. Weiszflog, *$^{98}_{48}Cd_{50}$: The two-proton-hole spectrum in $^{100}_{50}Sn_{50}$.* Phys. Rev. Lett. **79**:2415, 1997.

[18] G. Sadler, T.A. Khan, K. Sistemich, J.W. Gruter, H. Lawin, W.D. Lauppe, H.A. Selic, M. Shaanan, F. Schussler, J. Blachot, E. Monnand, G. Bailleul, J.P. Bocquet, P.Pfeiffer, H. Schrader, and B. Fogelberg, *Studies of the β-decay of ^{96}Y and the level scheme of ^{96}Zr.* Nucl. Phys. **A252**:365, 1975.

[19] M. Hannawald, T. Kautzsch, A. Wöhr, W.B. Walters, K.-L. Kratz, V.N. Fedoseyev, V.I. Mishin, W. Böhmer, B. Pfeiffer, V. Sebastian, Y. Jading, U. Köster, J. Lettry, H.L. Ravn, and the ISOLDE Collaboration, *Decay of neutron-rich Mn nuclides and deformation of heavy Fe isotopes.* Phys. Rev. Lett. **82**:1391–1394, 1999.

[20] J.A. Winger, D.S. Brenner, R.L. Gill, J.C. Hill, A. Piotrowski, R.B. Schuhmann, E.K. Warburton, and F.K. Wohn, *Structure of ^{76}Zn from ^{76}Cu decay and systematics of neutron-rich Zn nuclei.* Phys. Rev. C **42**:954–960, 1990.

[21] Y. Fukuda *et al.*, *Evidence for oscillation of atmospheric neutrinos.* Phys. Rev. Lett. **81**:1562–1567, 1998.

[22] L. Wolfenstein, PhysicsWeb - PhysicsWorld.

[23] F. Friedlander, J.W. Kennedy, E.S. Macias, and J.M. Miller, *Nuclear and radiochemistry.* John Wiley & Sons, New York, 1981.

[24] Samuel S.M. Wong, *Introductory Nuclear Physics.* John Wiley & Sons, New York, 1998.

[25] B.M. Sherrill, D.J. Morrissey, J.A. Nolen Jr., and J.A. Winger, *The A1200 projectile fragment separator.* Nucl. Inst. Meth. **B56**:1106–1110, 1991.

[26] J.A. Winger, private communication.

[27] G.F. Knoll, *Radiation Detection and Measurement.* John Wiley & Sons, New York, 1989.

[28] T. Dörfler, W.-K. Schmidt-ott, T. Hild, T. Mehren, W. Böhmer, P. Möller, B. Pfeiffer, T. Rauscher, K.-L. Kratz, O. Sorlin, V. Borrel, S. Grévy, D. Guillemaud-Mueller, A.C. Mueller, F. Poughenon, R. Anne, M. Lewitowicz, A. Ostrowsky, M. Robinson, and M.G. Saint-Laurent, *Neutron-rich isotopes $^{54-57}Ti$.* Phys. Rev. C **54**:2894–2903, 1996.

[29] O. Sorlin, V. Borrel, S. Grévy, D. Guillemaud-Mueller, A.C. Mueller, F. Pougheon, W. Böhmer, K.-L. Kratz, T. Mehren, P. Möller, B. Pfeiffer, T. Rauscher, M.G. Saint-Laurent, R. Anne, M. Lewitowicz, A. Ostrowski, T. Dörfler, and W.-D. Schmidt-Ott, *First beta-decay studies of the neutron-rich isotopes $^{53-55}Sc$ and $^{56-59}V$.* Nucl. Phys. **A632**:205–228, 1998.

[30] F. Ameil, M. Bernas, P. Armbruster, S. Czajkowski, Ph. Dessagne, H. Geissel, E. Hanelt, C. Kozhuharov, C. Miehe, C. Donzaud, A. Grewe, A. Heinz, Z. Janas, M. de Jong, W. Schwab, and S. Steinhäuser, *β-decay half-lives of very neutron-rich isotopes of elements from Ti to Ni.* Eur. Phys. J. **A1**:275–283, 1998.

[31] http://www.triumf.ca/people/chuma/physica/docs.html.

[32] E. Runte, K.-L. Gippert, W.-D. Schmidt-Ott, P. Tidemand-Petersson andL. Ziegeler, R. Kirchner, O. Klepper, P.O. Larsson andE. Roeckl, D. Schardt, N. Kaffrell, P. Peuser, M. Bernas, P. Dessagne, M. Langevin, and K. Rykaczewski, *Decay studies of neutron-rich isotopes of manganese, iron, cobalt, nickel, copper and zinc.* Nucl. Phys. **A441**:237–260, 1985.

[33] http://www.nndc.bnl.gov/.

[34] C.N. Davids, D.F. Geesaman, S.L. Tabor, M.J. Murphy, E.B. Norman, and R.C. Pardo, *Mass and β decay of the new isotope ^{57}Cr.* Phys. Rev. C **17**:1815–1821, 1978.

[35] K.A. Aniol, D.W. Gebbie, C.L. Hollas, and J. Nurzynski, *The $^{50,52,54}Cr(\alpha,p)^{53,55,57}Mn$ reactions at E_α = 18 and 26 MeV.* Nucl. Phys. **A303**:154–184, 1978.

[36] S. Raman, Jr. C.W. Nestor, and P. Tikkanen, *Transition probability from the ground to the first-excited 2^+ state of even-even nuclides.* At. Data Nucl. Data Tables **78**:1–128, 2001.

[37] T. Ishii, M. Asai, A. Makishima, I. Hossain, M. Ogawa, J. Hasegawa, M. Matsuda, and S. Ichikawa, *Core-excited states in the doubly magic ^{68}Ni and its neighbor ^{69}Cu.* Phys. Rev. Lett. **84**:39–42, 2000.

[38] M. Bernas, Ph. Dessagne, M. Langevin, J. Payet, F. Pougheon, and P. Roussel, *Magic features of ^{68}Ni.* Phys. Lett. **113B**:279–282, 1982.

[39] M. Girod, Ph. Dessagne, M. Bernas, M. Langevin, F. Pougheon, and P. Roussel, *Spectroscopy of neutron-rich nickel isotopes: Experimental results and microscopic interpretation.* Phys. Rev. C **37**:2600–2612, 1988.

[40] A.M. Oros-Peusquens and P.F. Mantica, *Particle-core coupling around ^{68}Ni: a study of the subshell closure at $N = 40$.* Nucl. Phys. **A669**:81–100, 2000.

[41] R. Grzywacz, R. Bérand, C. Borcea, A. Emsallem, M. Glogaowdki, H. Grawe, D. Guillemaud-Mueller, M. Hjorth-Jensen, M. Houry, M.Lewitowicz, A.C. Mueller, A. Nowak, A. Plochocki, M. Pfützner, K. Rykaczewski, M.G. Saint-Laurent, J.E. Sauvestre, M. Schaefer, O. Sorlin, J. Szerypo, W. Trinder, S. Viteritti, and J. Winfield, *New island of μs isomers in neutron-rich nuclei around the $Z = 28$ and $N = 40$ shell closures.* Phys. Rev. Lett. **81**:766–769, 1998.

[42] W.F. Mueller, B. Bruyneel, S. Franchoo, M. Huyse, U. Köster, K.-L. Kratz, K. Kruglov, Y. Kudryavtsev, B. Pfeiffer, R. Raabe, I. Reusen, P. Thirolf, P. Van Duppen, J. Van Roosbroeck, L. Vermeeren, W.B. Walters, L. Weissman, and A. Wöhr, *Magicity of the ^{68}Ni semidouble-closed-shell nucleus probed by Gamow-Teller decay of the odd-A neighbors.* Phys. Rev. Lett. **83**:3613–3616, 1999.

[43] Y. Kudryavtsev, J. Andrezejewski, N. Bijnens, S. Franchoo, J. Gentens, M. Huyse, A. Piechaczek, J. Szerypo, H. Reusen, P. Van Duppen, P. Van Den Bergh, L. Vermeeren, J. Wauters, and A. Wöhr, *Beams of short lived nuclei produced by selective laser ionization in a gas cell.* Nucl. Instrum. Methods Phys. Res. B **114**:350, 1996.

[44] S. Franchoo, B. Bruyneel, M. Huyse, U. Köster, K.-L. Kratz, K. Kruglov, Y. Kudryavtsev, W.F. Mueller, B. Pfeiffer, R. Raabe, I. Reusen, P. Thirolf, P. Van Duppen, J. Van Roosbroeck, L. Vermeeren, W.B. Walters, L. Weissman, and A. Wöhr, *Beta decay of neutron-rich cobalt and nickel isotopes.* ENAM98: Exotic Nuclei and Atomic Masses **1**:757–760, 1998.

[45] J.I. Prisciandaro, P.F. Mantica, A.M. Oros-Peusquens, D.W. Anthony, M. Huhta, P.A. Lofy, and R.M. Ronningen, *β decaying $T_{1/2} = 3.4$ s isomer in ^{69}Ni.* Phys. Rev. C **60**:054307-1–7, 1999.

[46] L. Weissman, A. Andreyev, B. Bruyneel, S. Franchoo, M. Huyse, K. Kruglov, Y. Kudryavtsev, W.F. Mueller, R. Raabe, I. Reusen, P. Van Duppen, J. Van Roosbroeck, L. Vermeeren, U. Koster, K.L. Kratz, B. Pfeiffer, P. Thirolf, and W.B. Walters, *β decay of ^{67}Co.* Phys. Rev. C **59**:2004, 1999.

[47] L. Trache, A. Kolomiets, S. Shlomo, K. Heyde, H. Dejbakhsh, C.A. Gagliardi, R.E. Tribble, X.G. Zhou, V.E. Iacob, and A.M. Oros, *"Bare" single-particle energies in ^{56}Ni.* Phys. Rev. C **54**:2361–2368, 1996.

[48] F. Tondeur, *Self-consistent study of nuclei far from stability with the energy density method.* Nuclei Far From Stability; CERN Report **81-09**:81–89, 1981.

[49] X.L. Tu, X.G. Zhou, D.J. Vieira, J.M. Wouters, Z.Y. Zhou, G.L. Seifer, and V.G. Lind, *Direct mass measurements of the neutron-rich isotopes of chlorine through iron.* Z. Phys. **A337**:361–366, 1990.

[50] W.A. Richter, M.G. Van der Merwe, and B.A. Brown, *Shell-model calculations for neutron-rich nuclei in the 0f1p shell.* Nucl. Phys. **A586**:445–456, 1995.

[51] B.A. Brown and W.A. Richter, *Shell-model plus Hartree-Fock calculations for the neutron-rich Ca isotopes.* Phys. Rev. C **58**:2099–2107, 1998.

[52] R. Chapman and S. Hinds, *A study of ^{52}Cr, ^{54}Cr and ^{56}Cr by the (t,p) reaction.* Nucl. Phys. **A119**:305–324, 1968.

[53] T.T. Bardin, J.G. Pronko, R.E. McDonald, and A.R. Poletti, *Gamma-ray spectroscopy of low-lying states in ^{56}Cr.* Phys. Rev. C **14**:1782–1788, 1976.

[54] M.H. Brennan and A.M. Bernstein, *jj coupling model in odd-odd nuclei.* Phys. Rev. **120**:927–933, 1960.

[55] J.I. Prisciandaro, P.F. Mantica, B.A. Brown, D.W. Anthony, M.W. Cooper, A. Garcia, D.E. Groh, A. Komives, W. Kumarasiri, P.A. Lofy, A.M. Oros-Peusquens, S.L. Tabor, and M. Wiedeking, *New evidence for a subshell gap at $N = 32$.* Phys. Lett. B **510**:17–23, 2001.

[56] O. Sorlin, L. Axelsson C. Donzaud, M. Belleguic, R. Béraud, C. Borcea, G. Canchel, E. Chabanat, J.M. Daugas, A. Emsallem, M. Girod, D. Guillemaud-Mueller, K.-L. Kratz, S. Leenhardt, M. Lewitowicz, C. Longour, M.J. Lopez, F. de Oliveira Santos, L. Petizon, B. Pfeiffer, F. Pougheon, M.G. Saint-Laurent, and J.E. Sauvestre, *Beta decay half-lives of neutron-rich Ti-Co isotopes around $N = 40$.* Nucl. Phys. **A669**:351–367, 2000.

[57] A.M. Nathan, J.W. Olness, J.B. McGrory, and E.K. Warburton, *Yrast decay schemes from heavy ions + ^{48}Ca fusion-evaporation reactions. I. $^{54-56}Mn$, ^{56}Cr and $^{52-53}V$.* Phys. Rev. C **16**:192–214, 1977.

[58] P. Federman and S. Pittel, *Towards a unified microscopic description of nuclear deformation.* Phys. Lett. **69B**:385–388, 1977.

[59] K. Heyde, M. Huyse, J. Jolie, J. Moreau, J. Ryckebusch, P. van Duppen, M. Waroquier, and J.L. Wood, *A shell-model description of 0^+ intruder states in even-even nuclei.* Nucl. Phys. **A466**:189–226, 1987.

[60] G. Cata, D. Bucurescu, D. Cutoiu, M. Ivaşcu, and N.V. Zamfir, *Effective boson number calculations in Mo and Cd isotopes.* Z. Phys. **A335**:271–278, 1990.

[61] A. De-Shalit and M. Goldhaber, *Mixed configurations in nuclei.* Phys. Rev. **92**:1211–1218, 1953.

[62] M.N. Rao, J. Rapaport, A. Sperduto, and D.L. Smith, *Nuclear structure studies of the chromium isotopes: The $^{52,53}Cr(p,p')$, $^{53}Cr(p,p'\gamma)$, $^{53}Cr(d,d')$ and $^{52}Cr(d,p)$ reactions.* Nucl. Phys. **A121**:1–37, 1968.

[63] J. Kopecký, K. Abrahams, and F. Stecher-Rasmussen, *Study of the (n,γ) reaction in the mass region A = 50 - 63.* Nucl. Phys. **A188**:535–544, 1972.

[64] T.W. Burrows, *Nuclear data sheets update for A = 49.* Nucl. Data Sheets **76**:191–338, 1995.

[65] Zhou Chunmei, *Nuclear data sheets update for A = 51.* Nucl. Data Sheets **81**:183–324, 1997.

[66] Huo Junde, *Nuclear data sheets update for A = 53.* Nucl. Data Sheets **87**:507–644, 1999.

[67] Zhou Enchen, Huo Junde, Zhou Chunmei, Lu Xiane, and Wang Lizheng, *Nuclear data sheets update for A = 55.* Nucl. Data Sheets **44**:463–658, 1985.

[68] M.R. Bhat, *Nuclear data sheets for A = 57.* Nucl. Data Sheets **85**:415–612, 1998.

[69] J. Duflo and A.P. Zuker, *The nuclear monopole Hamiltonian.* Phys. Rev. C **59**:R2347–R2350, 1999.

[70] W.A. Richter, M.G. Van der Merwe, R.E. Julies, and B.A. Brown, *New effective interactions for the 0f1p shell.* Nucl. Phys. **A523**:325–353, 1991.

[71] T. Mizusaki, T. Otsuka, Y. Utsuno, M. Honma, and T. Sebe, *Shape coexistence in doubly-magic ^{56}Ni by the Monte Carlo Shell Model.* Phys. Rev. C **59**:R1846–R1850, 1999.

[72] P.F. Mantica, A.E. Stuchbery, D.E. Groh, J.I. Prisciandaro, and M.P. Robinson, *g factors of the first 2^+ states in the transitional $^{92,94,96,98,100}Mo$ isotopes and the onset of collectivity.* Phys. Rev. C **63**:034312-1–13, 2001.

[73] M. Huhta, P.F. Mantica, D.W. Anthony, P.A. Lofy, J.I. Prisciandaro, R.M. Ronningen, M. Steiner, and W.B. Walters, *New evidence for deformation in ^{73}Zn.* Phys. Rev. C **58**:3187–3194, 1998.

[74] H. Gotoh and H. Yagi, *Solid angle subtended by a rectangular slit.* Nucl. Inst. Meth. **96**:485–486, 1971.

[75] http://wwwinfo.cern.ch/asdoc/geant_html3/geantall.html.

[76] W.R. Leo, *Techniques for Nuclear and Particle Physics Experiments.* Springer-Verlag, Berlin, 1994.

[77] I.M. Band, M.B. Trzhaskovskaya, and M.A. Listengarten, *Internal conversion coefficients for atomic numbers $Z \leq 30$.* At. Data Nucl. Data Tables **18**:433–457, 1976.

[78] Klaus Debertin and Ulrich Schötzig, *Coincidence summing corrections in Ge(Li)-spectrometry at low source-to-detector distances.* Nucl. Inst. Meth. **158**:471–477, 1979.

[79] D.S. Andreev, K.I. Erokhina, V.S. Zvonov, and I.Kh. Lemberg, *Consideration of cascade transitions in determining the absolute yield of gamma rays.* Instr. Expt. Techn. **25**:1358–1360, 1972.

[80] D.S. Andreev, K.I. Erokhina, V.S. Zvonov, and I.Kh. Lemberg, *Determination of the γ-detection efficiency in energy peaks by means of nuclides having a complicated decay scheme in close-geometry.* Izv. Akad. Nauk. SSR, Ser. Fiz. **37**:1609–1612, 1973.

[81] G.J. McCallum and G.E. Coote, *Influence of source-detector distance on relative intensity and angular correlation measurements with Ge(Li) spectrometers.* Nucl. Inst. Meth. **130**:189–197, 1975.

[82] R.J. Gehrke, R.G. Helmer, and R.C. Greenwood, *Precise relative γ-ray intensities for calibration of Ge-semiconductor detectors.* Nucl. Inst. Meth. **147**:405–423, 1977.